Evaluation of the overall installation penalty of aero-engines for single aisle aircraft

A comparison between engine retro-fit and aircraft redesign

T.E. Boogaart

Technische Universiteit Delft

Evaluation of the overall installation penalty of aero-engines for single aisle aircraft

A comparison between engine retro-fit and aircraft redesign

by

T.E. Boogaart

to obtain the degree of Master of Science
at the Delft University of Technology,
to be defended publicly on 23rd of November, 2021 at 9:00.

Student number:	4228642	
Project duration:	March, 2020 – November, 2021	
Thesis committee:	Dr. A. G. Rao,	FPP, TU Delft, supervisor
	Dr. ir. M.F.M. Hoogreef,	FPP, TU Delft
	Dr. ir. M.M. van Paassen,	C&S, TU Delft
	Dr. ing. A. Heidebrecht	FPP, TU Delft

TU Delft

Preface

This report concludes the Master Thesis research focused on the overall installation penalty of aero-engines on an aircraft. The effects of engine size, weight and location have been investigated using the Initiator toolbox for an aircraft redesign. Furthermore a preliminary stability analysis is done to calculate the effect of a larger engine on the tail design in an engine retro-fit scenario. FlightStream has been used to replace the empirical relation for aerodynamic parameters.

My thesis work took place during the COVID 19 pandemic, visits to the University were not possible because of the lockdown and the required self quarantine. All communication took place with computer programs like Microsoft Teams or Skype. I have missed the live discussions at the university.

I would like to thank my supervisors Arvind Rao and Maurice Hoogreef for the interesting Thesis topic, the discussions we had and for their patience. Special thanks to Maurice Hoogreef for helping me with the Initiator Toolbox and Vivek Ahuja, one of the designers of the FlightStream program. I'm also grateful to my parents for their help and hospitality services during the pandemic and their unconditional support and patience. Lastly, a big thanks to my friends for their moral support, and for being one of the best keepsakes of my time in Delft.

T.E. Boogaart
Delft, October 2021

Abstract

The past 70 years has shown an incredible growth in air transport. The increase in flights has resulted in an increased strain on the environment. Climate change is a fact. Designers have been working on improving the aircraft, and in particular, the engine efficiency. By improving the internal components through better materials, new design methods and new fabrication techniques, the engine specific fuel consumption has decreased. A major factor however is the engine bypass ratio. By increasing the bypass ratio the engine specific fuel consumption (SFC) can be drastically reduced. As a consequence the engine weight and size increased with subsequent ramifications.

Evaluating the installation penalty is not a new topic. In existing literature, studies on the various aerodynamic effects have been published. The largest contributor to the drag is the friction drag from the nacelle. Interference drag due to wing-pylon-nacelle flow interaction can be reduced with proper engine placement. The increase in drag due to a larger engine can also be minimised by the engine location and the shape of the nacelle. All studies show a change in drag when engine size or location are varied. Consequently all studies have been done using finite volume Reynolds Averaged Navier Stokes (RANS) solvers. Friction drag is relatively easy to predict, but if complex flows and separation areas are present, high fidelity tools are required.

An answer to the main research question: **For narrow wing/body aircraft, can the installation penalties from an increase in bypass ratio outweigh the gain in specific fuel consumption?** is found when a full aircraft redesign is allowed. Using the Initiator toolbox it was found that the lower fuel burn, due to a SFC improvement, results is a lighter aircraft for a given mission. The reduction in fuel burn negates the increase in engine weight, drag, and possible interference.

The stability analysis is done for an engine retro-fit scenario, like the 737 MAX. The method used requires several assumptions or estimations based on empirical relations. In order to improve the accuracy the vorticity solver FlightStream was used. It was not possible to validate the A320 design by using both FlightStream and the empirical methods, however the trends observed can be used to evaluate the effect on the c.g. margin and the required tail size. The c.g. margin decreased by max 7.1%, which would nullify a typical stability margin of 5%. The calculated maximum increase in tail size is 18%. Compared to the A320 tail size, it is only a 2% increase, and in most cases the tail becomes smaller. This can be explained because the A320 uses an oversized tail, originally designed for the smaller A318.

Contents

List of Figures

List of Tables

Nomenclature

Value	Unit	Explanation
A	m^2	Capture Area
$\bar{c}$	m	Characteristic chord length, often MAC
C_D	-	Drag coefficient
C_f	-	Friction coefficient
C_{h_α}	-	Hinge moment with respect to angle of attack
C_{h_δ}	-	Hinge moment with respect to elevator deflection
C_p	-	Pressure coefficient
C_L	-	Lift coefficient
$C_{L_{A-h}}$	-	Maximum lift coefficient for the whole aircraft minus the tail
C_{L_R}	-	Lift coefficient at take-off rotation
C_{L_α}	-	Lift slope coefficient
C_{L_h}	-	Maximum lift coefficient for the horizontal tail
$C_{L_{h_\alpha}}$	-	Horizontal tail lift curve slope
$C_{L_{h_\delta}}$	-	Lift curve slope for the horizontal tail with respect to the elevator deflection
C_M	-	Pitching moment coefficient
$C_{M_{ac}}$	-	Pitching moment coefficient around the aerodynamic center
C_N	-	Normal force coefficient
C_T	-	Tangential force coefficient
C_{Th}	-	Thrust coefficient
K_{ng}	-	Weight correction factor, 1.017 for pylon-mounted nacelle
l_h	m	Horizontal distance between the wing quarterchord point and tail quarterchord point
$\dot{m}$	kg/s	Mass flow
N_{en}	-	Number of engines
N_{Lt}	ft	Nacelle length
N_w	ft	Nacelle width
N_z	-	Ultimate load factor
S	m^2	Wing surface area
S_h	m^2	Horizontal tail surface area
S_n	ft^2	Nacelle wetted area
V_h	m/s	Local velocity at the horizontal tail
V_R	m/s	Velocity at take-off
V_{S1}	m/s	Decision speed V1
V	m/s	Ambient velocity
W_{direct}	lbs	Dry engine weight
W_{ec}	lbs	Weight of engine and contents
W_n	lbs	Nacelle weight
x_{ac}	m	X-coordinate of the aerodynamic center
x_{cg}	m	X-coordinate of the center of gravity
x_h	m	X-coordinate of the horizontal tail with respect to a reference location
x_g	m	X-coordinate of the main gear with respect to a reference location
x_n	m	X-coordinate of the neutral point
z_{ac}	m	Z-coordinate of the aerodynamic center
z_{eng}	m	Perpendicular distance between the thrust vector and the center of gravity
α	Degree	Angle of attack
ϵ	Degree	Downwash angle
$\dot{\theta}$	Degree/s	Pitchrate during the rotation phase

Abbreviations

a.c.	Aerodynamic Centre
ACARE	Advisory Council for Aeronautics Research in Europe
AVL	Athena Vortex Lattice
BPR	ByPass Ratio
CAD	Computer Aided Design
CFD	Computational Fluid Dynamics
c.g.	Centre of Gravity
CRM	Common Research Model
FTF	Flap Tracks Fairing
GHG	Green House Gas
HPC	High Pressure Compressor
IATA	International Air Transport Association
ICAO	International Civil Aviation Organization
LPC	Low Pressure Compressor
MAC	Mean Aerodynamic Chord
MDA	Multidisciplinary Design and Analysis
MDO	Multidisciplinary Design and Optimisation
MTOM	Maximum Take-off Mass
MTOW	Maximum Take-Off Weight
NACA	National Advisory Committee for Aeronautics
NASA	National Aeronautics and Space Administration
OEM	Operational Empty Mass
OEW	Operational Empty Weight
(O)PR	(Overall) Pressure Ratio
RANS	Reynolds Averaged Navier Stokes
(T)SFC	(Thrust) Specific Fuel Consumption
S.M.	Stability Margin
SPL	Sound Pressure Level
TET	Turbine Entry Temperature
VLM	Vortex Lattice Method
WB	WingBody
WBPN	WingBody + Pylon + Nacelle

1

Introduction

As of 2021 the effects of climate change are more pronounced than ever before. The emission of greenhouse gasses by humans has been designated to be of great influence to climate change. The aviation sector is a large contributor to the emission of greenhouse gases. This has stimulated the governing bodies in the aviation sector to set ambitious goals to reduce CO_2 and NO_x emissions. The best way to reduce the emissions is by burning less fossil fuels. Alternative fuels and propulsion systems, as seen in cars, are not yet ready for the commercial aviation sector. In order to reduce emissions, the aircraft and aero-engines must become more fuel efficient. Airlines themselves also have an incentive to reduce the fuel burn as the operation costs are directly correlated to the fuel burn. Hence it should not come as a surprise that in the last 70 years engine technology has made significant leaps.

The concept of wing-body aircraft with wing mounted podded engines has been widely adopted. The wing mounted engines meant easy accessibility for maintenance and noise shielding for the passengers. Early gas turbine powered civil aircraft, such as the Boeing 707, look very similar to newest Boeing 737 MAX or 787 Dreamliner. Over the years the engines have become larger, mainly due to the increase in bypass ratio of the engine. By increasing the bypass ratio, the thrust can be generated more efficiently. The side effect is a larger engine diameter. The first generation 737 entered service in 1967. The latest, the 737 MAX, entered service in 2017. The 737 MAX is in principle the same aircraft as its predecessor, except for a newer engine. The new engine is larger, and because the airframe has remained the same, the engine had to be relocated. Sufficient ground clearance was a problem and to solve this, the engine was moved forward and up. The consequence was a changed pitching moment characteristic. To compensate this, the designers implemented a control system (Maneuvering Characteristics Augmentation System (MCAS)), however the system was prone to errors and caused two fatal incidents.

Based on the 737 MAX case, the question arose if it is possible to actually quantify the negative effects of the engine installation. Increasing the engine size will have an effect on the drag, weight and the aerodynamic performance (e.g. stability) of the aircraft. If space between the wing and the ground is limited, resulting in not enough ground clearance, a redesign of the landing gear may be required. A trade-off between an engine retro-fit and a more drastic aircraft redesign will have to be made. Quantifying, or at least getting a better understanding of the installation penalties, can provide new insights. It offers a basis for future aircraft and aero-engine design. If the installation penalties of a more efficient engine on a conventional wing-body become too large, a new aircraft concept should be investigated. If retro-fitting has no significant effect on the aircraft performance, it is still a worthwhile solution for current aircraft. Trying to quantify all the installation penalties is quite a strenuous task. To frame the research several research questions have been defined.

Research Questions

It is noteworthy to investigate whether the current engine and aircraft concept have potential for further efficiency improvements. In other words: at what point will the increase in engine efficiency be fully mitigated by the increase in installation penalties.

The main research question is: **For narrow wing/body aircraft, can the installation penalties from an increase in bypass ratio outweigh the gain in specific fuel consumption?**

Sub-question include:

- How does the engine bypass ratio relate to the engine performance and size?
  - What is the relation between the engine bypass ratio and specific fuel consumption?
  - What is the relation between the engine bypass ratio and engine weight and dimensions? (Nacelle length and diameter)
- What are the engine installation penalties on the aircraft aerodynamics?
  - How does the drag change for the complete aircraft?
  - How does the engine affect the main wing, what are the interference effects?
- How does the addition of an engine change the weight distribution of the aircraft?
  - How does the changed weight distribution affect the stability margins?
  - What is the effect on the empennage due to the changed stability margin?

This research question can be made more specific in the following research goal: Determine the **installation penalty** of **turbofan engines** by comparing the **SFC** for **uninstalled engine + airframe** to the **SFC** for **installed engine + airframe**, for **single aisle aircraft**.

At the end of this research the goal is to find a quantitative value of the fuel burn increase for the engine installation and link the current engine design trends, e.g. larger bypass ratios, to possible gains and respective losses. Figure 1.1 shows an expected result.

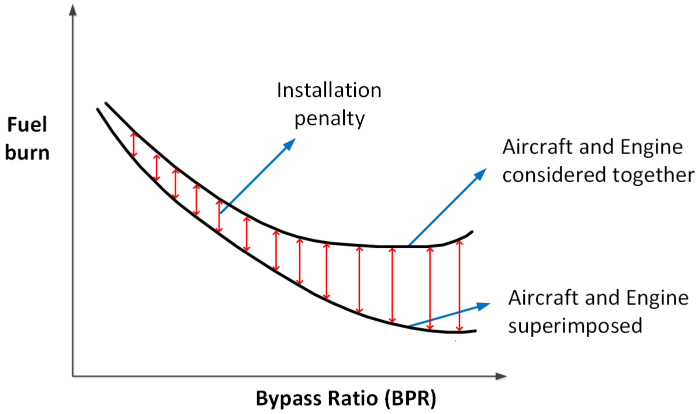

Figure 1.1: Example of the effect of the installation penalty on the fuel burn

Thesis outline

Before any simulation is done, some background knowledge is required. A summary of the literature study is provided in chapter 2. Information of the underlying reasons for the engine improvements is given. Different installation penalties and the subsequent design considerations are explored. To quantify the penalties, several analysis tools have been investigated. The results are shown in chapter 3. Based on the literature review and conclusions from the analysis tools, a method to answer the research questions is formulated. The methodology is explained in chapter 4. The results of a stability analysis for the engine retro-fit, as well as the aircraft redesign using the Initiator tool box, are given in chapter 5. Based on the results, in chapter 6 several (general) conclusions are drawn. Where possible, an answer to the research questions is given. Finally, evaluating the results, conclusions and lessons learned, chapter 7 provides multiple recommendations for future research.

2

Literature Review

In this chapter a literature review is presented on the engine installation effects. Starting with how aero-engines have grown in size and weight because of environmental and financial reasons. In the next sections the installation effects, resulting from the engine geometry, the aerodynamic effects (drag, interference), stability effect, noise, and engine offtakes are discussed.

2.1. Environmental Motive

In the past 70 years passenger air transport has strongly grown, Figure 2.1. This graph does not include military or freight flights. An exponential growth is visible over the past decades. Despite several dips in the number of flights as a result of different worldwide crises, the growth returned to the same growth rate as before.

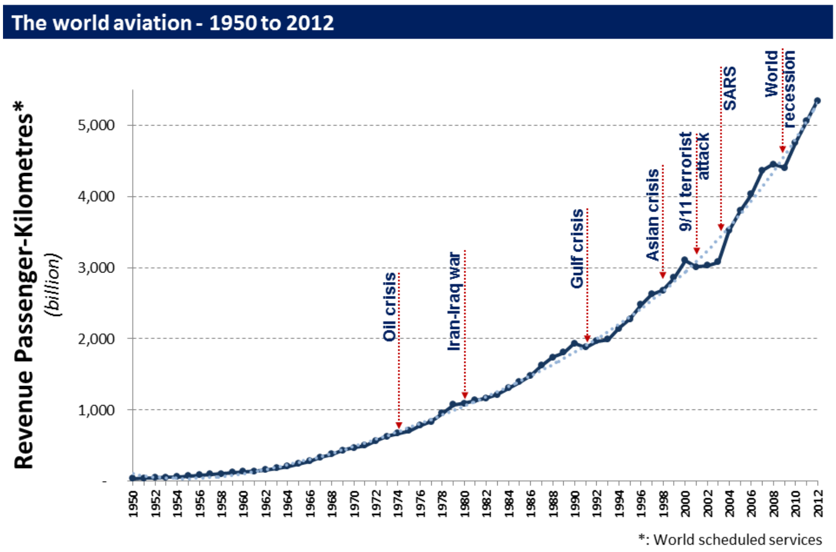

Figure 2.1: Growth of passengers over the last 70 years[1]

As a result of this increase in air traffic, the total CO_2 emission over the last 70 years has also steadily increased, as can be seen in Figure 2.2. Interesting to note is that there is no exponential, but rather a more linear growth in CO_2 emissions. Airline companies have an incentive to keep fuel burn, and subsequently fuel cost, to a minimum. A demand for fuel efficient aircraft arose [26].

---

[1] Obtained from: `https://www.icao.int/sustainability/Pages/Facts-Figures_WorldEconomyData.aspx` [accessed: 28-03-2020]

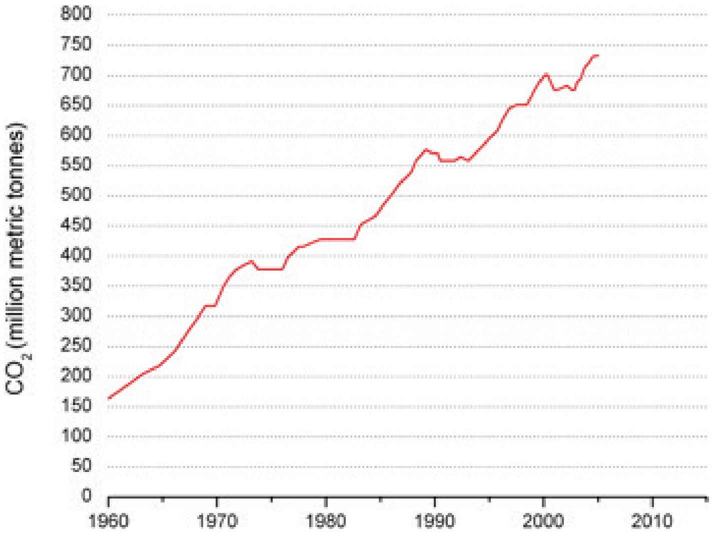

Figure 2.2: CO_2 emissions from aviation (including military and general aviation), 1960 to 2006 [26] adapted from Lee et al(2009) [27]

This becomes more apparent in Figure 2.3 where the average fuel burn per passenger is plotted in the same timespan. Starting from 1968, a decrease in average fuel burn can be observed. Up to 2014 an annual reduction rate of 1.3% was reached [26]. However, when comparing this to the total CO$_2$ increase, see Figure 2.2, due to the increasing air traffic over the last years, it is clear that a reduction rate of 1.3% is enough to stop the CO$_2$ emission growth.

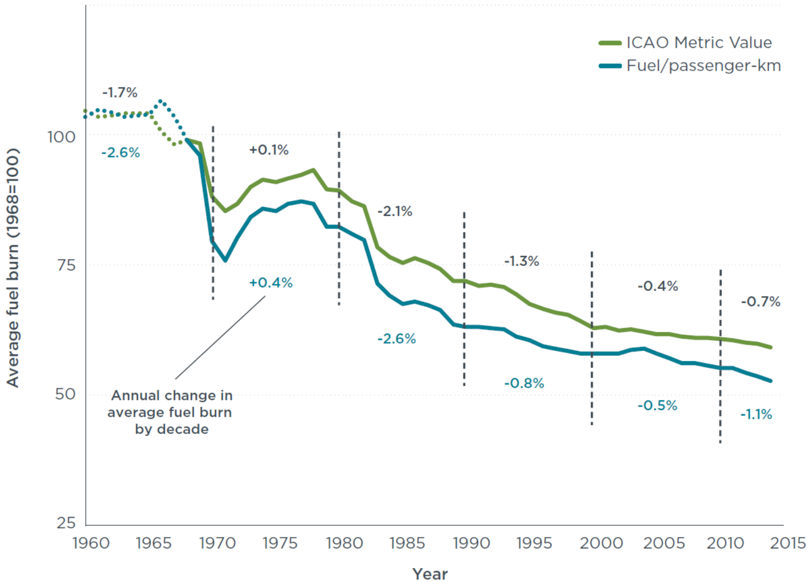

Figure 2.3: Average fuel burn for new commercial jet aircraft, 1960 to 2014 (1968=100) [26]

In the last few years as shown in these graphs, from 1999 to 2008, the scheduled passenger air-travel grew at an average rate of 4.8% per year. In that same period, air freight grew at an average rate of 4.1% per year [13].

From Figure 2.3 it is clear there have been large improvements with respect to fuel burn, and these improvements can be supported by technological advancements. The introduction of high bypass ratio engines in the 1970's is one of the main reasons for the improvement in fuel efficiency [5]. Also at that time the introduction of modern large twin aisle aircraft, such as the 747-200 in '71, meant a reduction in fuel burn per passenger [26]. More passengers could be transported over a longer range with the new 747. Considering that the 747-100 took up 39% of all deliveries in '69 and the 747-200 36% of all aircraft deliveries in ’71 (as described in Rutherford et al based on Ascend Fleets analyser [6]), the decline in average fuel burn in the 1970’s is clarified.

Fuel cost is a large expense for airlines and drives the need for more fuel efficient aircraft. In the last few decades the world has started to realise that not only economic reasons, but also environmental reasons, should drive technological advancements. On top of the ever increasing total CO_2 emission of the aviation sector, the aviation sector is also occupying a larger percentage of the total global CO_2 emissions [27]. Another concern is that most of the aircraft emissions are expelled at high altitude. At high altitude these anthropogenic greenhouse gasses (GHG’s) are more pronounced [16][43]. Despite uncertainties about estimates of the aviation contribution to global warming [53][44], new ambitions for future emissions have been defined. During the 37th Assembly in 2010 of the International Civil Aviation Organization (ICAO) two main goals for the international aviation sector were set [32]:

- A 2% annual fuel efficiency improvement up to 2050
- A carbon neutral growth from 2020 onwards

In 2009 the International Air Transport Association (IATA), the trade association for the world’s airlines, set out the following three targets for future emissions:[2]

- An average improvement in fuel efficiency of 1.5% per year from 2009 to 2020.
- A cap on net aviation CO_2 emissions from 2020 (carbon-neutral growth).
- A reduction in net aviation CO_2 emissions of 50% by 2050, relative to 2005 levels.

Lastly the Advisory Council for Aeronautics Research in Europe (ACARE) also set a series of targets for future aircraft and aviation with the name **Flightpath 2050**:[3]

- In 2050 technologies and procedures available allow a 75% reduction in CO_2 emissions per passenger kilometre and a 90% reduction in NO_x emissions. The perceived noise emission of flying aircraft is reduced by 65%. These targets are relative to the capabilities of typical new aircraft in 2000.
- Aircraft movements are emission-free when taxiing.
- Air vehicles are designed and manufactured to be recyclable.
- Europe is established as a centre of excellence on sustainable alternative fuels, including those for aviation, based on a strong European energy policy.
- Europe is at the forefront of atmospheric research and takes the lead in the formulation of a prioritised environmental action plan and establishment of global environmental standards.

The above mentioned goals have been set already 10 years ago. Today we can see already some improvement with the entry into service of the next generation aircraft, such as the Boeing 737 MAX, 777x, 787 and Airbus A320neo, A330neo, A350. All aircraft support the new generation aero-engines with new engine technologies.

2.2. Engine installation effects

An ideal aero-engine would have no weight, no drag and no exhaust flow while providing the required thrust through the centre of gravity of the aircraft. Unfortunately this is not possible. The engine does have a weight, an exhaust flow, and causes drag which all have an effect on the airframe performance. The following chapter describes the integration effects and the consequences on the aircraft design.

An aircraft engine can be split into three main components: the gas generator, nacelle and pylon. Each component has a different effect on the aircraft and subsequently the aircraft performance. Figure 2.4 indicates the installation effect of the aforementioned components. The drag effects are indicated in red. The other aerodynamic effects are shown in orange. Lastly the stability effects are shown in blue.

---

[2] obtained from: `https://www.iata.org/en/policy/environment/climate-change/` [accessed on: 28-03-2020]

[3] obtained from: `https://www.acare4europe.org/sria/flightpath-2050-goals/protecting-environment-and-energy-supply-0` [accessed on: 28-03-2020]

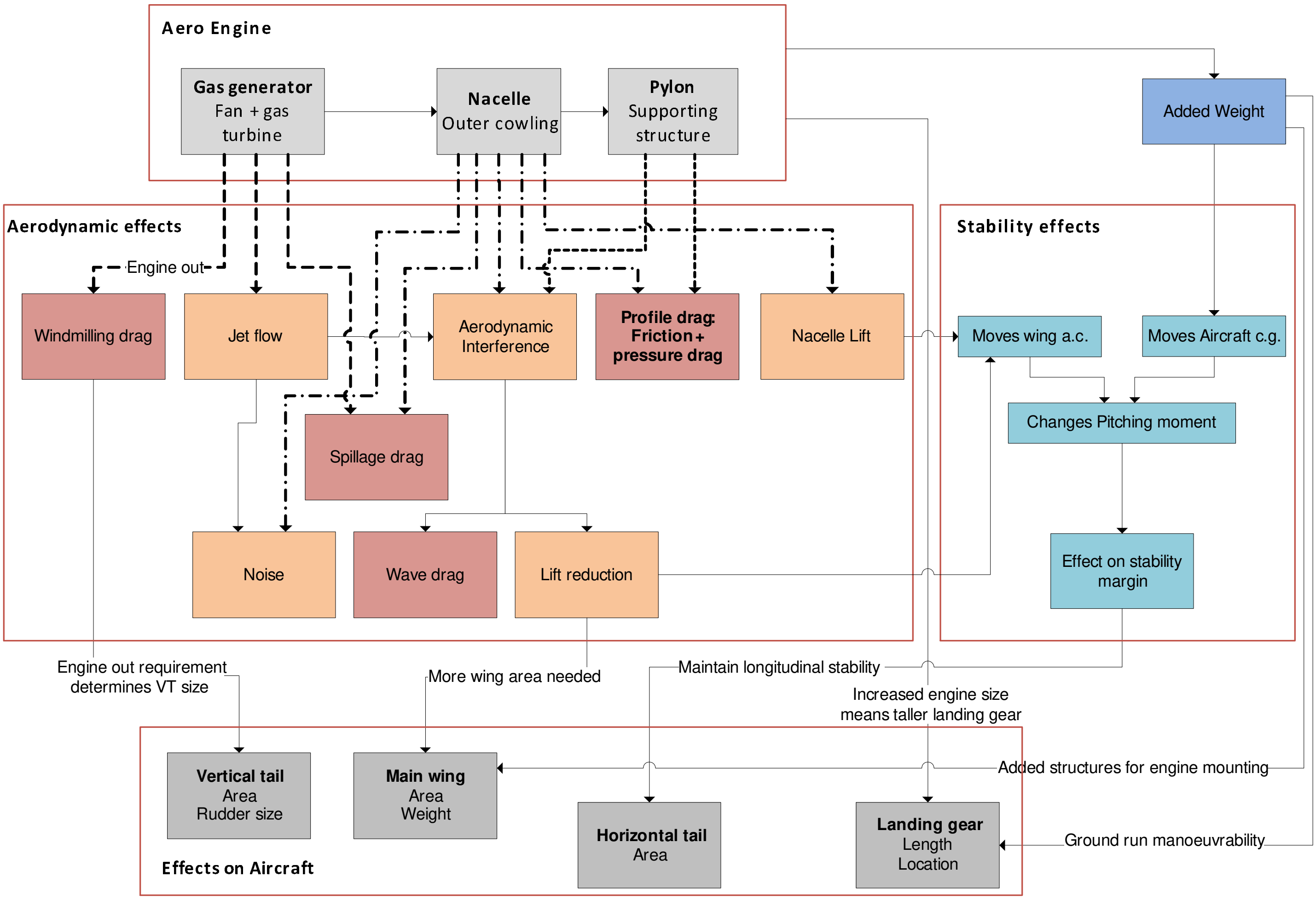

Figure 2.4: Schematic of various installation effects, their dependencies and the consequences on the aircraft geometry

2.2.1. Geometry considerations

Modern transport aircraft utilise podded engines mounted on a pylon. Podded engines can be mounted to either the wing or the fuselage. In the past embedded engines have also been tried. The ”De Havilland Comet”, see Figure 2.5, used engines mounted in the wing root. Embedded engines are still used in fighter aircraft. Another concept used by McDonnel Douglas had a third engine mounted in the vertical tail, see Figure 2.6.

Figure 2.5: De Havilland Comet supporting engines mounted inside the wing structure

Figure 2.6: McDonnel Douglas DC-10 that uses a tri-engine set up with the third engine mounted in the vertical tail

To improve engine fuel efficiency the bypass ratio has increased and simultaneously the engine diameter has grown (see Figure 2.7 and Figure 2.8). Only under-the-wing mounted engines are left as a feasible option. For smaller jets, fuselage mounted engines are still an option when thrust requirements are low. The trend for larger podded engines mounted below the wing means new solutions must be found for the pylon and the nacelle design.

Aero-engine geometry

In Figure 2.4 three main engine components are defined: the fan + gas generator, the nacelle and the pylon. These three are picked since they are the main drivers for the integration effects. This section will elaborate on the considerations and constraints applicable to these three engine components.

Fan + Gas generator The overall engine size and weight will be governed by the size of the fan and gas generator. In general a larger bypass ratio means a larger fan diameter and larger frontal area. The larger frontal area results in a larger **windmilling drag** in case of engine failure. The effects of increased windmilling drag are discussed later.

The fan diameter directly influences the nacelle diameter. The increased nacelle diameter results in a larger wetted area and therefore larger drag penalty. The nacelle can also be used for mixing the exhaust flow with the bypass flow. Therefore the nacelle length is dependent on the bypass ratio and the size of the gas generator.

The gas generator is part of the core engine. It is needed to drive the fan and provides part of the thrust. The gas generator produces a high velocity **jet flow**. The jet flow can cause adverse aerodynamic effects if the flow is too close to other aerodynamic bodies. The jet flow is also a large source of engine **noise** during take-off. The core flow and bypass flow also lead to a mixing loss. Mixing losses are generally only considered when evaluating the engine performance by itself, rather than looking at the engine penalty on the aircraft performance.

Nacelle The main purpose of the nacelle is to cover the engine with the lowest possible drag penalty. In general the nacelle area should be minimised such that the wetted area is minimised and **friction drag** is as low as possible. Furthermore the shape of the nacelle can be modified to minimise **form** or **profile drag** [7]. In the case of the Boeing 737-400, Figure 2.8, the nacelles were ovoid to allow for better ground clearance while retaining the correct inlet conditions. All at the cost of increasing the wetted area and friction drag.

Figure 2.7: Front view of the first generation Boeing 737-200 advanced, using the older JT8D engines

Figure 2.8: Front view of the third generation Boeing 737 classic, using the CFM56-7 engine with ovoid nacelle

Second to providing an engine cover, the nacelle serves as a duct for the bypass flow and shapes the engine inlet. The purpose of the inlet is to reduce the flow Mach number before it reaches the fan and compressor. The inlet must be able to do this for different flight conditions. As a result the streamtube entering the inlet varies in size. During take off, the streamtube is large and the inlet design must prevent separation inside the nacelle inlet. During cruise, the streamtube is small and most of the flow is redirected outside the inlet. The increase in drag from the excess flow around the nacelle is called **spillage drag**. It can amount to a large portion of the total engine drag [30]. A careful trade-off must be made between low speed inlet stall and the drag during cruise. The exhaust can also drastically influence the engine performance. If a full length exhaust is used to mix the core and bypass flow, the engine **noise** can be significantly reduced. Moreover the thrust specific fuel consumption (TSFC) will also improve due to a better thermal efficiency from the exhaust flow mixing. The better TSFC however is often negated by the increase in drag from the longer nacelle [4].

The nacelle diameter is driven by the fan size. By adding the surrounding systems and clearance requirements, the maximum nacelle diameter is roughly fixed. The nacelle length is less constrained. As stated before, one could opt for a short nacelle and sacrifice mixing for less profile drag. However, the ratio between the diameter and length has also been shown to be important. Stubby nacelles, short length over diameter, tend to show a higher **wave drag**. It is caused by the higher curvatures for shorter nacelles resulting in higher velocities over the surface. A solution could be to have longer nacelles with adversely a larger wetted area and higher drag [9].

Practical requirements to the nacelle include: accessibility for maintenance and protection in case of blade failure, no blades are allowed to exit the engine. Ground clearance can be a requirement for the nacelle design, although it can be mitigated by changing the engine location on the wing. With positive dihedral (wings are angled upwards) and placing the engine further outboard the ground clearance can be increased.

Pylon For podded engines the pylon is the bridging part that connects the engine to the aircraft. The pylons are a structural component and houses fuel and bleed air lines coming from the engine. For wing mounted engines the pylon attaches to the wing structure (the wingbox). For fuselage mounted engines the pylons are integrated in the fuselage structure. Pylons for fuselage mounted engines are heavier as they are placed horizontally and have to carry bending loads [49].

Mounting the engines using a pylon gives quite some freedom in engine placement. Spanwise location can be quite easily modified as long as ground clearance is not becoming an issue. The pylon can also be used to place the engine higher up and closer to the wing. Placing multiple curved bodies in close proximity can increase the **interference effects**. Adding twist, camber and local fairings to the pylon can help to reduce the effects. Another option is to use the pylon to mount the engine further forward. Engine location will have an effect on the centre of gravity and subsequently the stability margins.

2.2.2. Aerodynamic effects

Two forms of aerodynamic effects will be discussed. First the different sources of drag such as friction drag, spillage drag, wave drag and windmilling drag. In addition to the various sources of drag other aerodynamic effects include the aerodynamic interference, the jet flow and the nacelle lift.

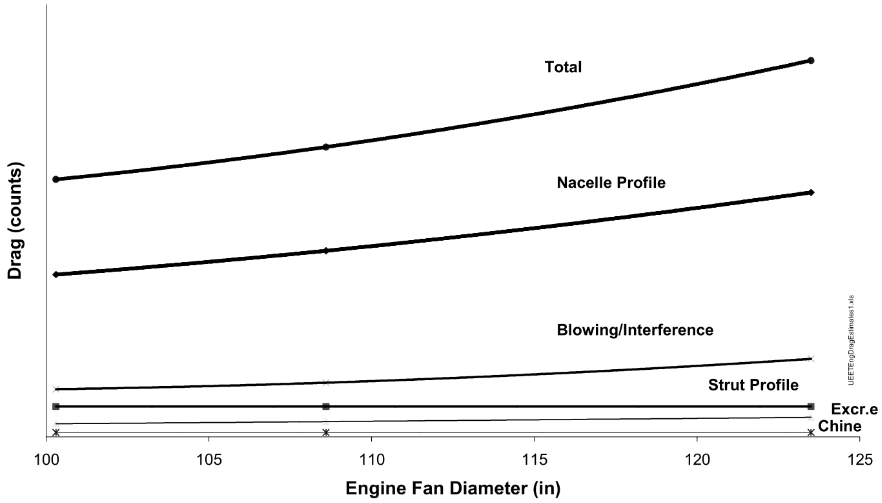

Figure 2.9: Drag component breakdown for a gas turbine engine as a function of fan diameter. Study performed by Dagget et al [9]

Drag effects

Engine studies in the past have shown that two podded under wing mounted engines add 30 to 50 drag counts for a 777 type aircraft. For engines with a larger diameter, the effects become more significant [47]. Figure 2.9 shows the drag composition for an engine. The main contribution to the drag comes from the profile drag of the nacelles. In this graph the profile drag is a combination of the friction and pressure drag.

To calculate the drag for the engine, analytical/empirical relations can be used during the preliminary design phase. However when more complex flow phenomena occur, these methods are no longer sufficient. For further more detailed design, a method involving computational fluid dynamics (CFD) should be used [31]. For CFD solvers the computational time can quickly increase if the geometry complexity grows. The wing-pylon-nacelle interaction is an example of complex geometry. Together with the geometry size, the solver times will be long.

In a research by the DLR and ONERA the effect of the engine location was examined with respect to the installation drag [15][22]. It was concluded that the optimal engine position yields a nearly constant installation drag coefficient for the lift range considered. The design goal should be to minimise the installation drag for a given lift coefficient. The installation drag can be split in different drag sources, which are explained in the next paragraph.

Friction drag A fluid particle moving along a surface experiences a tangential friction force. Equally every aircraft component with a surface area that is in contact with an airstream produces a friction drag. Friction drag occurs in flows where viscous effects are taken into account. In viscous flows the boundary layer is fully modelled and the friction drag follows from the boundary layer theory [21]. The Reynolds number is an indication of the thickness of the boundary layer and therefore also for viscous effects. For a large transport aircraft the Reynolds number is large. This means viscous forces are less prevalent and an assumption for the friction forces may be used. The friction drag can be calculated with the Equation 2.1 from Obert [30]:

$$C_{D_{friction}} = C_f \frac{S_{wet}}{S_{ref}} \tag{2.1}$$

where:

- C_f is the friction coefficient
- S_{wet} is the wetted surface area of the body for which the friction drag is calculated
- S_{ref} is a reference surface area, generally the wing surface area

The friction coefficient C_f is dependent on the surface roughness. A smoother surface will reduce the friction coefficient and postpones the point of transition from laminar to turbulent flow, further reducing the friction coefficient. The transition point is also dependent on the flow conditions and Reynolds number. As a first order estimation the friction coefficient can be estimated from test data for a specific Reynolds number.

For aircraft engines, the friction drag can be lowered by reducing the wetted area. This might not always be possible due to constraints, e.g required surface area to produce lift, or the nacelle size which depends on the bypass ratio. Another method is reducing the surface roughness. This has been done by countersinking the rivets and painting the panels. However certain irregularities, such as panel edges or lights, can not be resolved [30].

Pressure drag The friction drag together with the pressure drag is often referred to as profile drag or form drag [49]. Similar to the friction drag the pressure drag follows from the interaction between an airstream and a body. Where friction drag acts tangential to the surface, the pressure drag is perpendicular to the surface. A large increase in pressure drag occurs when flow separation takes place. Flow separation typically happens at large angles of attack or when a too large radius of curvature is used on a body.

Flow separation causes a major increase in pressure drag. For an attached flow there is also a pressure drag component. The main driver for the profile drag is the shape of the body or the non-zero pressure gradient that the body creates [7]. Therefore it is often associated with the thickness of a body and called form drag. A perfect body from a pressure drag point of view would be a straight one dimensional line. As long as the engine produces a non-zero pressure gradient, it will produce a pressure drag. There is a difference in the drag between engine ”on” and ”off” conditions due to the presence of an inlet stream and exhaust jet flow. The inlet and exhaust flows will induce a pressure gradient.

Reducing the pressure drag for a gas turbine is very difficult as it is inherent to a body with thickness and curvature. The nacelle can be ’streamlined’ and thus reducing the wake size. The smaller wake reduces the pressure drag as well [21]. A better goal should be to avoid a rapid increase in pressure drag due to flow separation over the nacelle or in the inlet.

Spillage drag The engine spillage drag is a different way of describing the profile drag of the nacelle. It is however associated with a drag increase due to off-design flight conditions. Spillage drag is defined by Covert as: the drag increase resulting from the difference between the inlet mass flow ratio at the operating conditions and the operating reference condition [7]. Aero engines operate at multiple, very different, flight- and operating conditions. For instance, high required thrust at sea level and low flight speed during take-off or relatively low thrust at high altitude and high flight speed during cruise. Figure 2.10 shows the capture area for two different thrust settings.

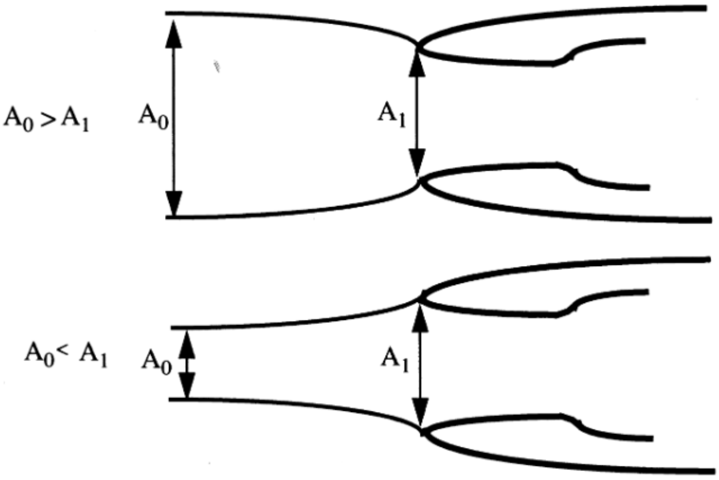

Figure 2.10: The inlet capture area for a low speed high thrust setting (top), and a high speed low thrust setting (bottom)

The spillage drag occurs when A_0 is much smaller than A_1. The large adverse pressure gradient at the inlet lip causes flow separation around the nacelle. Reducing the inlet size A_1 will reduce the adverse pressure gradient and therefore reduces the spillage drag. The smaller inlet can cause flow separation in the inlet in the case of a large streamtube. Optimal would be the smallest possible inlet area for which no flow separation occurs in the inlet at take off thrust. Robinson [40] investigated the effect of engine geometry on spillage drag. The study was limited to a CFD analysis. The spillage drag was roughly 10% of the total drag calculated. The spillage drag was also dependent on the exhaust geometry used.

Wave drag Wave drag is defined as the increase in drag due to the presence of shockwaves. Shockwaves occur when the flow becomes supersonic. Transport aircraft fly transonic, but due to local velocity increasing over negative pressure zones, shockwaves can still arise [52]. With more bodies in close proximity of each other, flow interference between the bodies can cause local supervelocities and shockwaves.

Shockwaves should be avoided at all costs. The nacelle, pylon and main wing are located closely together. The chance of local supervelocities is therefore realistic. Possible ways to reduce the chance are: increasing the distance between components or reducing local curvature. In the Boeing 777 engine study, the writers investigated the possibility of low velocity pressure side of the main wing to reduce local shock formation [4]. Alternatively, the nacelle shape can be modified to reduce supervelocities and reduce the chances of shockwaves.

Windmilling drag Lastly, the windmilling drag is defined as the added drag from the engine in case it fails during flight. The drag of a windmilling gas-turbine engine is composed of external drag due to spillage of the inlet and internal drag associated with pressure losses in the flow through the windmilling engine [49].

The windmilling drag causes a yawing moment that induces sideslip. The engine location and engine size are both influencing factors. In order to reduce the drag the wetted area must be minimised, as well as the frontal area. This is often not possible as a larger fan diameter allows for a higher bypass ratio and a better SFC. It only leaves external drag to be reduced, but this is already the goal in nacelle design. The moment can also be reduced by locating the engine further inboard. Moving the engine further inboard can result in ground clearance issues, or increased interference between the jet flow and horizontal tail.

Non-drag effects

Other aerodynamic effects that originate from the engine include aerodynamic interference, jet flow effects and noise.

Aerodynamic interference The addition of the nacelle and pylon mounted to the main wing or fuselage means multiple bodies in close proximity. Interference between two bodies can be used as an advantage on lift generating bodies, e.g. multi-element flaps. For the pylon and nacelle it often results in an increase in drag and loss in lift [52][22].

Figure 2.11 shows the pressure distribution (Cp) for a wing with (WBNP) and without (WB) nacelle and pylon. In both cases fairings on the bottom side that cover the flap mechanisms (FTF) are included. The location of the cross-section is in spanwise direction just before the pylon. The interference effects between the wing and nacelle-pylon are visible through two suction peaks.

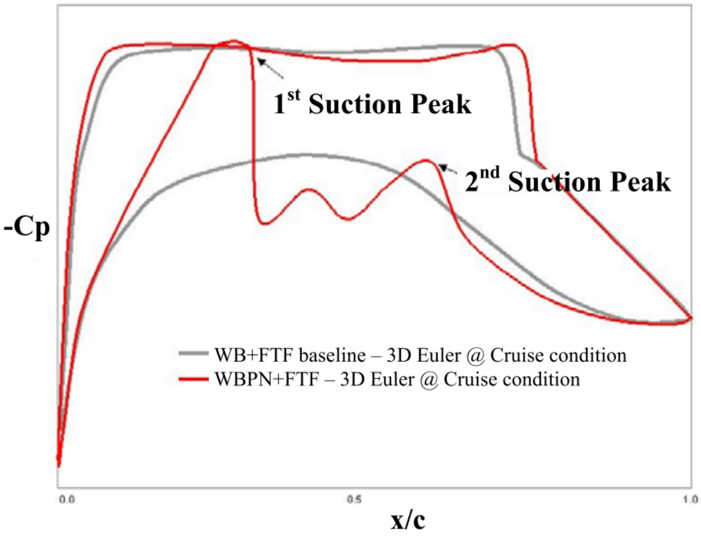

Figure 2.11: The Cp distributions of the clean wing baseline configuration (WB+FTF) and the podded wing configuration (WBPN+FTF), at a wing-section just to the right of the pylon. Taken from Oliveira et al [31]

The graph is produced using an invicid analyses. In reality the viscous effects reduce the amplitudes of the suction peaks, making the invicid analysis a conservative method [31]. The suction peaks can be reduced by modifying the engine location. By moving the engine, the channels between the nacelle and wing can be altered to mitigate the interference effects. Hoheisel showed that with the engine installation there is a loss in lift on more than 60% of the span [22]. In general, when moving the engines more forward, the interference is reduced [4]. Engines moved more forward and keeping the same ground clearance, will result in a larger gully (the distance between the wing and nacelle) and reduced interference between nacelle and main wing. The loss of lift due to engines being present for low angles of attack means new trim conditions and possible higher trim drag compared to the aircraft without engines. According [42] increasing the vertical distance to the wing does not have a significant influence.

The engines can also be placed on the fuselage rather than under the wing. Fuselage mounted engines yield practical advantages, such as smaller landing gear for easy boarding of the aircraft and a lower landing gear weight. The interference effects are stronger due to possible boundary layer separation in the divergent portion of the channel formed between the nacelle, pylon and fuselage. At high Mach numbers this can lead to forming of shockwaves and an increase in wave drag [49].

Jet flow A special case of interference flows is caused by the exhaust flow. With under wing engines the jet flow moves over the pressure side of the wing, especially in case of far forward engines. The high velocity jet flow reduces the pressure on the bottom side of the wing and reduces the lift locally. Measures must be taken to ensure enough lift can be generated when the engines are installed [4].

Hoheisel showed that higher bypass ratio engines lead to smaller jet flow velocities due to better and more mixing of the exhaust gasses [22]. Although the effects of the jet flow are small, higher bypass engines are often located closer to the lower surface of the wing and as mentioned before this can have negative effects on the interference drag [36].

Nacelle lift Typically the nacelle is not designed to produce lift during cruise. Reducing the nacelle drag is the predominant requirement for nacelle design. During the take-off and landing phases the angle of attack will be higher, and the nacelle will produce a lift force. With the engine and nacelle becoming larger this force will have larger effects. This must be accounted for in the tail sizing, but is not a design consideration for the nacelle itself. During take-off the nacelle inlet design is much more important than the possible lift generation.

2.2.3. Stability effects

The engines are a significant portion of the empty weight of an aircraft. The added weight causes a change in the centre of gravity (c.g.). Moving pylon mounted engines along the wingspan, or along the fuselage will have an effect on the centre of gravity. This change in centre of gravity can cause the stability margin of the aircraft to become smaller with control problems as a result.

Longitudinal stability

Transport aircraft are longitudinally stable which means if the aircraft flies level, after a pitch disturbance the aircraft will return to level flight again. Normally the horizontal tail will be sized such that it balances the moment created by the lift [50]. Engine location can help reducing the required tail surface. The forces and moments that act on the aircraft during flight are shown in Figure 2.12. Drag is not included, because the moment due to drag is negligible compared to the moment due to lift.

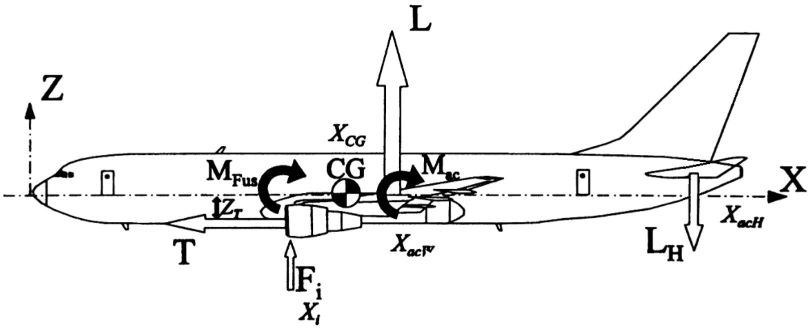

Figure 2.12: Forces and moments in flight used for a typical stability analysis, taken from [3]

In this case the engines are located below the c.g. of the aircraft, they will cause a destabilising effect or pitch up moment [3]. Reducing the distance between the thrust vector and the c.g. can reduce this moment and improve the pitch characteristics. With the current engines becoming larger due to bigger bypass ratios, as a consequence the thrust vector will move down and increases the pitch up moment. Fuselage mounted engines are a possible solution for this problem. With the engines located above and further behind the centre of gravity, the engines will have a stabilising effect [49].

If the engines are moved further back, the c.g. will move back as well. With the c.g. closer to the aerodynamic centre (a.c.), where the main lift vector acts, the required force by the tail will be reduced. With the engines moved back, the chance of higher interference drag becomes imminent. Another way to move back the c.g. is by moving the engines further outboard in case of a swept wing. However engines moved further outboard will yield directional stability problems in case of one-engine-out conditions [17].

For the Boeing 737 MAX the increased size of the LEAP 1B engine caused stability problems. The larger bypass ratio meant a larger diameter of the nacelle and added weight. It also meant that in order to maintain the required ground clearance, the engines had to be moved forward to mount them higher. As a result, the aircraft had a nose up pitching moment for mid Mach numbers and high angles of attack [23]. As mitigation an automatic control system was implemented. Due to a sensor failure, the control system did not work properly and caused multiple incidents.

Lastly, there are also the ground manoeuvring and tip over criteria which require the main landing gears to be far enough apart [41]. The location of the landing gear has an effect on the centre of gravity. It can also cause the engines to be moved further out to not interfere with the landing gear.

Directional stability

The directional stability determines the aircraft performance during side slip. Wing mounted engines, which use a pylon, have significant effects on the spanwise pressure distribution, especially during sideslip. The jet wash for wing mounted engines is not of importance for the lateral stability. The vertical tail is not in direct contact with the jet wash. For fuselage mounted engines this is more likely to happen and must be considered [38].

One engine inoperative For multi-engine aircraft, in case of one engine is inoperative, wing mounted engines generate a large yawing moment. The engine location as well as engine size are factors that determine the yawing moment. This yawing moment in turn is used to size the vertical tail and the rudder of the aircraft [49]. When one engine fails the other has to provide the thrust. The failed engine will impose a drag penalty which will further affect the yawing moment [9].

Adding larger engines, for example because of an increased bypass ratio, will cause a higher drag and to mitigate the increased yawing moment, the vertical tail must grow accordingly. When the engines are moved further out to make better use of the bending relief or to yield more ground clearance, the vertical tail will grow as well.

2.2.4. Engine noise

Aircraft noise has become more of a problem over the last few decades as air transport has increased significantly. With larger airports and more flights per day the noise pollution has grown accordingly. Therefore not only emission goals for the future have been set, but also a reduction in noise is aspired [8].

In the past, engines were a large contributor to noise. With the increase in bypass ratio the jet noise from the engine has decreased and an overall drop in engine noise of roughly 20% has been achieved [20]. Furthermore, the fan pressure ratio has been decreased for large bypass ratio engines, this is to reduce jet velocity and to increase propulsive efficiency. The lower fan pressure ratio entails larger diameter engines and with the engine being the main noise contributor during take-off, ways to reduce fan noise should be considered [9][8].

Engine location can help with noise shielding. For example engines located below the wing will result in better noise shielding for the passengers. With the wing between the engine and the cabin, noise levels will be lower in the cabin. However for ground level noise, fuselage mounted engines are preferred. For fuselage mounted engines the main wing can be used to shield the ground from inlet noise [20]. Another possibility to shield ground noise is to place the engines on top of the wing, as was done by the Fokker VFW 614, see Figure 2.13. However this will have a negative affect on the noise to the passengers in the cabin.

Figure 2.13: Fokker VFW 614 with over-the-wing mounted engines

On top of or over-the-wing mounted engines will have the same advantages as fuselage mounted engines regarding noise shielding. It better facilitates engine growth, e.g larger bypass ratio, compared to fuselage mounted engines. The interference effects are much larger for engines mounted on top of the wing. The location of the suction side and the high velocity flow, together with the nacelle and pylon, will result in a high chance of shockwaves at transonic conditions. Engine maintenance is also more complex for the engines at this less accessible location. At high angles of attack, the inlet might be disturbed due to flow separation with possible engine surge as a result. In order to improve total aircraft performance, boundary layer ingestion can be implemented for over the wing engines. With boundary layer ingestion the profile drag of the aircraft can be reduced, but this will be at the cost of engines performance and efficiency. The boundary layer flow is often turbulent and viscous forces dominate. As a result larger pressure losses in the inlet will occur with detrimental effects on the performance [18].

With an increasing number of engines, the Sound Pressure Level (SPL) spectrum is shifted to higher frequencies. This is expected, in contrast to the SPL peaks, they remain roughly the same. It can be concluded that the effects of jet noise for reduced engine size and number of engines balance each other. Unfortunately, the peak SPL for higher numbers of engines lies around 800 Hz which is a heavily weighted frequency in perceived noise metrics [19].

The noise emanating from the engine is not only due to the jet flow or the fan, but can also find its origin in the surrounding structures. The pylon creates flow features that interact with the jet and are influenced by aircraft attitude. Another example is the interaction of the fan or core jet exhaust flow with an extended flap. This interaction is often present on wing mounted engine configurations. These flow interactions, that are only present on installed engines, can lead to new acoustic sources [20].

2.2.5. Engine offtakes

The aircraft engines provide power for the avionics, cabin systems and provide the bleed air for the climate control in the cabin. In case of larger aircraft more power offtake and bleed air is required [34].

It also means that during engine design the increase in SFC and loss of thrust due to bleed air must be considered. With higher bypass ratio engines the fan pressure ratio is going down and this results in higher pressure losses from bleed offtakes in the bypass ducts [34]. Therefore for large bypass ratio engines separate electrical systems are being considered.

Giannakakis showed the SFC penalty for shaft and bleed-air offtakes and how these would change with modified engine size. The bypass ratio and the specific thrust have also been varied. For both varying there is a small change in SFC, however this change is not enough to affect the aero-engine design. The performance gains are simply too large for the penalties to have an effect [14].

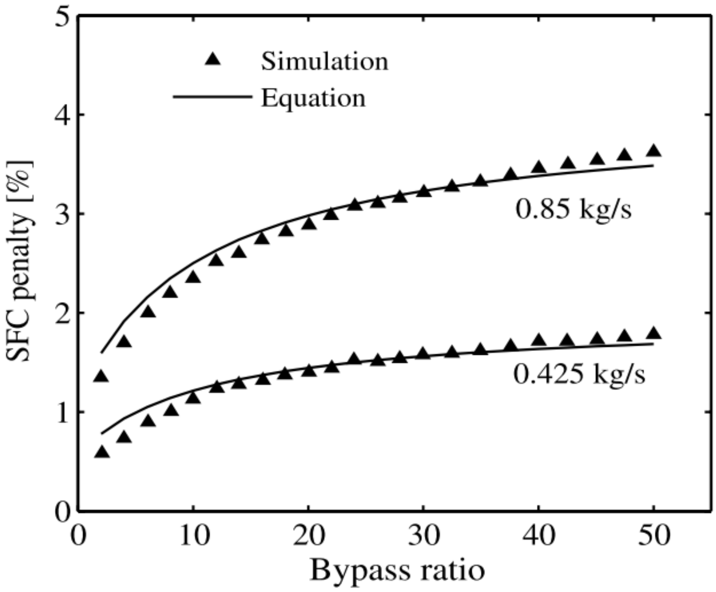

Figure 2.14: Relation between the bypass ratio and SFC penalty for two different bleed air requirements. Taken from Giannakakis [14]

Figure 2.14 shows the relation between the SFC penalty and the bypass ratio for a given bleed air requirement. The penalty on the SFC will increase as the bypass ratio increases. For the aircraft analysis however it is less important. The SFC penalty will be included in the final engine SFC. Furthermore the engine does not require drastic redesigns to accommodate the required bleed air flow. For the following research the engine off-takes will not be taken into consideration.

3

Simulation Tools Review

To calculate the installation penalty several computer simulation tools are available. First discussed is the ”Initiator tool box” of the TU Delft. It comprises many separate modules made in Matlab. Secondly a commercial program ”FlightStream” of the Research in Flight Company is discussed. FlightStream is a vorticity potential flow panel solver. To investigate the usability and accuracy of the program, it is validated with experimental data of the Common Research Model (CRM) developed by the National Aeronautics and Space Administration (NASA). Thirdly to establish a relation between engine bypass ratio, engine geometry and specific fuel consumption (SFC) an engine design tool by Proesman [37] is discussed.

3.1. TU Delft Initiator

The ”Initiator” is a Matlab tool developed by the TU Delft and to be used in the conceptual design phase. It offers the possibility to quickly generate designs from top level requirements such as missions profiles and payload requirements [11]. The tool uses a combination of statistical, semi-empirical and physics based modules to get to a converged aircraft design. The Initiator consists of sizing as well as analytical modules. These modules can be linked together to perform a design optimisation.

3.1.1. Initiator solving scheme

The Initiator uses top level requirements for inputs, such as passenger count, payload mass, cruise Mach number, cruise altitude and a mission profile. The solver procedure for the ”DesignConvergence workflow” module is given in Figure 3.1.

Based on a reference database and top level requirements, a Class 1 weight estimation is made. By using sizing rules and user-specified input on the aircraft configuration, the geometry of the aircraft is determined. Based on this geometry the weight and aerodynamic properties are estimated. The analysis results, such as operational empty mass (OEM), drag polar and specific fuel consumption (SFC), are fed back to the first module. This module uses the input to recalculate the maximum take-off mass (MTOM). This loop terminates once the Class 2 weight estimation at iteration i is within a predefined tolerance with respect to the value at iteration $i-1$, thus implying that the Class 1 weight estimation and Class 2 weight estimation have converged.

The following loop, the ”Mission Analysis” (MA) module, is run. It calculates new fuel fractions based on a more accurate analysis of the mission profile. The module is sensitive to changes in the centre of gravity. It also uses the trimmed drag polar. After the Class 2 loop is converged, the Mission Analysis loop runs. The solver then returns to the Class 2 loop. It stops when the difference in Class 2 weight between two subsequent iterations falls below the threshold.

In the final loop the empirical methods to predict the fuselage weight and the wing weight are replaced by two more advanced methods. The fuselage weight estimation module depends on various combinations of critical loads (inertial, aerodynamic, taxi). Based on these load cases, the primary structural components (skin panels, frames, stringers) are sized and their weight is estimated. Similarly, the weight of the wing is estimated based on gust loads or manoeuvre loads, whichever prevails.

---

[1] obtained from: `http://fppwiki.lr.tudelft.nl/index.php/Synthesis/Initiator` [accessed on: 25-06-2020]

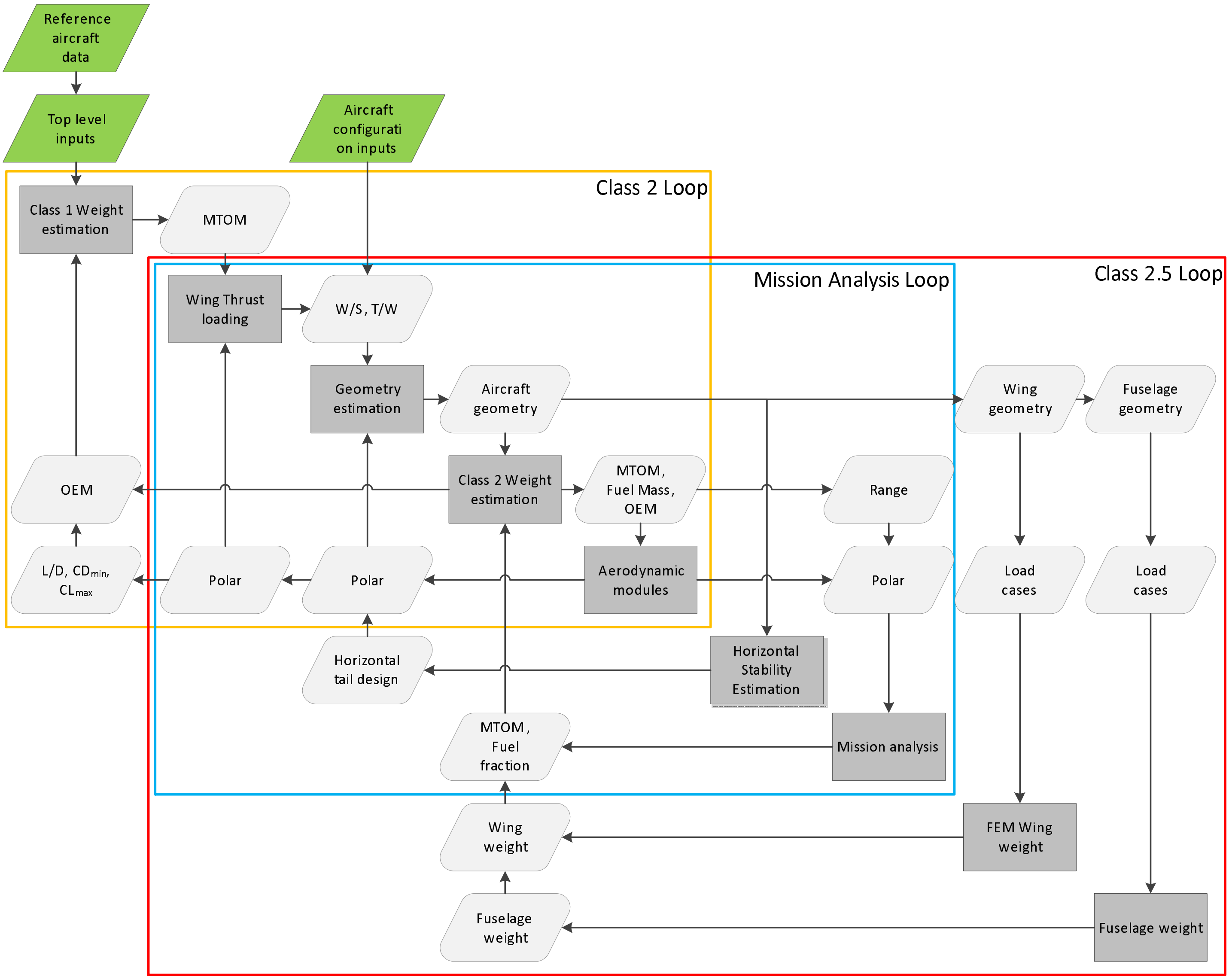

Figure 3.1: Initiator flowchart adapted from Initiator documentation[1]

Both the fuselage and wing weight estimation depend on the results of the aerodynamic analysis, as well as an estimation of the mass distribution. The calculated wing and fuselage weights are added to the results from the ”Class 2 Weight Estimation” for all other aircraft components. The resulting ”Class 2.5” weight prediction iterates until it converges below a user-defined threshold.[2]

3.1.2. Engine integration

The engine is sized in the ”Geometry estimation” module. The engine size is based on reference data, the required thrust and the bypass ratio. The thrust for the aircraft is based on the required cruise Mach number. The bypass ratio and the engine SFC are provided as an input value. The engine length and diameter are calculated using empirical relations given by Raymer [38]. The nacelle sizing depends on the engine diameter and the specified bypass ratio. The engine diameter and length can also be specified manually in the input file.

The engine location is specified in the input file. The location is defined using 4 values. Each value is a fraction of a wing or engine dimension. The first value defines the engine location with respect to the chord. A zero (0) value corresponds to the leading edge, a one (1) value represents the trailing

---

[2] obtained from: `http://fppwiki.lr.tudelft.nl/index.php/Synthesis/Initiator` [accessed on: 25-06-2020]

edge. The second value represents the spanwise location. The actual spanwise placement might differ slightly since the programme tries to fit the pylon to a wing spar. The third value specifies the chordwise location similar to the first value. Instead of using the chord as a reference, the engine length is used. The fourth and final value specifies the vertical location when looking from the front. The distance between the engine nacelle and main wing can be modified by this value.

Using the engine dimensions the engine weight follows from the Class 2 weight estimation. The landing gear is modified to make sure the ground clearance is sufficient. The engine location is used to determine the thrust vector location. The vertical tail is currently modelled using a tail volume coefficient, and does not account for an one engine out condition. The pylon is not sized properly in the current version. The pylon weight is not calculated in the current version.

3.1.3. Drag module

The drag components for the aircraft are calculated with the ”drag module”. The drag module calculates the zero-lift drag, wave drag and lift induced drag.

Zero-lift drag

The zero-lift drag is calculated using the parasite drag module. The module calculates the drag for the wing, fuselage, vertical tail, horizontal tail and nacelle. The pylons are currently not taken into account.

The major contributor to the zero-lift engine drag is the nacelle. The equations used for the calculation of the zero lift drag follow from Raymer [38]. Again for conventional aircraft configurations the pylons are not included in this analysis. The transition point from laminar to turbulent flow is first calculated. This transition point is then used to determine the skin friction coefficient using a look up graph from Roskam [41]. The zero lift drag follows from the friction coefficient and the wetted area. A direct relation between the two parameters is present. The interference effects between the pylon, nacelle and wing are accounted for in a correction factor, like the one used by Raymer. Nevertheless this factor is calculated using an unreferenced formula and gives rather low values compared to what Raymer suggests.

Wave drag

The wave drag module is quite extensive and calculates the wave drag for the wing and fuselage, however the nacelles are not included. The used method is based on the method as proposed by Feagin [12]: an empirical drag estimation devised in 1978. The downside of this method is that it mainly focuses on fighter aircraft, which generally don’t use podded wing mounted engines. Therefore the nacelle, or engine in general, is not taken into consideration.

Lift induced drag

The lift induced drag follows from the ”aerodynamics” module, which mainly consist of a wing analysis using AVL. AVL is a vortex lattice method (VLM) that describes the main wing as a vortex. The nacelles are not modelled and therefore the effects the nacelle might have during high angle of attack flight, are not captured. For cruise conditions the lift induced drag from the engines can be neglected.

3.1.4. Weight estimation

The current weight estimation consists of three main modules to calculate the structural weight. The main module is for the class 2 weight estimation and calculates the total operational empty weight (OEW) with corresponding c.g. location. The method uses the relations described in Torenbeek [49]. The engine weight is included in this module and is largely dependent on the required thrust.

Secondly an updated wing weight is calculated using a basic finite element method. It produces more detailed wing weights based on load cases and analytical relations, in stead of having to rely on statistical data.

Lastly the fuselage weight is estimated using a method as described by Schmidt [25]. The weight estimation is based on multiple load cases, such as cabin pressurisation, steady-state manoeuvre loads and landing loads. All the structural components in the primary fuselage structure are sized using two-dimensional satisfying requirements on bi-axial yield strength, global buckling, crippling, dimpling, and wrinkling. The fuselage skin is sized using a simplified buckling analysis for a curved stiffened panel. The remaining non-structural weights are estimated using empirical methods, similar to those of the class 2 method from Torenbeek [49].

3.1.5. Fuel consumption, SFC estimation

In the latest version of the Initiator the engine specific fuel consumption (SFC) is provided as an input. The aircraft's fuel burn during the mission follows from the ”MissionAnalysis” module. For each stage of the given mission profile, the required fuel burn is calculated based on the engine SFC and aircraft performance parameters, e.g. C_L , C_D and OEM. Based on the required fuel burn a maximum take-off mass can be determined.

3.2. FlightStream

In Figure 2.2.2 it was concluded that in order to quantify all the aerodynamic interference effects, a full 3D Navier-Stokes solvers must be used. However, this is not feasible in early design stages. For a sensitivity analysis of the variables, it is also not desirable due to the stringent hardware requirements. As a result, the possible variation options are limited. As an alternative, fast aerodynamic solvers, such as AVL (Athena Vortex Lattice), Tornado and Tranair by Boeing [35] may be used. FlightStream is a recent addition to this list and combines the strengths of the aforementioned programmes. For example FlightStream uses surface meshing in stead of a vortex lattice method which neglects thickness (e.g. AVL).

3.2.1. Program Description

FlightStream is a vorticity potential flow panel solver developed by the Research in Flight Company. It offers a quick detailed aerodynamic solution for the preliminary design phase. The program offers good fidelity inviscid load calculations for aircraft of a wide variety of configurations including blended bodies, canard configurations, and nearly any non-conventional geometry. Geometry consists of unstructured or structured surface meshes. For viscous analysis an additional viscous method can be used. This is however a simplification since the actual boundary layer is not modelled. The solution at the surface is used as a boundary condition for the viscous analysis. Other capabilities of FlightStream include: a compressibility correction and model expansion with engine intake with propeller and jetstream wakes.

3.2.2. Meshing

FlightStream support both structured and unstructured meshes. For the sake of solving time a structured mesh should be used. A structured mesh uses halve the number of elements, and is often better aligned with the flow direction. FlightStream can import a mesh directly or the built-in mesher can be used on a CAD model. Using the built-in mesher offers more flexibility if mesh parameters need to be changed.

Lifting surfaces, such as the wings and empennage, require a sufficient leading and trailing edge refinement. The leading edge refinement is indispensable for the separation computation. In general a good rule of thumb regarding mesh refinement for a lifting surface is to keep the aspect ratio of an element in the middle of the airfoil at around 2. Twice the width in spanwise direction compared to chordwise.

For non lifting bodies the mesh should only capture the geometry and does not require an intensive refinement. In case of the nacelles a leading edge refinement can be used when large forces are expected.

3.2.3. Solver physics

The solver in FlightStream is based on a vorticity solver, however it uses a new solution method suitable for unstructured meshes [1]. Where lifting line theory usually requires a structured mesh that is aligned to the flow, FlightStream can use arbitrary mesh shapes. As such the fast solver capabilities of a vorticity based solver are kept without the geometry restrictions.

Models

The surface vorticity data can be converted into force and moment results for the aircraft. The lift, drag and moments can be calculated using different models. These include vorticity and pressure for both lift and drag. The pressure model calculates the forces (Cx, Cy, Cz) along a bounding surface, the perpendicular plane to the force. For drag this plane is the height (thickness) of the airfoil. In order to use the pressure model, a very good mesh refinement to properly capture this is needed. For lift the surface is the chord length, which is much larger and easier to refine.

The moment can be calculated using a vorticity, linear pressure or non-linear pressure model. The non-linear pressure model should be used in case flow separation is expected. The moments are calculated with respect to a specified reference frame.

Viscous settings

The boundary layer can be set to laminar, turbulent or transitional. The transition marker can be shown in the solution. Separation can be enabled and is calculated based on the boundary layer settings. By specifying a certain surface roughness, the transition point can be influenced. The viscous drag is calculated by using one of two models: momentum integral or Reynolds averaged. By using the momentum integral method, the solution at the surface is used to calculate a boundary layer momentum. Integrating that solution gives the viscous drag. The second option is a more approximate method which corrects for the Reynolds number. It is preferred to use the momentum integral method.

Boundary conditions

The surfaces of the geometry are modelled as slip-walls or velocity and mass-flow inlets. For the lifting surfaces railing edges can be defined. The vorticity from lifting surfaces is shed at these trailing edges. The vertices at the junction of lifting and non-lifting edges can be specially marked for the vortex wake. The solver inputs include the angle of attack or the slide slip angle, and the free stream velocity.

Solver limitations

One of the biggest limitations of FlightStream is its inability to model shockwaves. In order to get realistic results only the subsonic, or early transonic regime, can be considered. The viscous analysis is an approximation because the boundary layer is not modelled completely. The drag increase due to separated flow is difficult to predict using the method currently in FlightStream.

3.2.4. Validation

Validation studies have been performed by the Research in Flight Company, results are shown in FlightStream workshops[3]. Despite the developers validation studies, an own validation study has been performed on the Common Research Model (CRM) developed by NASA. The focus lies on the 6th drag prediction workshop [48]. Part of the workshop focused on engine integration on the CRM model. The results from the drag prediction workshop can be used to validate the engine integration effects calculated by FlightStream.

Geometry description

The aircraft considered is the Common Research Model developed by NASA as a validation case for specific applications of computational fluid dynamics (CFD). Later this cultivated into the AIAA drag prediction workshops [51]. The design of the CRM aircraft is based on the DLR-F6.

Different variations for the CRM have been made. All to serve a different research purpose. The changes include: wing deformation due to lift, horizontal and vertical tail integration, and nacelle/pylon integration. The baseline however is the fuselage with the main wing. The fuselage is representative for a wide-body commercial transport aircraft, e.g Airbus A330 or Boeing 777. Furthermore, a wing-body fairing as well as a scrubbing seal for the horizontal tail are included [51].

The aerodynamic design of the wing has been done specifically for the CRM model. First, top level requirements on aircraft performance and preferred aerodynamic behaviour were set out. Design flight conditions include a cruise Mach of 0.85, C_L of 0.5 and a chord specific Reynolds number of 40 million. The behaviour requirements mainly focused on a good wing-body interaction. Firstly, it provides a simpler case for validation studies, and secondly, in case of fuselage mounted engines, such as business jets, the validation results can still be representative.

The geometry of the wing-body (WB) and the wing-body-nacelle-pylon (WBNP) are shown in Figure 3.2 and Figure 3.3.

---

[3] VSP workshop 2019 Non Linear

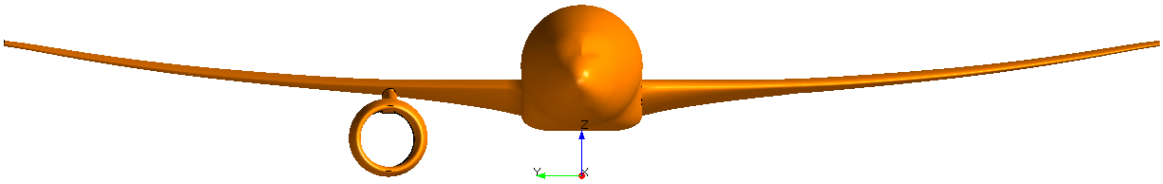

Figure 3.2: Front view of the CRM WBNP (left) and WB (right) configuration

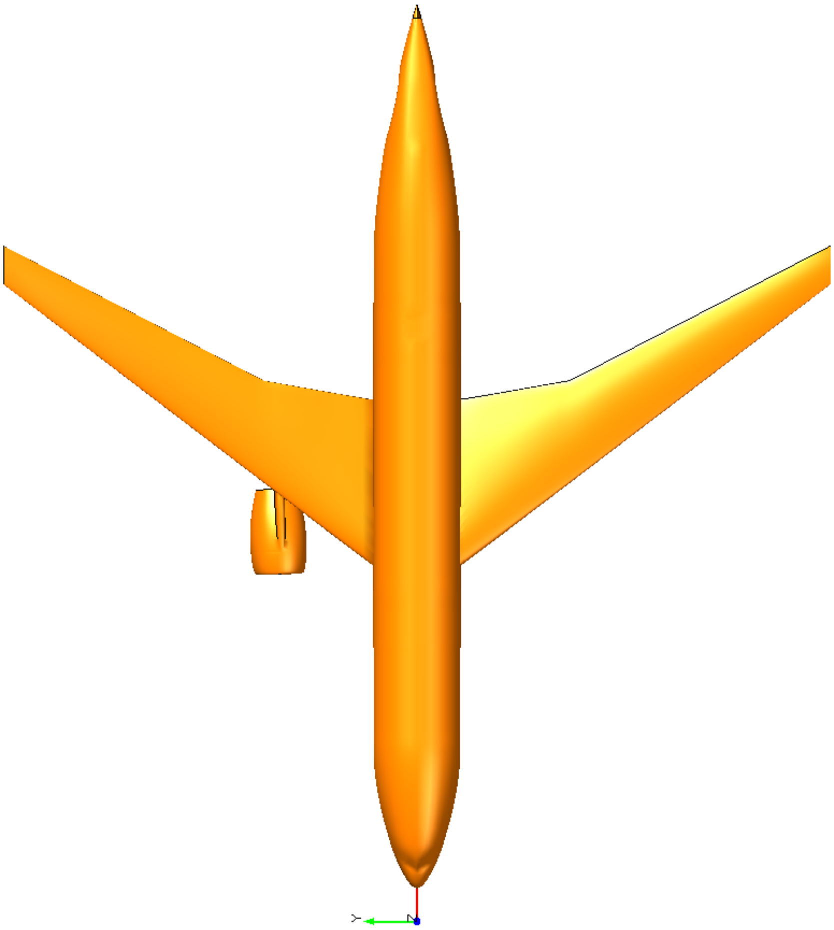

Figure 3.3: Top view of the CRM WBNP (left) and WB (right) configuration

The CAD geometry as shown in Figure 3.2 and Figure 3.3 has the same dimensions as the scaled down windtunnel model showed in the Appendix (Figure A.1). The reference location used for the moment is also similar to the windtunnel model.

Data

The data used for validation follows from two experimental studies at two different windtunnels: the Langley National Transonic Facility (NTF) and the NASA Ames 11-ft wind tunnel. Tests have been performed for Mach numbers ranging from 0.7 to 0.92. The angle of attack has been varied from -3deg to 12deg. Generally the angle of attack increment is 1deg. Near the transition point, from 2deg to 5deg, a smaller 0.25deg increment is used. More detailed runs to study only the separation bubble used an angle of attack range from 2deg to 5deg [4].

The runs are performed at three different Reynolds numbers. These include Re 5 million, Re 19.8 million and Re 30 million. All based on the chord reference length. For the validation analysis in this thesis, the results for Mach 0.7 with a Reynolds number of 5 million are used. FlightStream has no capabilities to capture shock waves, which are in fact present for Mach numbers larger than 0.7. There are also results available for configurations with the tail included, but they do not include the nacelle and pylon. Therefore for this validation only the wing-body (WB) and wing-body-nacelle-pylon (WBNP) are considered.

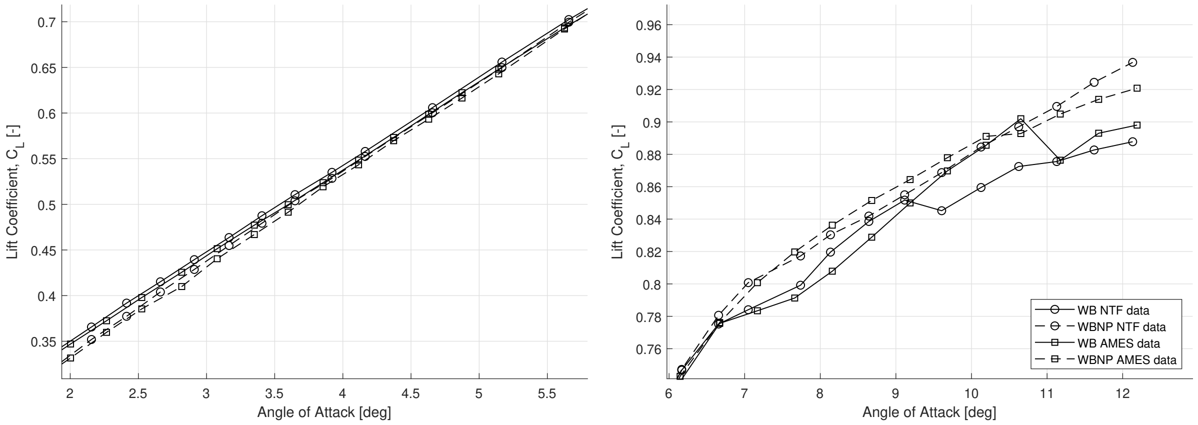

Figure 3.4: Experimental lift coefficient results for CRM WB and WBNP configurations at Mach 0.7, Re 5 million. The results are for the scaled windtunnel model.

The lift coefficient as given in Figure 3.4 is quite similar for both the WB and WBNP configurations. For lower angles of attack the added pylon and nacelle reduce the lift coefficient. This is consistent with the theory from Figure 2.2.2 that explains the loss in lift for the main wing due to the presence of nacelles. Contrary to the slight loss in lift at low angles of attack, for higher angles of attack the lift coefficient becomes slightly larger. Possibly because at higher angles of attack the (symmetrical) nacelle will produce a lift. This would also explain the slow tapering of the two lift curves. If the angle of attack increases, the effect of nacelle lift becomes more pronounced and the loss in lift produced by the wing is compensated. It is difficult to say if the nacelle could produce a similar lift force compared to the wing at that section. Another explanation could be that the presence of the nacelle and pylon affect the local flow in such a way that separation is postponed.

---

[4] obtained from: `https://commonresearchmodel.larc.nasa.gov/experimental-data/` [accessed on: 18-03-2021]

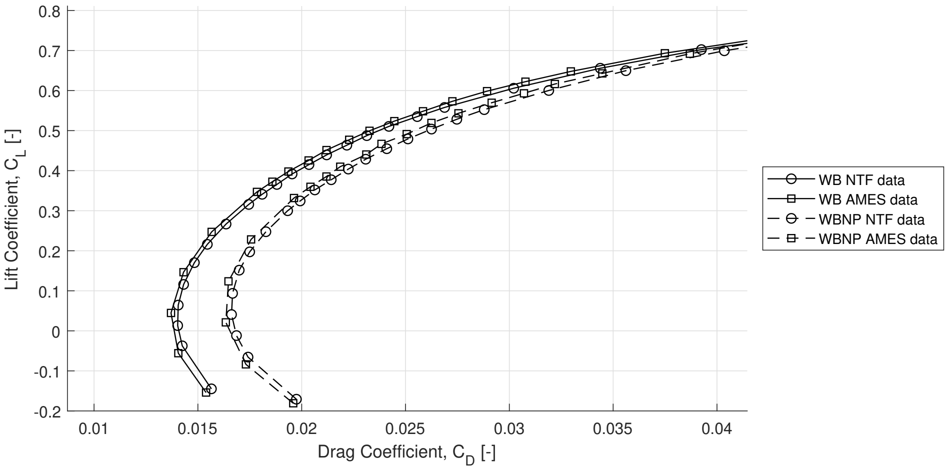

Figure 3.5: Experimental Drag polar results for CRM WB and WBNP configurations at Mach 0.7, Re 5 million. The results are for the scaled windtunnel model.

The aerodynamic performance of the two configurations is shown in the drag polar in Figure 3.5. At smaller lift coefficients up to roughly 0.6 the WB configurations has a lower drag coefficient compared to the WBNP. This is in line with what is to be expected. However for higher lift coefficients, the difference in drag coefficient becomes almost zero. From the lift curves it is clear that the effect on the lift coefficient after separation is smaller for the WBNP. The smaller separation area means less pressure drag and a larger lift coefficient.

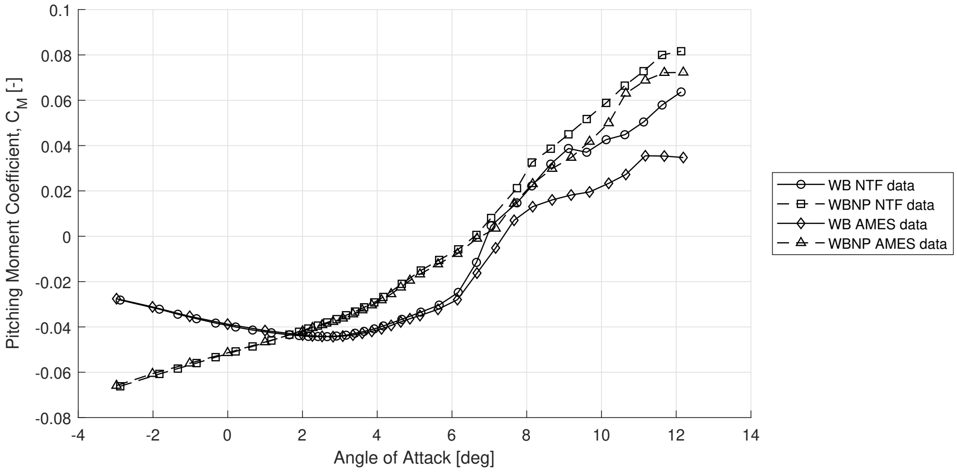

Figure 3.6: Experimental Pitching moment results for CRM WB and WBNP configurations at Mach 0.7, Re 5 million. The results are for the scaled windtunnel model.

The largest difference can be observed in the pitching moment. Figure 3.6 shows the pitching moment for the angle of attack range. The WB configuration shows a negative slope up to an angle of attack of 3deg. The WBNP has a positive slope in the entire angle of attack range. It should be noted that the reference point is fixed and does not represent the c.g of the aircraft. Drawing conclusions regarding the stability is not possible. The difference between the WB and WBNP configuration is however still of significance.

The differences between the two windtunnel test locations are negligible, as was concluded by Rivers [39]. There is a 3 and 5 drag count difference, at design point C_L 0.5, between the two locations for the WB and WBNP configuration respectively. At the design point the lift curve and pitching moment curve show very small differences between both windtunnel locations.

Solver set-up

The flight conditions follow from the experimental data described in Rivers [39]. The angle of attack range is from -3 to 12 degrees. The Reynolds number in the experiments is 5 million. The Mach number used is 0.7 and the geometry follows from the CRM website and is scaled to the windtunnel model. For the viscous settings the transitional boundary layer was used with the momentum integral viscous drag model. Flow separation was enabled as well as the compressibility correction.

Typical solver times are in the range of 1min to 5 min per angle of attack step. All depending on the mesh refinement used. Figure 3.7 shows the residuals converging to the specified threshold before going to the next angle of attack point.

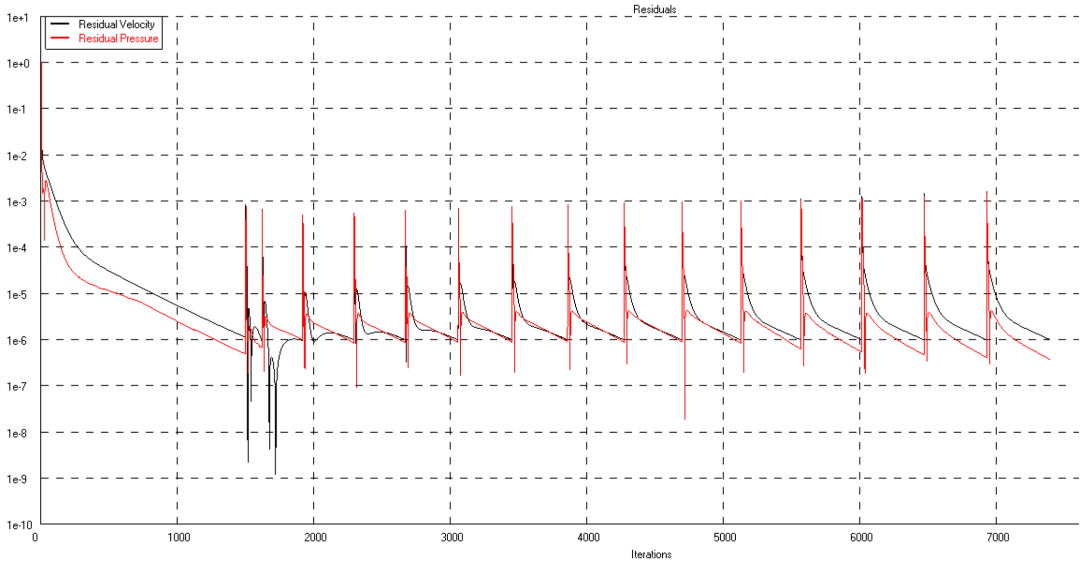

Figure 3.7: The residuals for an angle of attack range: -3 to 13 calculated by FlightStream at Mach 0.7, Re 5 million. For the scaled CRM WBNP model.

Results

Figure 3.8 shows the calculated aircraft lift coefficient (C_L) for the WB configuration (in blue). The experimental data from both windtunnel experiments are also given.

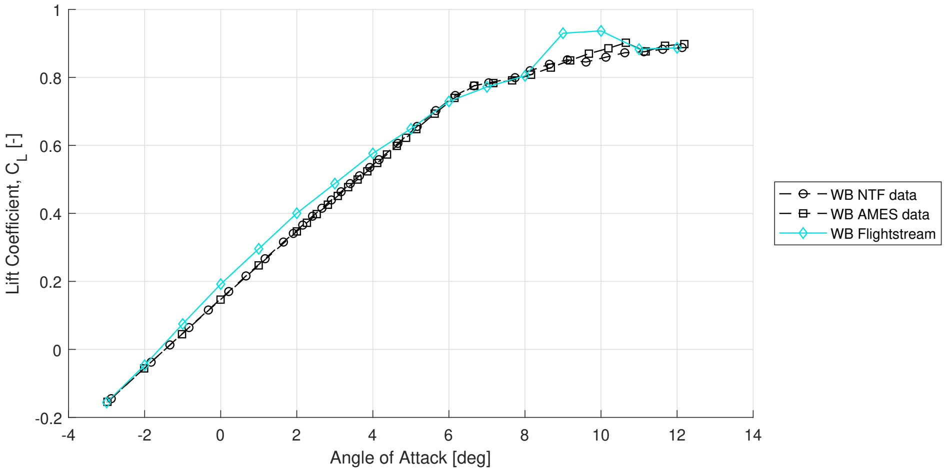

Figure 3.8: Comparison WB CL data experimental and calculated by FlightStream at Mach 0.7, Re 5 million, for the scaled CRM model.

In general, there is a close coherence between the experimental results and the numerical results produced by FlightStream. Two differences can be observed between the numerical and experimental results. Firstly, the sudden increase in lift coefficient at 9 degrees angle of attack. FlightStream is able to capture the start of separation well. The reason for the sudden jump is likely to be a numerical error, or mesh related. For the WBNP configuration no such jump is present, see Figure 3.9.

The second deviation from the experimental data happens between -1 and 5 degrees angle of attack. The lift curve slope calculated with FlightStream is slightly larger compared to the experimental data. At roughly 2 degrees the slope decreases again and the values get closer to the experimental results. The kink can be explained through the transitional boundary layer. There is a clear kink visible when a large portion of the airflow changes from laminar to turbulent. The effect is much more pronounced in FlightStream than in the experimental results. For the WBNP configuration, in Figure 3.9, the effect is magnified even further.

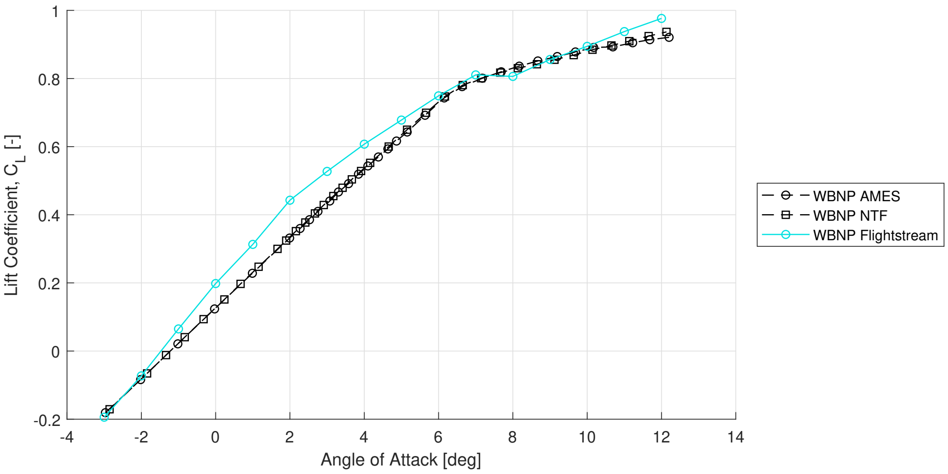

Figure 3.9: Comparison WBNP CL data experimental and calculated by FlightStream at Mach 0.7, Re 5 million, for the scaled model.

The lift curves calculated by FlightStream show resemblances to the experimental data, however there are several regions where FlightStream deviates. Although the point of separation can be estimated rather well, the results after this point are different. Estimating the maximum lift coefficient will therefore be difficult. The other difference is with the transition point. The ability to use a transitional boundary layer is nice. The transition from laminar to turbulent is a source of error when the results are compared to the experimental data. It becomes worse for the WBNP configuration.

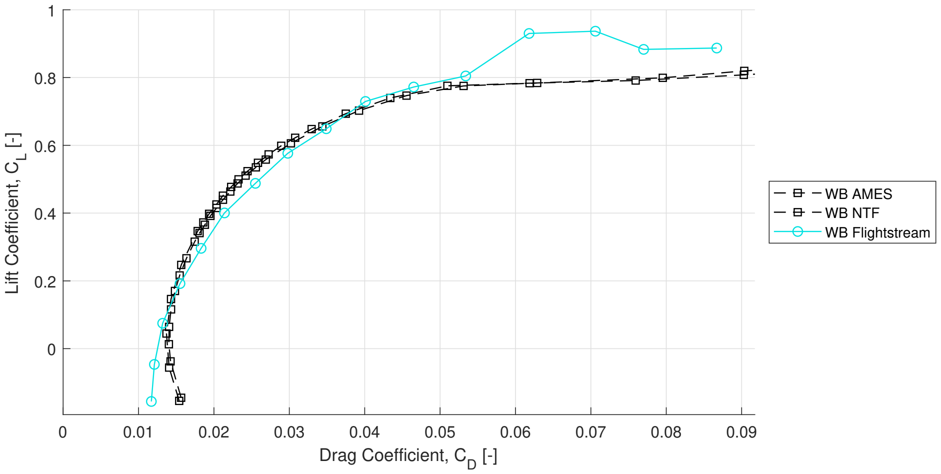

Figure 3.10: Drag polar plot for the CRM wingbody configuration with FlightStream results at Mach 0.7, Re 5 million, for the scaled model.

Figure 3.10 shows the polar for the WB configuration whereas Figure 3.11 shows the polar for the WBNP. Both graphs show the limitations of a vorticity solver when calculating the drag coefficient. The viscous drag estimation is not sufficient to capture the correct values. For the WB configuration at lower lift coefficients the absolute values are of the same order of magnitude. At negative lift coefficients there is a large difference. The same can be seen at large lift coefficients, showing the same sudden increase in lift coefficient as in the lift curve (Figure 3.8). The slope of the FlightStream curve is different for the whole range compared to the experimental data.

The large drag increase after the separation is lacking. This is best visible for the WBNP case in Figure 3.11. For the WBNP configuration the drag is lower for all values of C_L, whereas the WB configuration showed a better estimation for the absolute values. The slope of the curve for the WBNP is closer to the experimental data.

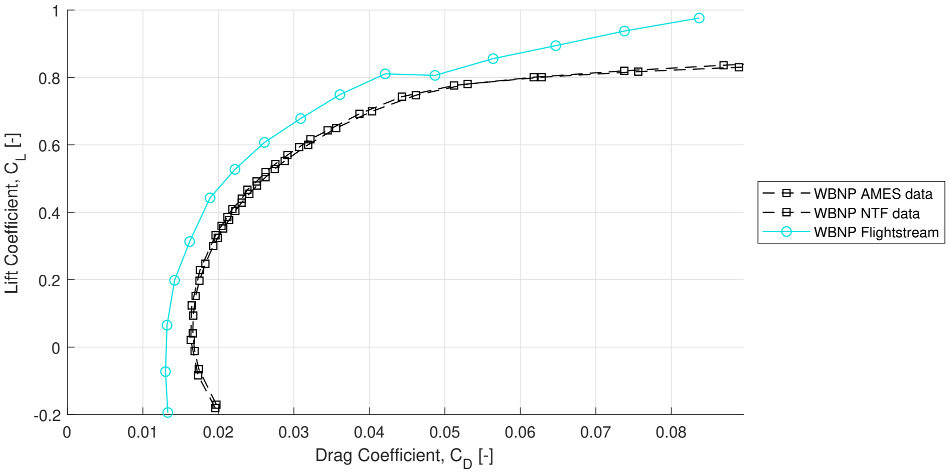

Figure 3.11: Drag polar plot for the CRM wingbody + nacelle and pylon configuration with FlightStream results at Mach 0.7, Re 5 million, for the scaled model.

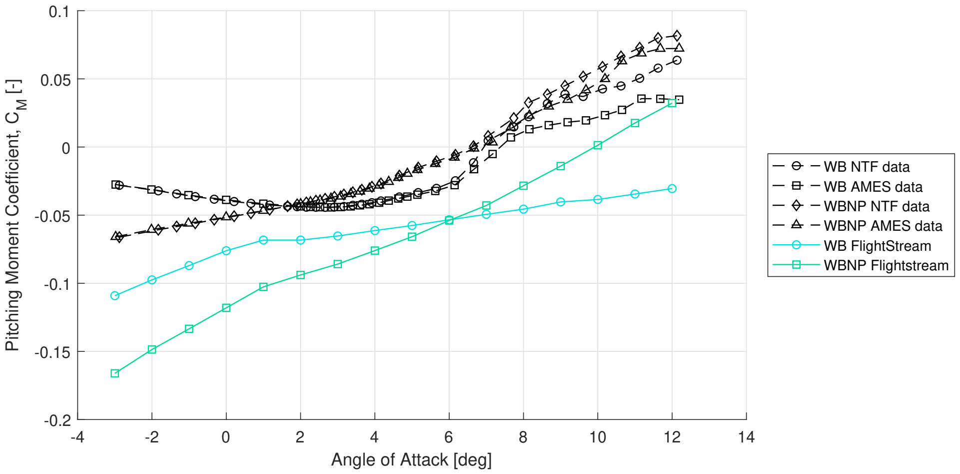

Figure 3.12: Pitching moment plot for the CRM wingbody + nacelle and pylon configuration with FlightStream results at Mach 0.7, Re 5 million, for the scaled model.

The pitching moment calculated in FlightStream is shown in Figure 3.12. The absolute values for the pitching moment coefficient are different for the whole range of angles of attack. There is a trend that is captured for the WBNP configuration. The slopes of both the FlightStream results and the experimental results are comparable. The WB configuration however is quite different up to 2 degrees angle of attack. The experimental results show a negative slope, compared to the positive slope of the

FlightStream results. Estimating the pitching moment for non-linear solutions is difficult because not only the magnitude of the forces is important, but also the location. Even if the calculated total forces (lift and drag) are close to the experimental data, the moment can be different. This is the case when the resultant lift and drag force is in a different location compared to the experimental data.

Conclusion

FlightStream has good capabilities when it comes to finding aerodynamic trends. Absolute values are sometimes harder to capture. The results are more accurate at lower angles of attack when separation has not yet occurred. There is a clear distinction between the WB and WBNP configuration in pitching moment curves. The absolute values are not correctly predicted. For the slope of the lift curve and the increase in drag, the effects are harder to quantify. It already starts with the inherently small difference between the WB and WBNP as was seen in Figure 3.4 and Figure 3.5.

3.3. Engine Design Tools

To calculate the installation penalty in terms of fuel consumption, the engine performance needs to be determined. The ”fuel consumption” of an aircraft without an engine needs to be determined first before the fuel consumption of an aircraft as a whole can be assessed.

The largest contributor to the Engine SFC improvement has been the increase in bypass ratio. Other factors have also been important, but when considering the effect on engine design, the bypass ratio is the most significant contributor. With a larger bypass the engine size increases, which can have detrimental effects, such as increased drag, less ground clearance and increased weight. Other engine improvements (e.g. materials) have little effect on the external engine design.

3.3.1. Python parametric engine design

A number of engine design tools are available within the faculty. The parametric engine design tool, built in Python by Proesman[37], has been tested for its suitability for this research study. The simulation program is based on first order principles and can be used to size an aero-engine for a small set of inputs. The methods are based on the principles described by Mattingly [28]. It would be favourable if this tool can be used to determine the engine SFC and other performance factors, as well as the engine size and weight. It has been validated with the CFM56 and GE90 aero-engines [37].

The goal is find a relation between the bypass ratio and the SFC. To determine the engine performance (SFC), more inputs are required than can be provided. In the most simple case the bypass ratio, compressor (LPC & HPC) pressure ratios, and the turbine entry temperature (TET) are needed. The values that work for the CFM56 engine with a bypass ratio of 5.6 do not work for a bypass ratio of 10 or higher. When increasing the bypass ratio only, the required fan power becomes too large, causing flow stagnation through the turbine. An alternative is to use a set of parameters which work for the entire range of bypass ratio’s. However in that case the pressure ratio’s will result in the best SFC and efficiency for 1 bypass ratio. It is possible that for large bypass ratio’s the SFC and efficiency gains are far from optimal and only a small gain is observed. If the pressure ratio’s are slightly changed, far within the physical limitations, a larger SFC gain is observed.

In order to get a feasible design for different bypass ratio’s (and the other engine parameters), pressure ratio’s and the turbine entry temperature need to be optimised. It is not straight forward to do so, since the optimisation has multiple optimisation goals. For example: the lowest SFC for the highest efficiency for the lowest weight and size. To test a possible optimisation of input values, a minimise function with a Sequential Least Squares Programming algorithm from SciPy has been used. SciPy is an open-source Python library used for scientific computing and technical computing. The flight conditions and the thrust requirements are kept constant. The bypass ratio and the flight conditions correspond to the CFM56 engine. The limits of the design vector is shown in Table 3.1.

Table 3.1: Design vector lower and upper limits. The bypass ratio, flight conditions and thrust requirements are kept constant.

	Fan PR [-]	LPC PR [-]	HPC PR [-]	TET [K]
lower	1.2	1.2	10	1100
upper	1.8	2	20	1700

Four different objective functions were used. Firstly, the optimiser was to used to minimise the specific fuel consumption. Secondly, to optimise the overall efficiency (a combination of mechanical and thermal efficiency). The next optimisation was to minimise the engine mass. Lastly, the overall efficiency divided by the engine mass was maximised. The results are shown in Table 3.2.

Table 3.2: Optimisation results for different optimisation criteria/variables. For a bypass ratio of 5.7 and constant flight conditions and thrust requirements.

Optimisation variable	Fan PR [-]	LPC PR [-]	HPC PR [-]	TET [K]	Overall efficiency [-]	Engine mass [kg]	Fan diameter [m]	TSFC cruise [lb/lbf.hr]
TSFC	**1.8**	**2.0**	**20.0**	1448	33.4%	3020	1.77	0.566
Overall efficiency	1.7	**2.0**	**20.0**	1442	33.4%	3029	1.78	0.566
Engine mass	**1.8**	**1.2**	**10.0**	**1700**	24.8%	1613	1.46	0.762
Efficiency/ engine mass	**1.8**	**1.2**	**10.0**	1525	27.4%	1755	1.54	0.688

In Table 3.2 the values in bold are the input values that have reached a limit. A fuel efficient engine will be large and heavy, while a lightweight engine has a bad efficiency. This is visible for the TSFC optimisation variable. The pressure ratio’s are maximised to maximise the thermal efficiency. The engine weight however increases, and is much larger compared to the CFM56 (2331 kg). Mainly because the large pressure ratio’s require larger compressors. Contrary, when optimising for engine mass, the opposite happens and the pressure ratio’s are reduced. As a result, the engine efficiency and also the TSFC drop significantly.

Combining the parameters in one cost function by adding weights does not yield valid results either. Mainly because the design goals, e.g. TSFC/efficiency and engine weight, require opposite design strategies. An efficient engine will result in a large weight, and a light engine will have an appalling efficiency. Defining weights will slightly improve the result, however if either design objective is favoured, the optimiser will converge to a local minimum for one objective.

An optimisation is not possible in its current tested form, and for the sake of time and scope of this research, it is opted to go for a statistical approach and usage of data of existing engines. A pitfall in using statistical data is the lack of data points. Although there is data available of comparable engines from the same era, finding engines with similar thrust ratings is challenging. For similar thrust rating newer engines often show performance and efficiency gains from optimised components. Although this research focuses more on the installation penalty and relative differences, the absolute values can be taken with a margin. These possible errors do need to be noted in the final results.

4

Methodology

The following Chapter describes the methodology used to answer the research questions. First some background is provided based on the literature and analysis tools review. Based on the conclusions that are drawn from these Chapters, the approach is modified. Next the aircraft geometry to be used is explained, followed by the engine determination. The engine size, weight, dimensions and specific fuel consumption are calculated. The next Section discusses the aerodynamic center evaluation using FlightStream. Theory on the method and a small validation study are given. After the section on the aerodynamic center, the equations and theory for the stability analysis are given.

4.1. Solution premise

Optimised aircraft design is a multidisciplinary problem. From chapter 3 it is shown that although there are several methods with accompanying software methods available, they all have shortcomings. The Initiator tool comes closest to a Multidisciplinary Design and Optimisation (MDO) result. Although the Initiator is closer to a Multidisciplinary Design and Analysis (MDA), no actual optimisation is done. In principle it includes all installation effects by modifying the aircraft completely. However making a fair comparison is not possible with so many aircraft parameters being changed. As such the tool makes it difficult to identify dependencies. The Initiator tool performs an optimisation, for almost all aircraft parameters. Modifying the Initiator tool such that it only modifies user specified variables is not wanted. The principle, on which the Initiator tool is built, requires all variables to change. If variables are being fixed, the complete solver structure needs to be modified. As a solution the following premise is suggested:

Is it possible to make a new engine work for a fully newly designed aircraft? However a large challenge arises when an existing aircraft is retrofitted with a new, often larger, engine. The Boeing 737 MAX is an obvious example. Therefore it is opted not to look for a full redesign of the aircraft when considering the installation penalty, but rather investigate the operational limitations of an existing airframe when fitted with a new engine. This means the aircraft flight performance will be investigated as well as a possible tail re-design. The reasoning follows from the 737 MAX case where the main problem was the longitudinal stability change due to the moved engine.

The design variables in this case are the engine location and the tail surface planform, both horizontal and vertical tails. The reason for changing the tail is to make it possible to compare the performance with no airframe changes, and to be able to check how much the tail must change to regain the old characteristics. The solution steps are shown in Figure 4.1.

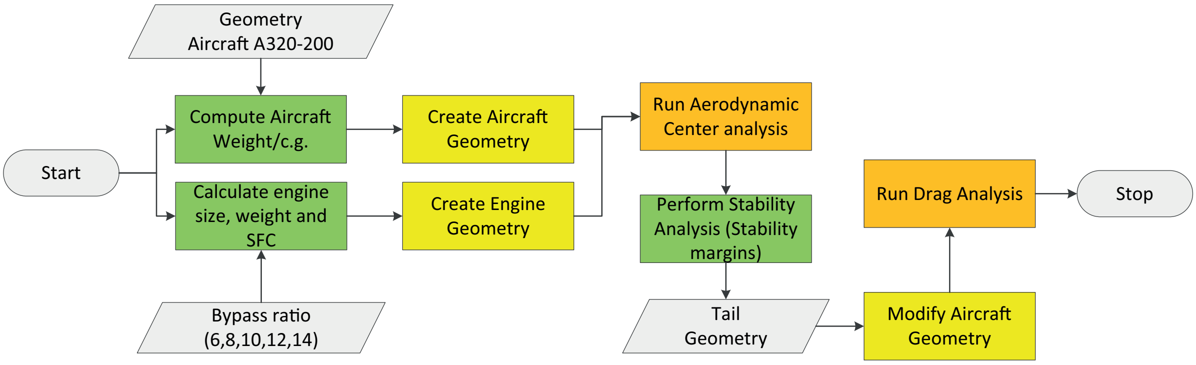

Figure 4.1: General flow diagram of the steps that will be taken for an engine retro-fit analysis.

It is prevalent that the analysis does not result into an optimisation problem. The goal first and foremost is to find the direct consequences of the engine installation. The next steps would be to go further and find the secondary effects which result from a changing airframe due to the changed engine.

4.2. Aircraft Geometry

In the previous chapter, the NASA Common Research Model (CRM) has been used for validation purposes. Windtunnel data is available for this aircraft model and is used to investigate the capabilities of FlightStream. For this research the focus will be on the A320, due to multiple reasons.

Firstly, there is quite some reference material of the A320 available, this allows for good reproduction of the geometry. The service manual [46] provides scaled drawings and weights for the aircraft, the drawings used are provided in Appendix C. The wing geometry follows from a previous Thesis report and paper by Orlita [33]. His research focused on the morphing spoilers, but as a part of his work, he reverse engineered the wing geometry from the book of Obert [30]. In the book the thickness distribution as well as the airfoil shape are described in graphs which have been interpreted by Orlita. For this research the wing airfoil shape and thickness have been used to reconstruct the wing in the 3D modelling program CATIA.

The second reason for using the A320 is the availability of a validated reference file in the Initiator tool. The goal was to use the Initiator tool for determining the installation penalty. The A320 has been one of the cases used in validating the Initiator tool.

Lastly it can be argued that for larger aircraft the engine installation is less critical. For the 737 MAX the ground clearance requirement was the main reason for relocating the new LEAP engine. If the airframe is larger, the ground clearance will be less of a problem. However for the new Boeing 777x, a somewhat similar trend is happening: older airframes are fitted with newer higher bypass ratio engines. The previous generation GE90 engine used a bypass ratio of 8 whereas the new GE9X engine uses a bypass ratio of 10. The increase in overall engine diameter is less drastic, from 3.926 m to 4.158 m.

FlightStream can read igs files exported from CATIA. An igs file contains the geometric data of the 3D object. Some CATIA functions however do not directly translate to a correct 3D CAD model in FlightStream. In some cases edges are merged when this is not desired, and some functions in CATIA, such as a sweep or revolute function, does not translate. For building the CAD geometry, a trial and error method was used to make the best CAD geometry for FlightStream. The 3D CAD geometry is required in FlightStream to enable the usage of the built-in aligned mesher tool. Creating a mesh with other programs resulted in errors or non-converge in FlightStream. The 3D model must be made with as few faces as possible. For the aligned mesher each face has to be defined separately. The faces must also be square, or at least with 4 edges for a good aligned mesh to be made.

4.3. Engine determination

The goal of this research is to investigate the trade off between improved engine performance and the negative effects on aircraft performance. The installation penalties have been described in Figure 2.4. For the analysis, a range of bypass ratios is chosen: 4, 6, 8, 10, 12, 14. Current turbofan engines range from 5 (CFM56) to 10 (CFM LEAP). For this research the engine can be regarded as a black box with only a few parameters. These include: engine Specific Fuel Consumption (SFC), nacelle width, nacelle height, engine weight and engine location. There are many factors that contribute to the engine SFC, the thrust it produces, and how large and heavy it will be. It is however not the goal to design a new engine, rather to just focus on possible effects on the aircraft. Therefore a simple statistical relation is used to link the bypass ratio to the aforementioned engine parameters.

The actual nacelle is often asymmetric and varies in thickness along the rotational axis. In this research the nacelle is axis-symmetric and the nacelle airfoil geometry is taken from the CRM model. In the CRM report [51] is not specified which airfoil shape is used. However the 3D aircraft model is made available. From the CAD model the nacelle airfoil geometry has been extracted. The nacelle is aligned with the incoming flow and has zero incidence angle.

4.3.1. Engine specific fuel consumption

In section 3.3 it is already concluded that designing an optimised engine for each bypass ratio is not favoured. It is therefore opted to use statistical data for the relation between the bypass ratio and specific fuel consumption. The data used is retrieved from the emission database (**ICAO Aircraft Engine Emissions Databank**) [1] as provided by the EASA. The data provided is for a large range of engines, but only provides the fuel flow at take-off, climb out, approach and idle conditions. For calculating the fuel burn in a mission, the fuel consumption during cruise conditions is required. Some example values for cruise SFC and take off SFC can be obtained from brochures and databases as found in Civil jet aircraft design by Jenkinson [24]. Generally these are older engines types, and are still a estimation because cruise conditions are not known. From this a correction of **1.8** is used to go from take off SFC to cruise SFC.

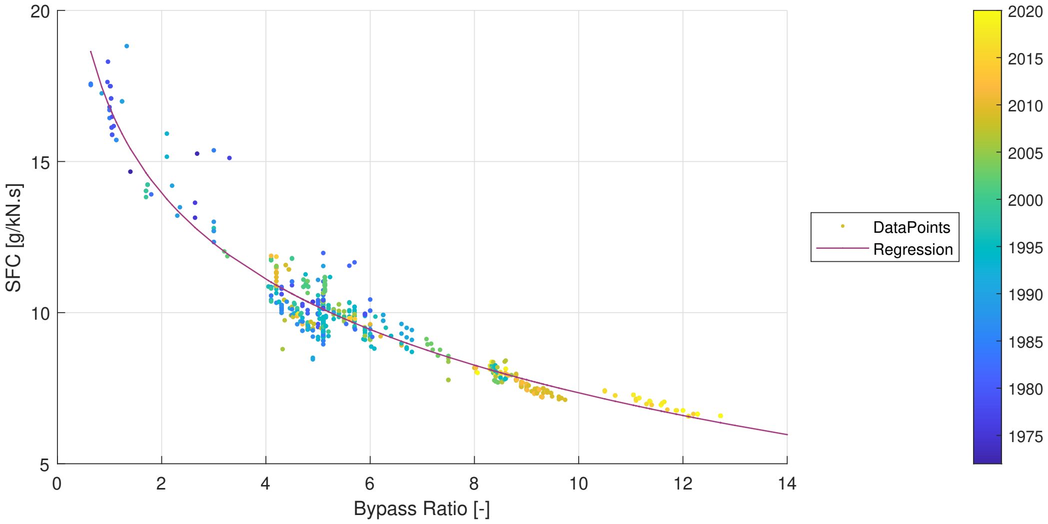

Figure 4.2: The take off specific fuel consumption plot against the bypass ratio for engines tested in ICAO emission databank. The datapoints are coloured by year of first inspection.

The engine SFC's are plotted in Figure 4.2. The graph shows a logarithmic relation between the bypass ratio and the SFC. A clear trend is visible, but for the large bypass ratio engines it is not evident all performance gain follows from the bypass ratio. The higher bypass ratio engines are newer, which means a more developed turbomachinary. Summarising, the improved SFC is not only due to the increased bypass ratio, but also due to improved pressure ratios and increased turbine entry temperatures. For the large bypass ratio's the trend looks to be too optimistic.

In Table 4.1 the calculated values for the SFC are given. The values are based on the regression curve shown above. The formula for the regression curve is:

$$SFC = -4.11 \ln(BPR) + 16.80$$
$$R^2 = 0.9345$$

---

[1] obtained from: `https://www.easa.europa.eu/domains/environment/icao-aircraft-engine-emissions-databank` [accessed on: 28-03-2020]

Table 4.1: Calculated take off and cruise SFC for different bypass ratios

		BPR [-]					
		4	**6**	**8**	**10**	**12**	**14**
Take off	**[g/kN.s]**	11.1	9.4	8.3	7.3	6.6	6.0
Cruise	**[g/kN.s]**	20.0	17.0	14.9	13.2	11.9	10.7

4.3.2. Engine dimensions

For the aerodynamic analysis, the engine (nacelle) dimensions have to be established, most importantly the nacelle outer diameter and nacelle length. The nacelle dimensions are often not provided for the engines themselves and have to be estimated based on the bare gas turbine size. It is opted to base the engine dimension on statistical data since very few engine parameters are known. Firstly the gas turbine dimensions must be determined based on the thrust requirement and bypass ratio. From the engine diameter a statistical relation can be used to estimate the engine length. Lastly, the nacelle dimensions are calculated using the engine dimensions of the CFM56-5 and CFM LEAP-1A used on the Airbus A320.

Table 4.2: Gas turbine size parameters for modern gas turbines, obtained from EASA type certification documents

Gas Turbine	**BPR**	**Diameter**	**Length**	L_n/D_n	**weight [kg]**	**thrust [kN]**
IAE V2527-A5	4.8	1.682	3.201	1.90	2404	118
Pratt & Whitney PW6162	4.9	1.52	2.7	1.78	2289	107
Rolls Royce BR700-715	4.68	2.128	3.738	1.76	2085	95
CFM56-5	5.5	2.1	2.6	1.14	2331	117
LEAP-1A	11	2.56	3.3	1.29	2990	140
PW1100G	12.5	2.224	3.401	1.53	2857	147
Rolls Royce Trent 500	7.6	3.374	4.689	1.39	4990	275
GE CF6-80	5.92	2.89	4.277	1.48	5091	304
GE90	8.4	3.95	7.26	1.84	7893	360
GEnx-1B	8.8	3.533	4.95	1.40	6147	339
GE9x	9.9	4.158	5.69	1.37	9630	490

Typically, the engine size follows from the required thrust. This can also be seen in the data in Table 4.2. In the scenario where the airframe stays the same, the thrust will likely remain the same as well. Therefore a relation between the bypass ratio and the diameter is favourable.

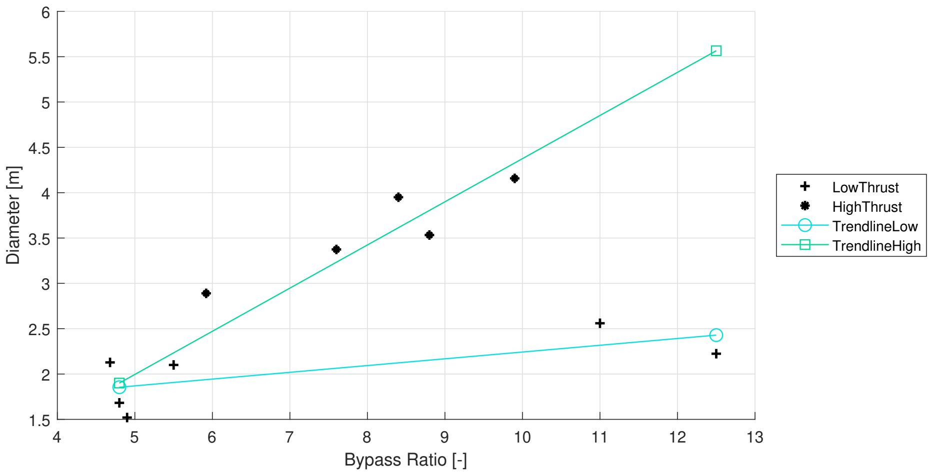

Figure 4.3: Relation between the diameter and bypass ratio from engine in Table 4.2. Low thrust up to 150 kN, and high thrust 150+ kN.

Figure 4.3 shows the relation between the bypass ratio and engine diameter. There are two trends visible for 'low' and 'high' thrust engines. In the past a larger bypass has been synonymous with a higher thrust engine. The current generation engines for single aisle aircraft are using a significant larger bypass ratio which throws off the curve. Therefore only the same thrust rated engines are used to determine a relationship between BPR and engine diameter. Unfortunately the sample size is rather limited in this scenario.

With the diameter known, the length of the engine can be determined from the data in Table 4.2. When plotting the diameter versus length, a linear relation is found (see Figure 4.4). For large bypass engines the gas generator is mainly used for power generation for the fan. The major portion of the thrust follows from the fan. Therefore it is expected that the engine length would also depend on the bypass ratio. For these engine examples however this is not the case and a fairly linear trend is observed.

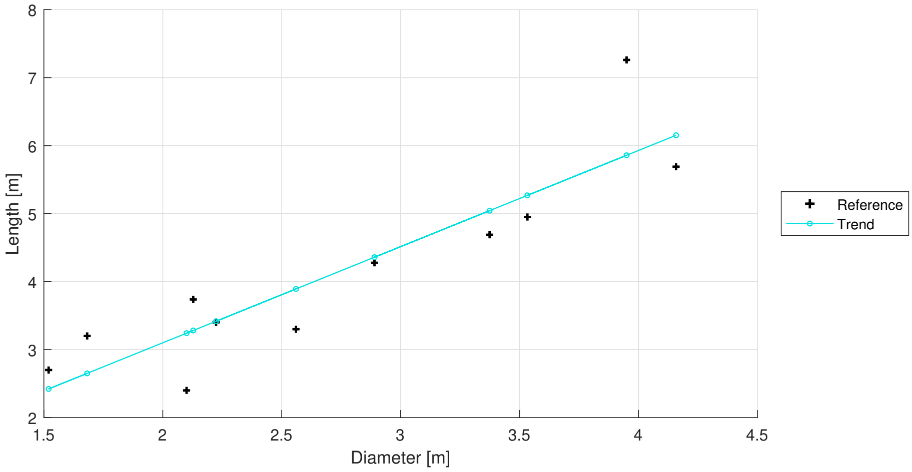

Figure 4.4: Relation between the engine diameter and engine length from engines in Table 4.2

The last step is to convert the engine dimensions to nacelle dimensions. Figure 4.5 shows the bare CFM56-5 engine as mounted on the A320-200. These dimensions follow from the service manual, but can also be found in other documents. From the most left picture in Figure 4.5 the nacelle is larger compared to actual engine. A fact made more clear in Figure 4.6 which shows the nacelle dimensions for the CFM56-5 for the A320-200.

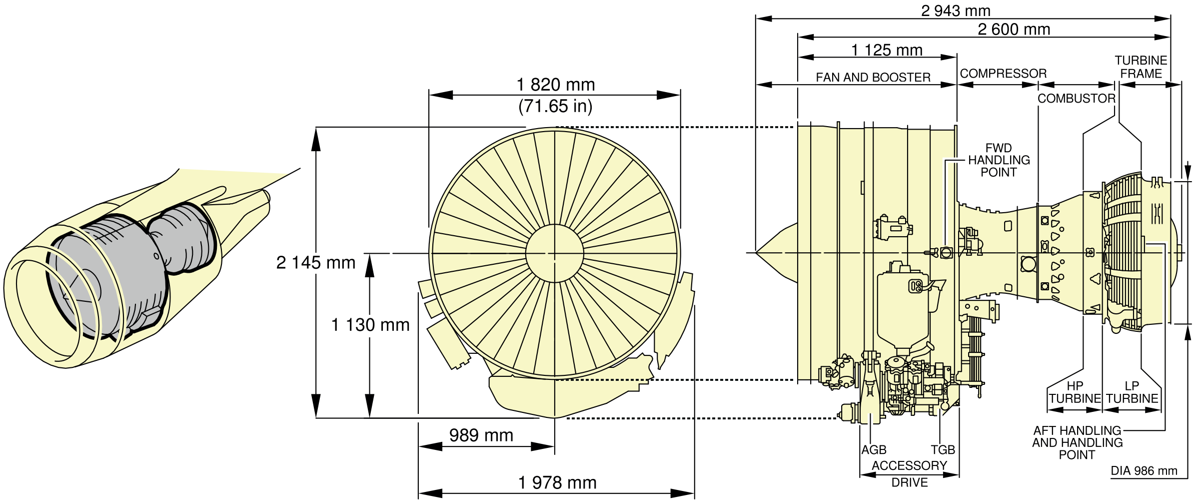

Figure 4.5: Technical drawing of the bare CFM56-5b engine as mounted on the A320-200 series, taken from A320 service manual [46]

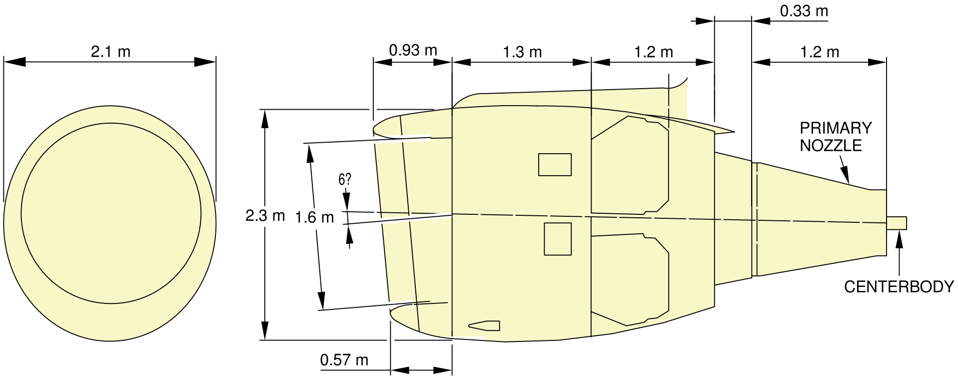

Figure 4.6: Technical drawing of the CFM56-5b nacelle as mounted on the A320-200 series, taken from A320 service manual [46]

The bare CFM56 engine with accessories is 1.978m wide, including the nacelle the width is 2.1m. The height of the bare CFM56 engine is 2.145m, including the nacelle, the engine is 2.3m high. A 6% and 7% increase respectively. The nacelle here only serves as a protection for the engine accessories. The nacelle length however is significantly larger. Largely due to the required inlet and long exhaust nozzle to facilitate flow mixing. The actual nacelle length is difficult to estimate since it depends on many factors. Therefore the engine examples from the A320 manual are used to determine a correction. Using the nacelle dimensions given in the manual and the known engine dimensions, the average difference is determined and from that the calculated engine dimensions are converted to nacelle dimensions. Table 4.3 shows the final nacelle dimensions. For the analysis in this thesis a circular nacelle is assumed, rather than ovoid, to simplify the analysis and creating the geometric model.

Table 4.3: Nacelle dimensions for different bypass ratio's

BPR [-]	4	6	8	10	12	14
Length [m]	3.20	3.41	3.62	3.83	4.04	4.26
Diameter [m]	1.88	2.03	2.19	2.34	2.50	2.66

4.3.3. Engine weight

For a proper stability analysis, the aircraft c.g. needs to be known. Using the same weight for all engines would not be fair and therefore an engine weight estimation has been performed. The Class2Weight estimation methods from Torenbeek [49] or Raymer [38] mostly rely on engine thrust. Since the engine in the proposed scenario remains roughly the same (only the size changes), the statistical relation can not be used.

Using a simple regression for statistical data is also not a viable option. Although a clear link between thrust and weight is discernible, the effect of engine size or BPR on the mass is not clear. Figure 4.7[Left picture] shows the relation between the engine dry mass and thrust. A linear trend between the take off thrust and the engine mass is clear. If the mass is normalised with the max thrust and plot against the bypass ratio, see Figure 4.7[Right picture], some grouping occurs. But a clear relation is not possible to determine, another method must be used.

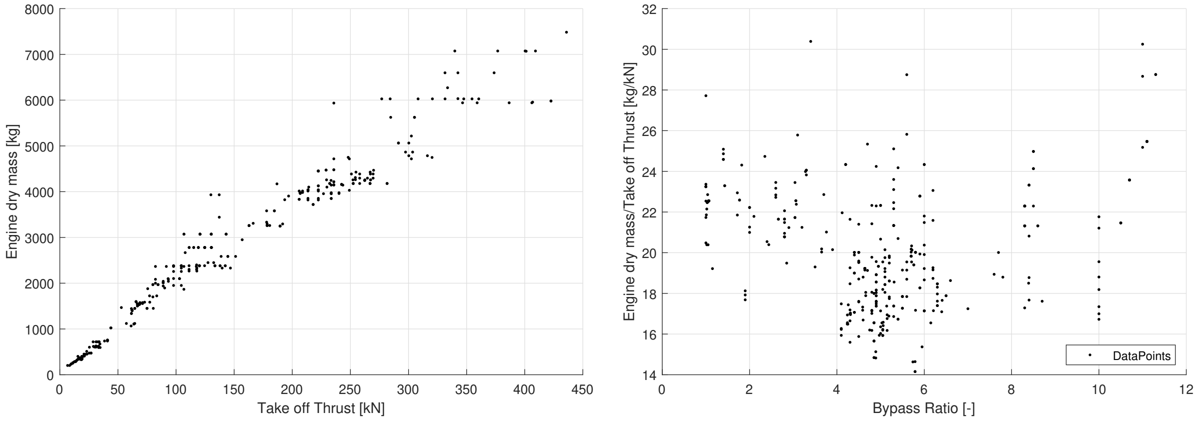

Figure 4.7: **[Left]** engine take-off thrust compared to engine drymass **[Right]** Bypass ratio compared to engine mass over max take-off thrust

Similarly to Torenbeek and Raymer, Mark Drela devised a method for engine weight estimation. The method is called TASOPT (Transport Aircraft System OPTimization) framework [10]. The Framework is used for complete aircraft design optimisation, similar to the Initiator tool. For the engine sizing rather than relying on statistical data, a simulation package (WATE [2]) was used. WATE calculates the weight and dimension of each major gas turbine engine component. It can be used to create an engine architecture that could achieve an engine thermodynamic cycle produced by a thermodynamic cycle code. Drela used the gas turbine design tool to create a data set for a range of bypass ratios, core mass flows, and overall pressure ratios. As a result, a power law relation between the engine weight and aforementioned parameters was found. The relation for the engine mass is shown in Equation 4.1. Two levels of technologies are considered which resulted in two different curves. Logically the weight of an advanced technology engine is lower than an engine built with the current technology level.

$$W_{direct,lbs} = a\left(\frac{\dot{m}_{core}}{100lbs/s}\right)^{b}\left(\frac{OPR}{40}\right)^{c} \tag{4.1}$$

with (current technology level, up to mid 2000s)

$$\begin{aligned} a &= 18.09BPR^2 + 476.9BPR + 701.3 \\ b &= (1.077x10^{-3})BPR^2 - (3.716x10^{-2})BPR + 1.190 \\ c &= (-1.058x10^{-2})BPR + 0.326 \end{aligned}$$

with (advanced technology level)

$$\begin{aligned} a &= 15.38BPR^2 + 401.1BPR + 631.5 \\ b &= (1.057x10^{-3})BPR^2 - (3.693x10^{-2})BPR + 1.171 \\ c &= (-1.022x10^{-2})BPR + 0.232 \end{aligned}$$

For this analysis the total engine mass flow is kept the same since thrust requirements are roughly similar for all engines. This leaves the BPR and the overall pressure ratio (OPR) to be varied. The BPR is the parameter to be varied, which means a value for the OPR needs to be found. When comparing the OPR with the BPR to find a relation, no clear dependency is found, see Figure 4.8. The OPR is more a function of the time period, see Figure 4.9. With the advancements in material science and better understanding of aerodynamics, higher pressure ratio's can be achieved. The spread of the overall pressure ratio for all datapoints is still quite large. Therefore it is opted to the use the values of the LEAP 1A and the CFM56 engine for a bypass ratio of 11 and 6 respectively and interpolate between them.

---

[2] obtained from : `https://software.nasa.gov/software/LEW-19687-1` [accessed on 10-06-2021]

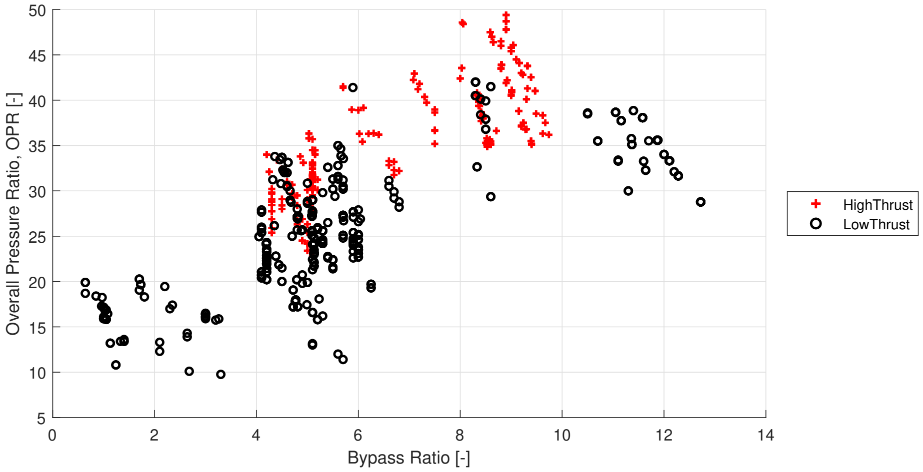

Figure 4.8: The datapoints from ICAO databank plotted for bypass ratio versus overall pressure ratio. Low thrust up to 150 kN, and high thrust 150+ kN.

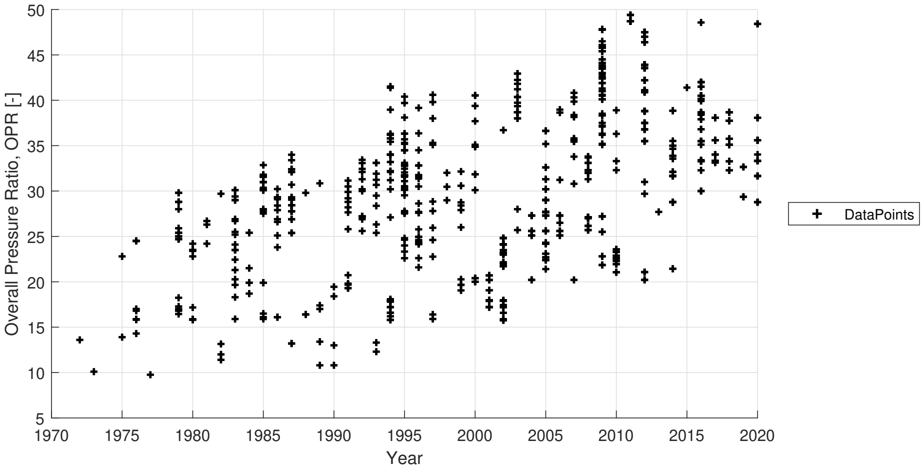

Figure 4.9: The datapoints from ICAO databank plotted for initial test date versus overall pressure ratio. Low thrust up to 150 kN, and high thrust 150+ kN.

As a check, the weight is also calculated in case all engines use the BPR 6 and the BPR 11 overall pressure ratio. The results are shown in Figure 4.10 together with the 'low' thrust reference engines from Table 4.2. The reference values for the lower bypass ratio are a little lower than expected. They lay below the line of the advanced engine technology, while these engines are from an older generation. The difference can be explained by the chosen mass flow which is closer to newer generation engines.

For a more accurate calculation of the engines weight, a third curve that averages the current and advanced technology curves should be used. Using such a curve the final engine weights become as shown in Table 4.5.

Table 4.4: The calculated engine weights for the different bypass ratio's, using a total mass flow of 900 lbs/s

BPR	4	6	8	10	12	14
OPR	28	30	34	38	42	44
$\dot{m}_{core}$ [lbs/s]	225	150	113	90	75	64
Dry engine mass [kg]	2624	2490	2579	2746	2952	3155

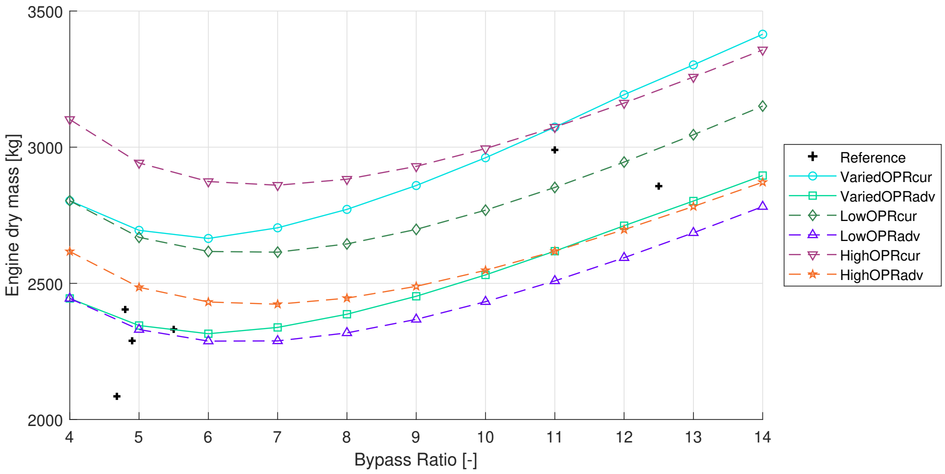

Figure 4.10: TASOPT calculated engine weights for difference levels of technology and OPR's

Besides the engine dry mass, the total engine weight including nacelle, systems and trapped liquids must be determined. These values are often estimated as percentages of the engine dry mass. Because the dry mass is already an assumption based on statistical data, it is assumed the liquids and other miscellaneous weights are included. Only the nacelle weight will be added. Torenbeek provides a simple calculation based on the take-off thrust. Because the take-off thrust is kept constant this will not work. The more complex method provided by Torenbeek calculates all nacelle components individually including sound proofing. However it would require more assumptions on the geometry. Raymer does provide a relation which only includes parameters that have already been established, see Equation 4.2.

$$W_n = 0.6724 K_{ng} N_{Lt}^{0.10} N_w^{0.294} N_z^{0.119} W_{ec}^{0.611} N_{en}^{0.984} S_n^{0.224} \tag{4.2}$$

with

- K_{ng} 1.017 for pylon-mounted nacelle
- N_{Lt} nacelle length, ft
- N_w nacelle width, ft
- N_z ultimate load factor; 2.5
- W_{ec} weight of engine and contents
- N_{en} number of engines, 2
- S_n nacelle wetted area, ft2

Using the values for the nacelle width and length from Table 4.3 and the weights from Table 4.4 the nacelle weight can be determined. The nacelle weights as well as the total engine weight used for the research are shown in Table 4.5

Table 4.5: The calculated engine weights for the different bypass ratio's, using a total mass flow of 900 lbs/s

BPR	4	6	8	10	12	14
Nacelle mass [kg]	489	504	546	599	658	719
Dry engine mass [kg]	2624	2490	2579	2746	2952	3155
Total engine mass [kg]	3113	2994	3125	3345	3610	3874

4.3.4. Engine location

In general, installing a larger engine on an existing airframe will require some modification to the engine location. For the engine retro-fit in this research, the airframe is kept the same. This means the wing, fuselage and landing gear are not changed. As a result, the engine location parameters should be constrained. Since a complete location optimisation is not possible, four simplified methods are proposed to investigate the effect of the engine location.

Firstly, an engine with fixed dimensions is moved in a 2D plane for the same spanwise location. The locations are shown in Figure 4.11. The effect of the engine location on the aerodynamic center can be isolated. The analysis is done for two engine sizes based on the CFM56 and LEAP. The engine is moved forward and back 10% of the engine length. Similarly, the engine is moved up and down 10% of the diameter. This does mean that the larger engine will be moved further in absolute values.

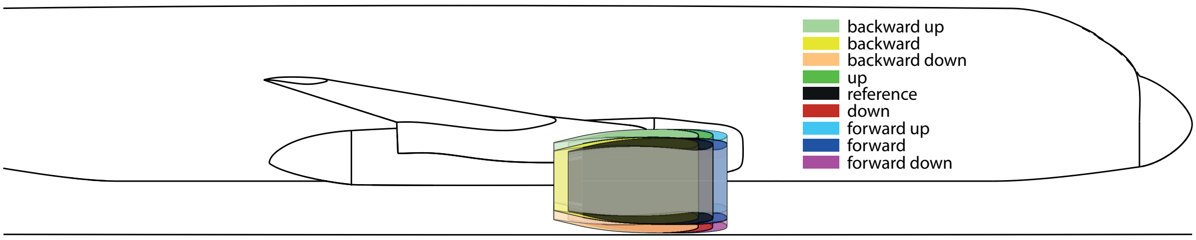

Figure 4.11: Different engine locations for the same nacelle size

Secondly, the engine location is kept constant, but the engine size is changed. The engine location is kept constant by keeping the geometrical center of the engine in the same place. As a result, the ground clearance and the distance between the engine and wing (gully) will reduce. The gully is the shortest distance between the nacelle and wing. Also the engine intake will effectively move forward. Similarly, the exhaust will move further aft. Figure 4.12 shows the locations schematically.

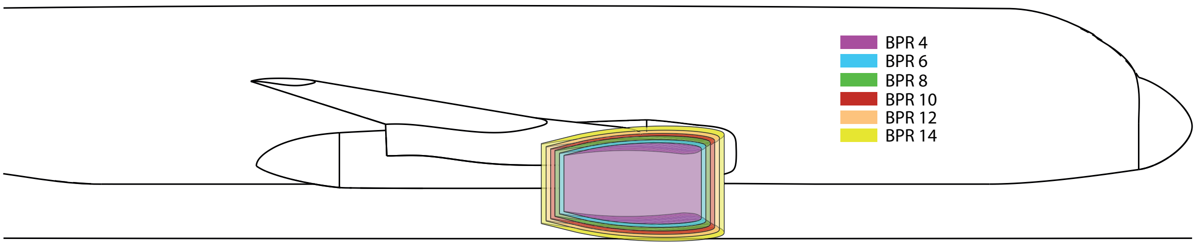

Figure 4.12: Engine locations for different bypass ratio's using a constant engine location, Case 1

By keeping the engine location constant, the effect of the engine size on the aerodynamic center can be evaluated. Next, to investigate the combined effect, two sets of constraints are defined for the engine location. For both sets of limitations, the gully distance is kept constant. The gully size and shape have a large influence on the aerodynamic interference around the nacelle and pylon. Sometimes resulting in a large increase in wave drag as discussed in chapter 2.

The first set of constraints is based on a constant spanwise engine location. The wing structure is reinforced at the location where the engine is mounted. By keeping the spanwise location the same, the required redesign of the wing may be neglected, provided that the engine location and weight don't increase too drastically. The steps of determining the engine location are as follows:

1. Keep gully distance the same.
2. Keep spanwise location the same.
3. Move larger engine down to a minimum ground clearance (Only explicitly defined for propeller aircraft. The LEAP1-A engine is used as a guidance).
4. Move engine forward and up.

Effectively, the larger engine will first move down and then forward to preserve the gully distance. The locations for the different engine sizes are shown in Figure 4.13. The horizontal line in the figure shows the lower limit which corresponds to a $0.47m$ ground clearance. The value is based on the smallest possible ground clearance for the A320. For the LEAP-1A engine together with the most forward location of the center of gravity, the ground clearance is $0.47m$ [46].

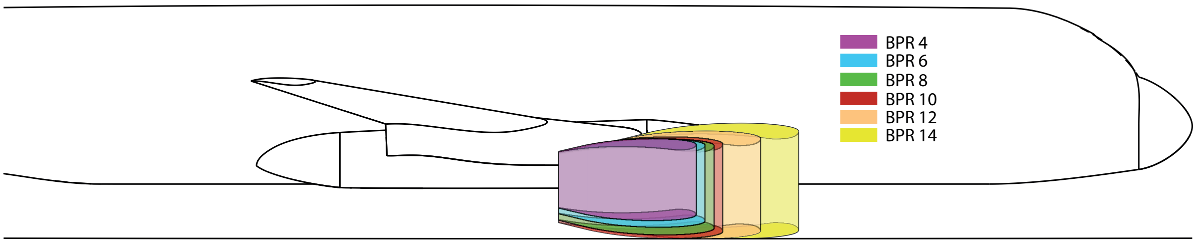

Figure 4.13: Engine locations for different bypass ratio's following the first set of constraints, Case 2

The effects of the new engine location for the aircraft are: a change in the overall center of gravity location due to the engine moving forward. A change in aerodynamic center due to the engine nacelle moving forward and as a consequence, moving the nacelle lift vector forward. The nacelle lift vector increases in size and will cause a larger pitching moment. Lastly the center of thrust moves down and will increase the destabilising effect of the thrust on the aircraft.

A second set of constraints is based around the aircraft center of gravity. The larger engine is heavier and will change the location of the center of gravity. The location of the center of gravity for the aircraft is known and the weight of the original engine (CFM56 or IAE V2500) is known too. With the new engine weights, the required moment arm can be calculated such that the moment remains the same. Similar to the first set of constraints, the gully distance must remain the same to prevent large wave drag effects. The gully distance can be preserved by moving the engine down and outboard. Moving the engine outboard will work for positive dihedral wings. The steps of determining the engine location are as follows:

1. Keep the aircraft centre of gravity the same by correcting for engine weight.
2. Keep gully distance the same.
3. Move larger engine down to minimum ground clearance (Only explicitly defined for propeller aircraft. The LEAP1-A engine is used as a guidance).
4. Move engine outboard and forward maintaining the gully distance.

The larger engine will move backward and down, and forward and down. When the ground clearance becomes a problem the engine will be moved outboard. Figure 4.14 shows the engine locations for the different engine sizes. The expected effects are similar to the first set of constraints, with the addition of the thrust vector moving further outboard. To comply with engine out requirement a larger vertical tail surface is needed.

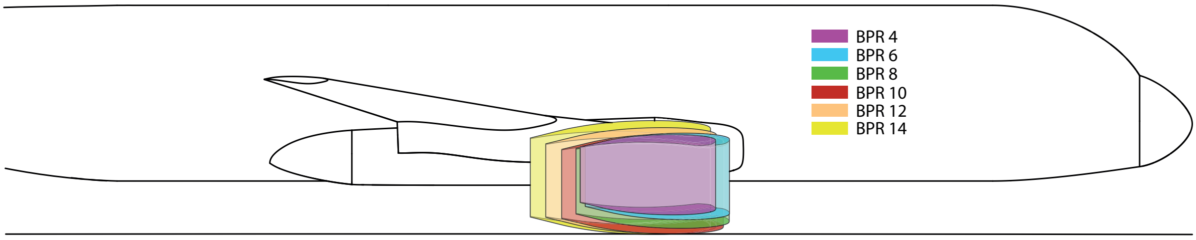

Figure 4.14: Engine locations for different bypass ratio's following the second set of constraints, Case 3

4.4. Aerodynamic Center evaluation

The effects of an engine and nacelle on the aircraft stability can be summarised in a change in aerodynamic center and pitching moment around the aerodynamic center. Normally in preliminary design methods, the aerodynamic center is estimated based on empirical relations. The data, on which the empirical relations are based, is old and likely invalid for modern high bypass ratio engines.

4.4.1. Theory

The pressure distribution around an airfoil can be simplified to a point with reaction forces. This point is called the center of pressure. For each pressure distribution, such a point can be defined and the location will change with the varying pressure distribution. For more consistent comparing the aerodynamic center is defined. Two major characteristics for the aerodynamic center will be used:

1. The location doesn't vary with the angle of attack
2. The pitching moment around the aerodynamic center is constant with the angle of attack

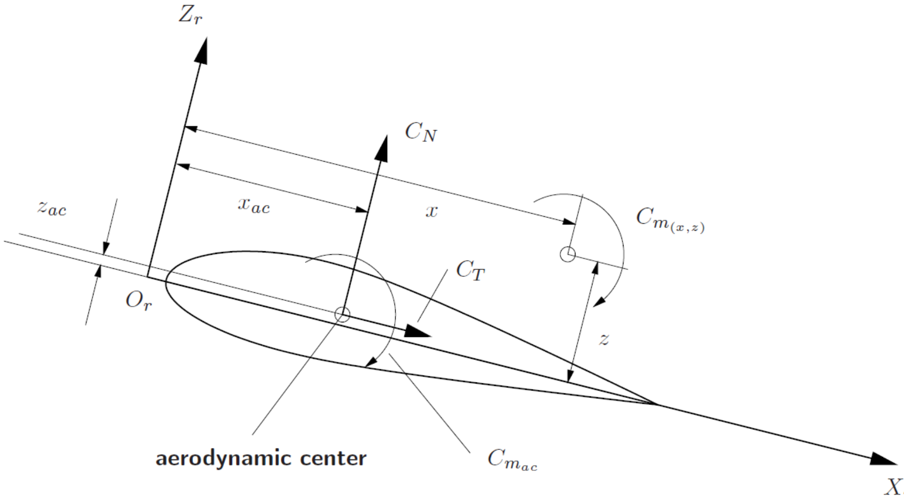

Figure 4.15: The aerodynamic forces and moment, using the aerodynamic center as the moment reference point, taken from [29]

Figure 4.15 shows a free-body diagram for an airfoil with all acting forces and moments. The moment coefficient C_M can be defined for any arbitrary location (x, z). Together with the location of the aerodynamic center and the magnitude of the pitching moment around the aerodynamic center, Equation 4.3 can be defined.

$$C_M(x,z) = C_{M_{ac}} + C_N \frac{x - x_{ac}}{\bar{c}} - C_T \frac{z - z_{ac}}{\bar{c}} \tag{4.3}$$

It is possible to use the second condition and Equation 4.3 to determine the aerodynamic center using FlightStream results. From the equation it is clear that for any arbitrary point (x, z) the $C_{M_{ac}}$ remains the same. Any moment curve will intersect at the $C_{M_{ac}}$. In other words, finding the intersection between two moment curves will yield the pitching moment around the aerodynamic center.

For lower angles of attack, the moment coefficient shows a linear behaviour which means the pitching moment curve can be approximated with a linear solution. For determining the linear moment curve, two solutions at different angles of attack are needed.

FlightStream computes its results around a user defined reference frame. In order to create two moment curves, two reference frames need to be defined at different longitudinal locations.

Before the solutions can be used, one assumption is made regarding Equation 4.3. When the user defined reference frames are chosen close to the expected aerodynamic center height z_{ac}, its contribution can be neglected. The wing is the main contributor to the aerodynamic center and a good start for z_{ac} is on the mean aerodynamic chord (MAC). With changing flight conditions, the aerodynamic center mainly moves forward and back. Additionally, the tangential coefficient C_T is almost 2 orders of magnitude smaller. Therefore it is assumed the effects of C_T can be neglected.

Using the two solutions for two reference frames, two moment curves can be drawn. Using the data points the respective linear equations can be found. Next the intersection (which is the $C_{M_{ac}}$) can be calculated. Using Equation 4.4 the unknown $x - x_{ac}$ can be calculated. The calculated variable gives the relative distance between the aerodynamic center and the user defined reference frame.

$$C_M(x) = C_{M_{ac}} + C_N \frac{x - x_{ac}}{\bar{c}} \tag{4.4}$$

It is essential that the reference frame used for computing the $C_{M_{ac}}$ is used when defining $x - x_{ac}$. With the location of the reference frame, either the absolute location or the relative location with respect to the leading edge of the MAC can be calculated.

4.4.2. Validation

To validate whether it is possible to use this method with FlightStream, a NACA airfoil is tested. In the same way the NASA CRM is checked. The validation is also performed to check whether the aforementioned assumption holds.

NACA0005

According to thin airfoil theory for incompressible, invicid flow the aerodynamic center of the airfoil lies at ${}^{1}/_{4}\bar{c}$ [2]. For low angles of attack and low Mach numbers, or when no separation occurs, the actual aerodynamic center will lie close to the quarter chord point.

In this validation the simulation is run for compressible, viscous flows at a Reynolds number of 5 million. The Mach number is 0.2 and the NACA 0005 airfoil has a small thickness, 5%. This means a slight deviation in aerodynamic center can be expected. The 2D geometry used for the NACA 0005 is shown in Figure 4.16. The reference frames are shown, as well as the quarter chord location.

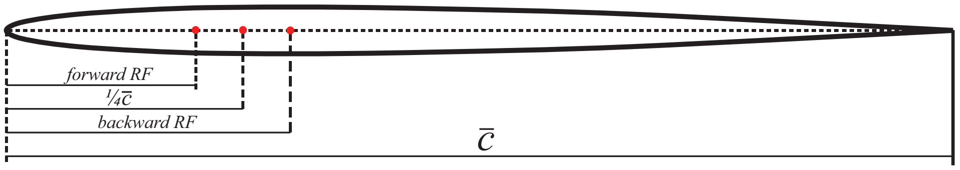

Figure 4.16: Schematic drawing of NACA 0005 profile with the chosen Reference Frames (RF)

In order to emulate a 2D wing solution, the span was chosen an order of magnitude larger compared to the chord. The number of spanwise elements is 1. The number of chordwise elements is similar to that of the CRM validation in subsection 3.2.4. Both a leading and trailing edge refinement is utilised. Figure 4.17 shows the normal and tangential forces for a range of angles of attack. For larger angles of attack the normal force compared to the tangential force is large. Meaning that the effect of the tangential force on the moment will be small.

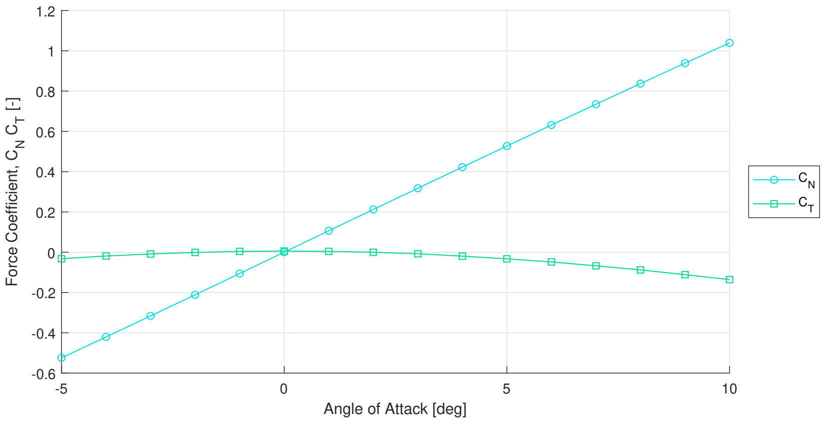

Figure 4.17: The normal force C_N and tangential force C_T for the NACA 0005 profile as calculated by FlightStream

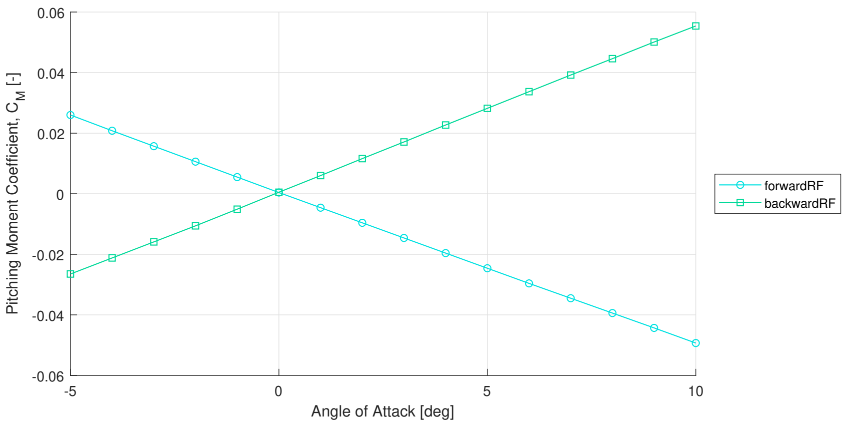

Figure 4.18: The pitching moment coefficient C_M for the NACA 0005 profile calculated at two reference locations

Figure 4.18 shows that for the chosen angle of attack range a linear estimation for the moment curve is acceptable. By using the data points at $-5°$& $10°$angle of attack, the two equations for the curves can be calculated. It is already clear from the figure that the intersection of the moment curves lies roughly at zero angle of attack. The pitching moment at that angle of attack is also roughly zero. The equations for the moment curves are:

Forward Reference Frame *Backward Reference Frame*

$$0.00546\alpha + 0.0008 \qquad -0.00502\alpha + 0.0009$$

By calculating the intersection between the two curves, the angle of attack at intersection is $0.01°$. The respective moment coefficient, $C_{M_{ac}}$ is 0.00085. The location of the aerodynamic center can be calculated using Equation 4.4 and the data from one of the moment curves. Further data is given in section B.1. For the NACA 0005 the location of the aerodynamic center is calculated at $0.248\bar{c}$, roughly $^1/_4\bar{c}$. The difference is -0.8%. In Figure 4.19 the moment curve around the aerodynamic center is shown. From the result data in section B.1 it can be seen that the moment stays constant at the C_{Mac} value that was previously calculated.

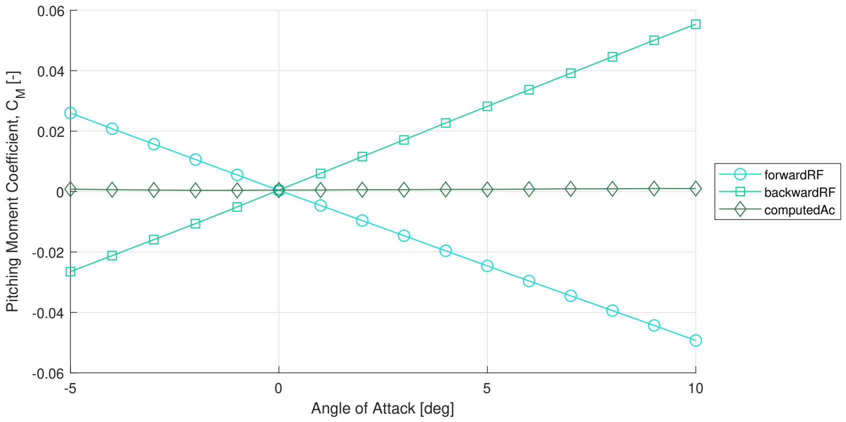

Figure 4.19: The pitching moment coefficient C_M for the NACA 0005 profile calculated at two reference locations and the aerodynamic center

To check the effect of the vertical distance z and the tangential force C_T the reference frame is moved up and down with respect to the calculated aerodynamic center. The moment due to the normal force is not considered in this case. The reference frames are a similar distance away from the aerodynamic center as the horizontally chosen reference frames. It is roughly 5% of the chord. From Figure 4.20 it is clear that magnitude of the moment is much smaller, especially for the larger angles of attack. Another way of checking this assumption is by evaluating an entire aircraft compared to just the airfoil.

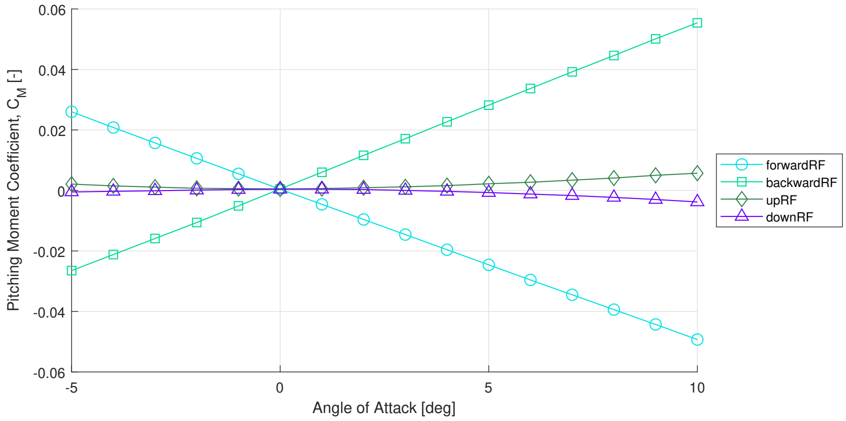

Figure 4.20: The pitching moment coefficient C_M for the NACA 0005 profile calculated at four reference locations

NASA Common Research Model

Although the Common Research Model (CRM) does not have a known location of the aerodynamic center, the calculation of the location is still done and used to check the method. In the calculation a nacelle and pylon geometry are also added.

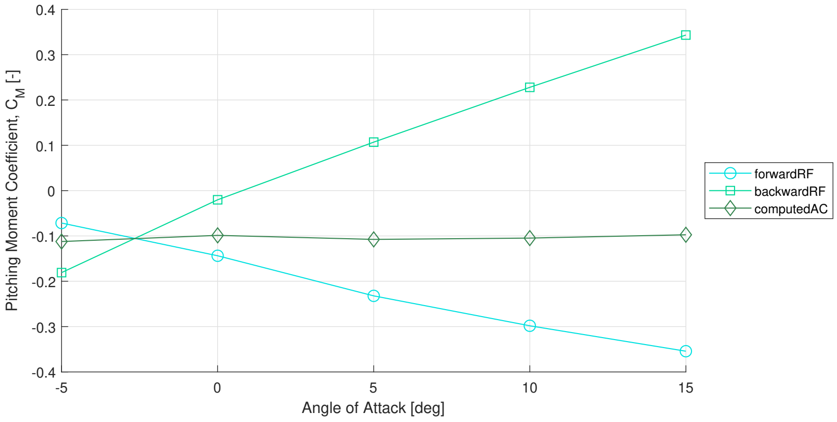

Figure 4.21: Moment curves for the CRM wing body and the moment curve at the calculated aerodynamic center

In Figure 4.21 the moment curves corresponding to the CRM Wing Body (WB) are plotted. For the angle of attack range ($-5°$- $15°$) the curves show a small non-linearity. This non-linearity becomes more apparent when adding the nacelle and pylon. Figure 4.22 shows the moment curves for the Wing Body, Nacelle and Pylon (WBNP). From $5°$onward a non-linearity is visible in the forward RF curve. The real change in slope however happens at $10°$. Through the points $-5°$to $10°$a mostly linear trend can be seen. For the calculated location of the aerodynamic center the curve has a zero slope.

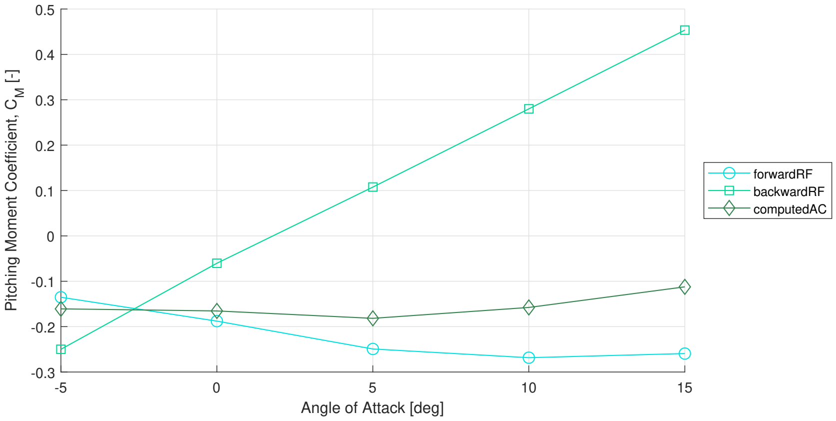

Figure 4.22: Moment curves for CRM wing body+nacelle+pylon and the moment curve at the calculated aerodynamic center

To check the effect of the pylon on the location of the aerodynamic center, the same analysis is done without the pylon. The results are shown in Figure 4.23

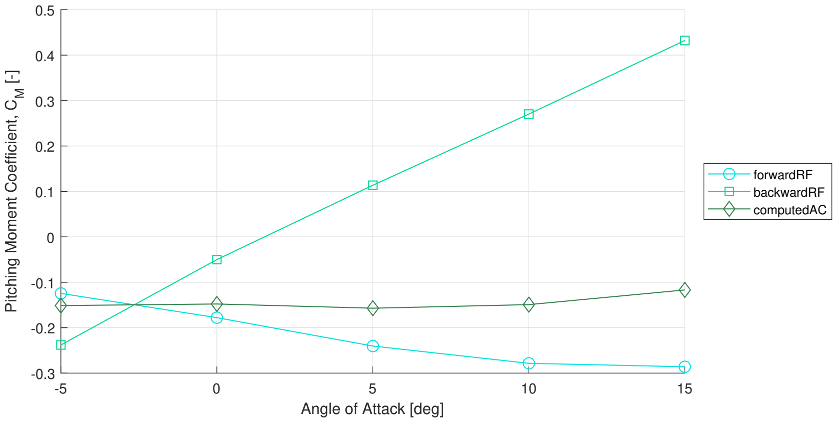

Figure 4.23: Moment curves for CRM wing body+nacelle and the moment curve at the calculated aerodynamic center

The exact values for the CRM aerodynamic center locations are shown in Table 4.6. Adding the nacelle to the CRM model resulted in a movement of the aerodynamic center forward by roughly 1%. By adding the pylon to the aircraft the aerodynamic center moved 0.5% further forward. In this case for the CRM the effect of adding the engine nacelle is quite small. Secondly the effects of the pylon cannot be neglected when considering the WBN and WBNP case. The difference in aerodynamic center is almost 50% between the two. However compared to the whole aircraft, the effect of the pylon is minor.

Table 4.6: Aerodynamic center locations for the CRM simulation case

	x_{ac} from nose	Delta	
	[m]	[m]	[-]
WB	0.890	0.000	0.00%
WBN	0.879	-0.0106	-1.19%
WBNP	0.875	-0.0143	-1.61%

4.5. Stability analysis

During the preliminary design phase, the horizontal and vertical tail surfaces are sized by using stability and control criteria. In this research four criteria will be investigated. These include: stick free, and stick fixed stability for the aft c.g. location. For the forward c.g. location, the aircraft low speed controllability and take-off rotation are the criteria for the tail design. For the stick-fixed criteria often a stability margin (S.M.) is included. No governing requirements are defined, but generally a 5% margin on $x_{ac}/\bar{c}$ is used.

In Figure 4.24 the 4 different criteria used in preliminary tail design are shown. The green area shows the possible design space. From the preliminary weight estimation the forward and aft c.g. location can be estimated. The c.g. locations give a required travel which will correspond to a required tail surface. Important for the analysis is an accurate weight and c.g. estimation. In this research the airframe is kept mostly the same, only the engine is changed. This makes the c.g. estimation easier because a c.g. can be chosen, and would only have to be corrected for the new engine weight and location. This nullifies the need to perform a full weight and balance estimation.

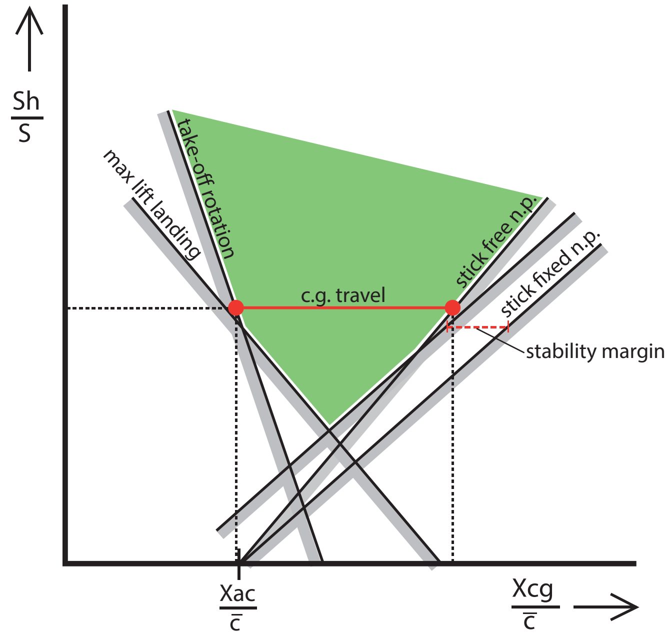

Figure 4.24: Example of a stability plot used for the preliminary tail design

4.5.1. Center of gravity estimation

Simply choosing a c.g. location for the aircraft would not be rectifiable. Either a known value or some sort of estimation should be used. Figure 4.25 shows the center of gravity limits for an A320-232 aircraft. It shows the most forward and backward c.g. locations with respect to the MAC. Using this figure, a substantiated estimation for the c.g location can be made. However, it should be noted that the geometry used in the FlightStream simulations is based on an approximation. For the criteria of the stability analysis as shown in Figure 4.24, further assumptions will be made. Nevertheless, basing the parameters on real values will help in drawing conclusions.

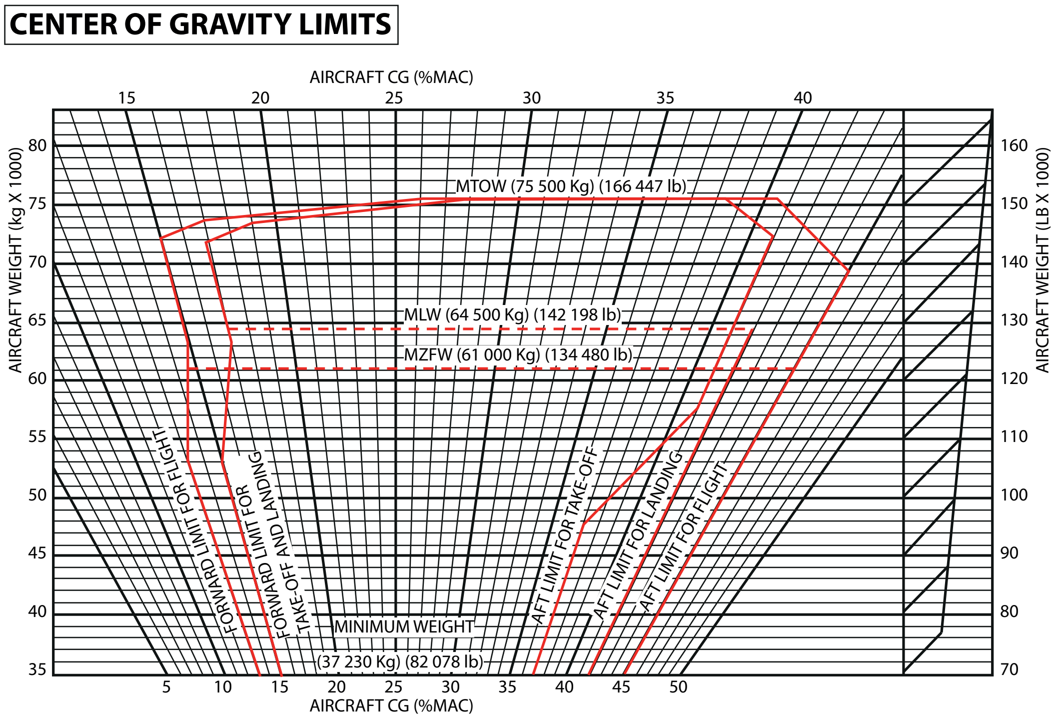

— CG limits are given in percentage of the reference chord length aft of the leading edge.

— The reference chord length is 4.193 m (13.76 ft). It is 16.31 m (53.51 ft) aft of the aircraft nose.

— The CG must always be within these limits, regardless of fuel load.

Figure 4.25: Center of gravity limits plot for the A320-232 taken from the weight and balance manual [45]

The A320-232 is mostly equipped with the IAE Model V2527-A5 engine. By using the known weight and location of the engine on the aircraft, the c.g. location of the basic airframe can be determined. The IAE engine weighs 2404 kg, see Table 4.2. From the A320 service manual [46] the location of the engine is taken. The leading edge of the nacelle lies 11.12m from the nose of aircraft. The nacelle and engine are 5.25m and 3.10m long respectively, the engine fan face lies 1.41m from the nacelle inlet. The actual c.g. of the engine is located at approximately one-third of the engine length, or 13.56m from the nose of the aircraft. Most of the weight will be located at the front of the engine (at the fan and compressor). Similar numbers are found in an old (1988) A320 weight and balance manual [45], see Figure C.1. The c.g. location of the engine lies roughly 1m behind the fan face for an engine with 3m length.

Regardless of the correction for the engine weight, the values from Figure 4.25 can still be used. The c.g. range will be very similar and can still be used to adjust for tail size using a graph as shown in Figure 4.24

4.5.2. Stick-fixed static stability

The first criteria that will be discussed is the stick-fixed stability. The stick-fixed criterion checks the required tail surface area to provide sufficient force to be neutrally stable in cruise conditions. Torenbeek [49] provides a method to determine the stability plot for a simplified aircraft using the free body diagram shown in Figure 4.26. Torenbeek does not regard the engine in the analysis, whereas for this research, it is required to take the engine into account. In red, the engine thrust is added to the free body diagram. The moment, as a result from the thrust, will be taken into account in the analysis. If the horizontal tail is located far above the c.g. (T-tail configuration) the drag produced by the tail can generate a moment around the c.g. as well. The magnitude of drag compared to the lift forces is small, and the arm will be relatively small compared to the tail force (L_h) arm. Therefore the drag of the horizontal tail is not considered.

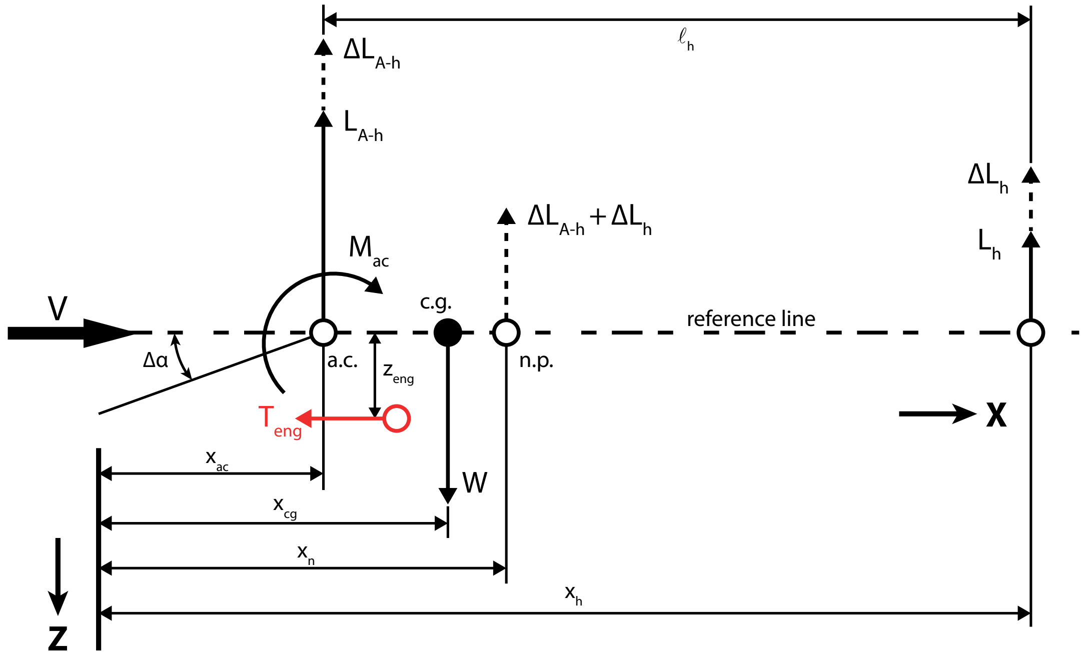

Figure 4.26: Simplified free body diagram for an aircraft in cruise configuration

Using the free body diagram a non-dimensional moment equilibrium can be calculated. Equation 4.5 shows the moment equilibrium as is defined by Torenbeek. The effect of the engine is included in red. The effect of the nacelle lift will be included in the lift generated by the wing-fuselage, or L_{A-h} in the free body diagram.

$$C_M = C_{M_{ac}} + C_L \frac{x_{cg} - x_{ac}}{\bar{c}} - C_{L_h} \frac{S_h l_h}{S\bar{c}} \left(\frac{V_h}{V}\right)^2 + C_{Th} \frac{z_{eng}}{\bar{c}} \tag{4.5}$$

$$\frac{x_n - x_{cg}}{\bar{c}} = -\frac{dC_M/d\alpha}{dC_L/d\alpha} \tag{4.6}$$

In Torenbeek the requirement for stick-fixed stability can be found (Equation 4.6). Using this equation and Equation 4.5 a relation between $x_{cg}/\bar{c}$ and the required S_h/S can be derived, as shown in Equation 4.7.

$$\frac{x_{cg}}{\bar{c}} = \frac{x_{ac}}{\bar{c}} + \frac{C_{L_{h\alpha}}}{C_{L_\alpha}} \left(1 - \frac{d\epsilon}{d\alpha}\right) \frac{S_h l_h}{S\bar{c}} \left(\frac{V_h}{V}\right)^2 - \frac{C_{Th_\alpha}}{C_{L_\alpha}} \frac{z_{eng}}{\bar{c}} - S.M. \tag{4.7}$$

with

- $\frac{x_{cg}}{\bar{c}}$ is the c.g. location as a percentage of the MAC.
- $\frac{x_{ac}}{\bar{c}}$ is the a.c. location as a percentage of the MAC (obtained from FlightStream).
- $C_{L_{h\alpha}}$ is the lift slope coefficient for the horizontal tail (obtained from a FlightStream analysis for A320 reference tail).
- C_{L_α} is the lift slope coefficient for the aircraft without tail (obtained from FlightStream).
- $\left(1 - \frac{d\epsilon}{d\alpha}\right)$ the downwash coefficient (obtained from FlightStream)
- $\frac{S_h}{S}$ is the ratio of the tail surface area over wing surface area.
- l_h is the horizontal distance between the wing quarterchord point and tail quarterchord point, see Figure 4.26 for the definition.
- $\frac{V_h}{V}$ is the velocity ratio of the tail velocity over the wing (obtained from FlightStream)

- C_{Th_α} is the thrust coefficient with respect to the angle of attack.
- z_{eng} is the perpendicular distance between the thrust vector and the c.g.
- $S.M.$ is the stability margin, usually set at 5%.

The effect of the thrust with respect to the angle of attack is negligible. The effect of the engine in this criterion is included in the lift coefficient for the aircraft without the tail (A-h). The downwash $(1 - d\epsilon/d\alpha)$ and the velocity ratio $(V_h/V)^2$ are determined from the FlightStream solution. FlightStream can calculate off-body streamlines. In the geometry used for the simulation, the tail is not present. To compensate for this non-presence, a set of streamlines is placed along the leading edge of a fictional horizontal tail. The location of the fictional horizontal tail is based on the A320 geometry. The streamlines are generated upstream. The coordinates for the streamlines are used to determine the downwash at the horizontal tail. The local velocity is used to calculate the velocity ratio. Finally, the results are averaged for all streamlines to obtain the final values used in the analysis.

4.5.3. Stick-free static stability

The stick-free stability can be determined using a similar method to that of the stick-fixed. For the aircraft without tail, nothing will change. However, the tail performance is now dependent on the elevator position. Equation 4.8 is similar to Equation 4.7 as derived above. The parameters with a prime (’) are modified. When looking at the parameter $C'_{L_{h_\alpha}}$, shown in Equation 4.10, the effect of the elevator is visible.

$$\frac{x'_{cg}}{\bar{c}} = \frac{x_{ac}}{\bar{c}} + \frac{C'_{L_{h_\alpha}}}{C'_{L_\alpha}} \left(1 - \frac{d\epsilon}{d\alpha}\right) \frac{S_h l_h}{S\bar{c}} \left(\frac{V_h}{V}\right)^2 \tag{4.8}$$

$$C'_{L_\alpha} = \left(C_{L_\alpha}\right)_{A-h} + C'_{L_{h_\alpha}} \frac{S_h}{S} \left(1 - \frac{d\epsilon}{d\alpha}\right) \tag{4.9}$$

$$C'_{L_{h_\alpha}} = C_{L_{h_\alpha}} - C_{L_{h_\delta}} \frac{C_{h_\alpha}}{C_{h_\delta}} \tag{4.10}$$

with

- $\frac{x'_{cg}}{\bar{c}}$ is the c.g. location as a percentage of the MAC with correction for a free elevator.
- $C'_{L_{h_\alpha}}$ is the lift slope coefficient of the horizontal tail with a free elevator.
- C'_{L_α} is the corrected lift curve slope for a free elevator.
- $C_{L_{h_\delta}}$ is the lift curve slope for the horizontal tail with respect to the elevator. Calculated using $C_{L_{h_\alpha}} \sqrt{S_{elevator}/S_h}$ where $S_{elevator}/S_h$ is based on the value (0.24) for the A320.
- C_{h_δ} is the hinge moment with respect to the elevator deflection. From Torenbeek follows a conservative value of -0.1.
- C_{h_α} is the hinge moment with respect to the angle of attack. Torenbeek suggests using $-{}^{1}/{}_{3}C_{h_d}$ as a guideline.

4.5.4. Max lift at landing controllability

The first forward c.g. criterion is the low speed, or landing controllability. The goal of the criterion is to provide sufficient tail force at low speed to maintain aircraft control. The landing conditions means the aircraft must be in landing configuration, with flaps deployed. Figure 4.27 shows a free body diagram for the aircraft during the landing phase.

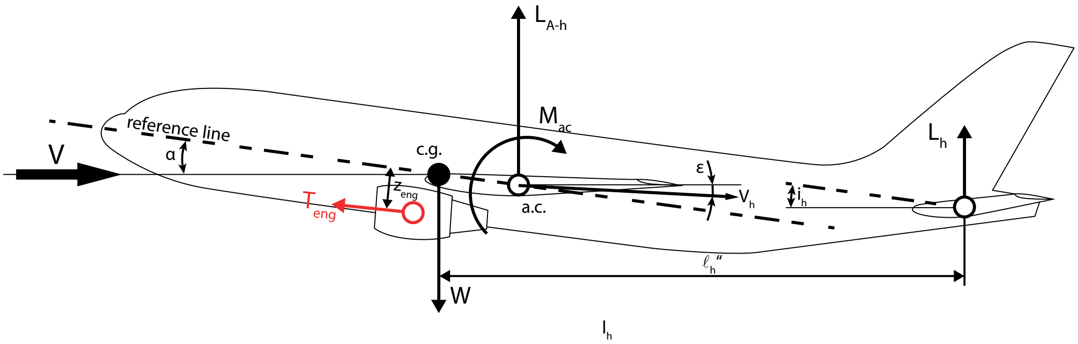

Figure 4.27: Simplified free body diagram for an aircraft during landing

The following equation is used:

$$\frac{x_{cg}}{\bar{c}} = \frac{x_{ac}}{\bar{c}} - \frac{C_{Th}}{C_{L_{A-h}}}\frac{z_{eng}}{\bar{c}} - \frac{C_{M_{ac}}}{C_{L_{A-h}}} + \frac{C_{L_h}}{C_{L_{A-h}}}\frac{S_h l_h"}{S\bar{c}}\left(\frac{V_h}{V}\right)^2 \tag{4.11}$$

with

- $\frac{x_{cg}}{\bar{c}}$ is the c.g. location as a percentage of the MAC.
- $\frac{x_{ac}}{\bar{c}}$ is the a.c. location as a percentage of the MAC (obtained from FlightStream).
- $C_{M_{ac}}$ is the pitching moment around the a.c. (obtained from FlightStream).
- C_{L_h} is the maximum lift coefficient for the horizontal tail (Assumption based on Torenbeek).
- $C_{L_{A-h}}$ is the maximum lift coefficient for the whole aircraft minus the tail (Assumption based on Torenbeek)
- $\frac{S_h}{S}$ is the ratio of the tail surface area over wing surface area
- $l_h"$ is the horizontal distance between the wing quarterchord point and tail quarterchord point, see Figure 4.27 for the definition.
- $\frac{V_h}{V}$ is the velocity ratio of the tail velocity over the wing (obtained from FlightStream).
- C_{Th} is the thrust coefficient, $T = C_{Th} 1/2 \rho V^2 S_{ref}$
- z_{eng} is the distance between the thrust vector and the c.g.

4.5.5. Take-off rotation controllability

The second low speed criterion is the take-off rotation criterion. The horizontal tail must be able to provide enough force to produce a specified angular rotation.

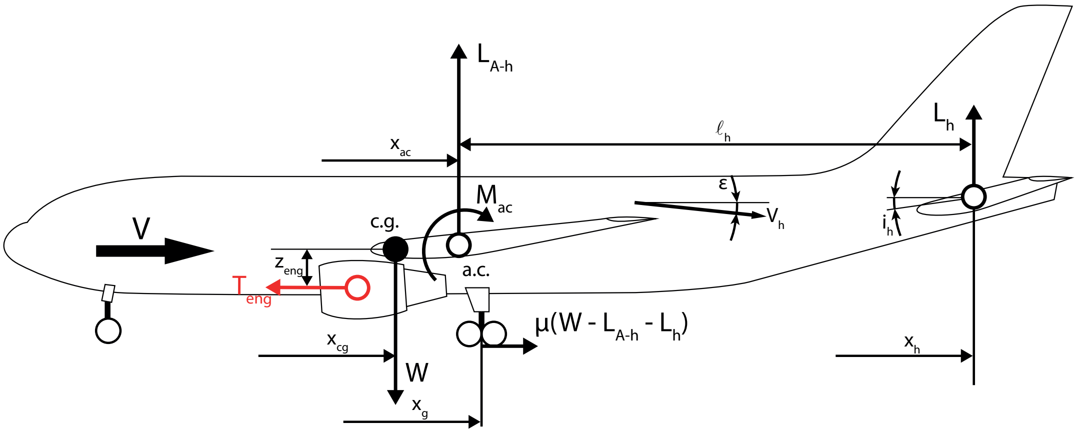

Figure 4.28: Simplified free body diagram for an aircraft during take-off rotation

$$\frac{x_{cg}}{\bar{c}} = \left[\left(\frac{S_h}{S}\frac{l_h}{\bar{c}} - \frac{C_{L_R}}{C_{L_h}}\left(\frac{x_g}{\bar{c}} - \frac{x_{ac}}{\bar{c}}\right)\right) * \frac{\eta_h \eta_q C_{L_h}}{C_{L_{max}}} - \frac{C_{M_{ac}}}{C_{L_{max}}}\right] \frac{V_R}{V_{S1}}^2 + \frac{x_g - 2 z_{eng} T/W}{\bar{c}} \tag{4.12}$$

where

$$\eta_h = \frac{x_h - x_g}{l_h}\left(\frac{V_h}{V_R}\right)^2 \tag{4.13}$$

$$\eta_q = 1 + \frac{C_{L_{h\alpha}}}{C_{L_h}} \frac{\dot{\theta}_R (x_h - x_g)}{V_R} \tag{4.14}$$

with

- $\frac{x_{cg}}{\bar{c}}$ is the c.g. location as a percentage of the MAC.
- $\frac{x_{ac}}{\bar{c}}$ is the a.c. location as a percentage of the MAC (obtained from FlightStream).
- C_{L_R} is the lift coefficient at rotation. Based on the MTOM and required lift to take-off at V_R.
- C_{L_h} is the lift coefficient of the horizontal tail.
- $\frac{V_h}{V_R}$ the velocity ratio of the horizontal tail over the main wing during rotation.
- $\frac{V_R}{V_{S1}}$ is the velocity ratio between the velocity at take-off rotation and decision speed V1 (V1 for the A320 is 149 kts).
- T/W is the thrust over the aircraft weight ratio.
- $\dot{\theta}$ is the pitchrate during the rotation phase. Torenbeek suggests a value of $4\,\mathrm{deg}/s$ for medium range transport aircraft.
- x_g is the location of the main gear with respect to a reference location.
- x_h is the location of the horizontal tail with respect to a reference location.
- η_h is the tailplane effectiveness factor.
- η_q is a simplification factor.

For the landing and take-off cases the aircraft should be in the respective configuration with flaps deployed. No geometry for the flaps is available. Determining the maximum lift coefficients and the above mentioned FlightStream parameters is not possible. Therefore it is opted to use the clean configuration and evaluate it at the landing and take-off conditions. The pitching moment is then corrected for the flaps using the information in Appendix E of Torenbeek [49].

4.6. Drag analysis

Finally, to go back to the original question of finding the installation penalty, a small drag assessment is performed. Using the newly obtained geometry for the nacelle and tail, the change in the drag coefficient is assessed.

In subsection 3.2.4 the capability of FlightStream to capture the aircraft performance has been investigated. Although it is difficult to capture quantitative results, the trends can be captured. Correct modelling and meshing of the pylon in FlightStream is a difficult task. A small test is done for the CRM to check the influence of the pylon on the overall drag coefficient. Figure 4.29 shows the pressure coefficient contours for the CRM WB and WBNP configuration.

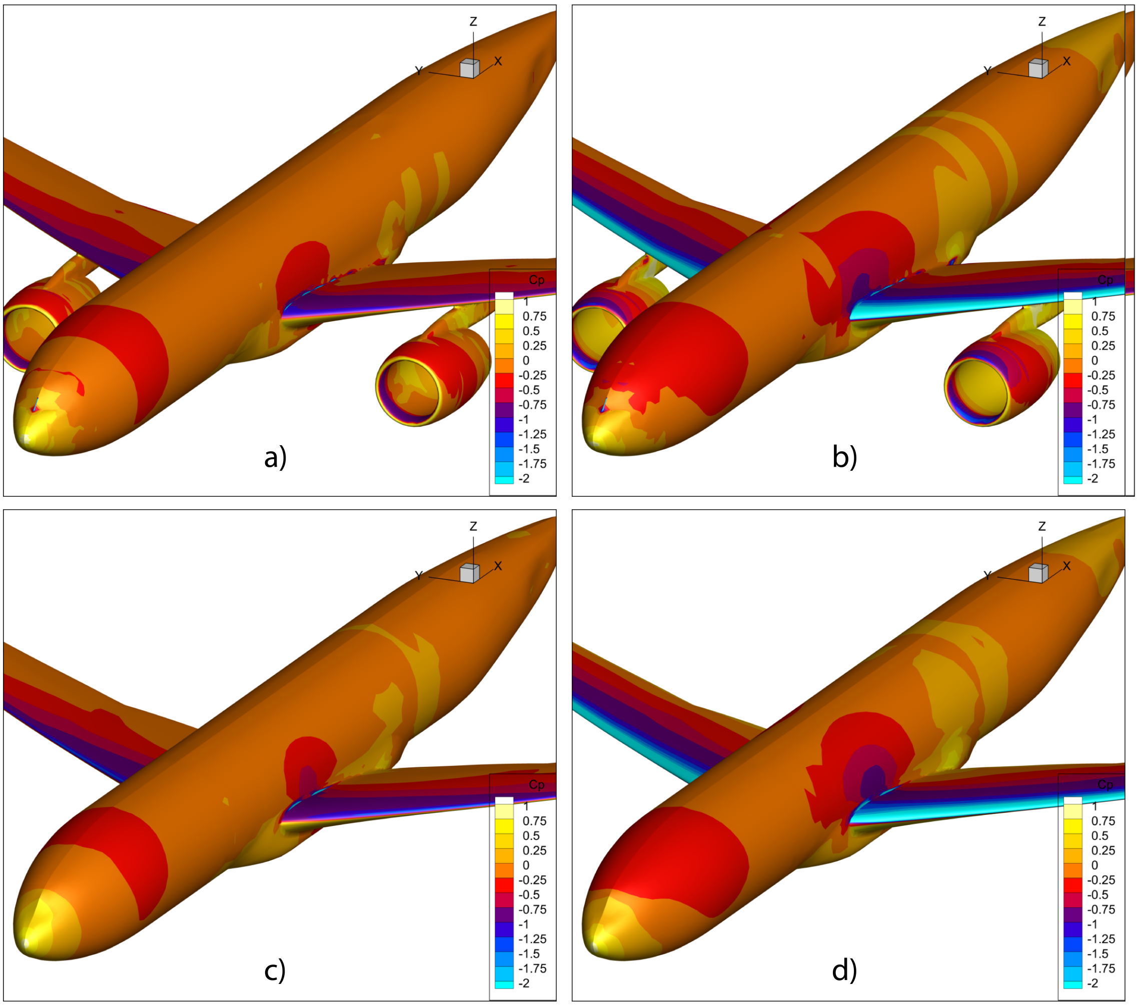

Figure 4.29: Contour plot of the pressure coefficient (C_p) for the CRM WBNP and WB configuration. Isometric view. Angle of attack for a) and c) are 2.8° ($C_L =$ 0.5) and for b) and d) 10°.

Looking at the first plot a) in Figure 4.29, a difference pressure between the inside and outside of the pylon can be seen. On the inboard side of the pylon the pressure is lower compared to the outboard side. As a result, the pressure distribution on the main wing also changes. This is better visible in Figure 4.30 a) & b). The pylon causes contour lines to occur on the bottom side, these are not present when there is no nacelle and pylon.

The reduction in the lift coefficient is also visible through the contour lines. For Figure 4.29 a) & c), the low pressure suction peak (indicated with blue) is smaller when the nacelle and pylon are included. This even extends to the fuselage. In chapter 2 it was already stated that it is possible for 60% of the wing to experience a reduced lift coefficient. With the FlightStream analysis for the CRM case, it was not possible to quantify this coefficient.

The contour plots also show some small anomalies. These occur especially near the surface connections, such as the wing-fuselage connection. The effective magnitude of these elements is small. The effect on the total aircraft performance is negligible. However, it does show an important point when using FlightStream. Either minimise the number of surface connections or apply local mesh refinement. Local mesh refinements are not straight forward to make in FlightStream. If the mesh of the entire model is refined, the solver time will be too long.

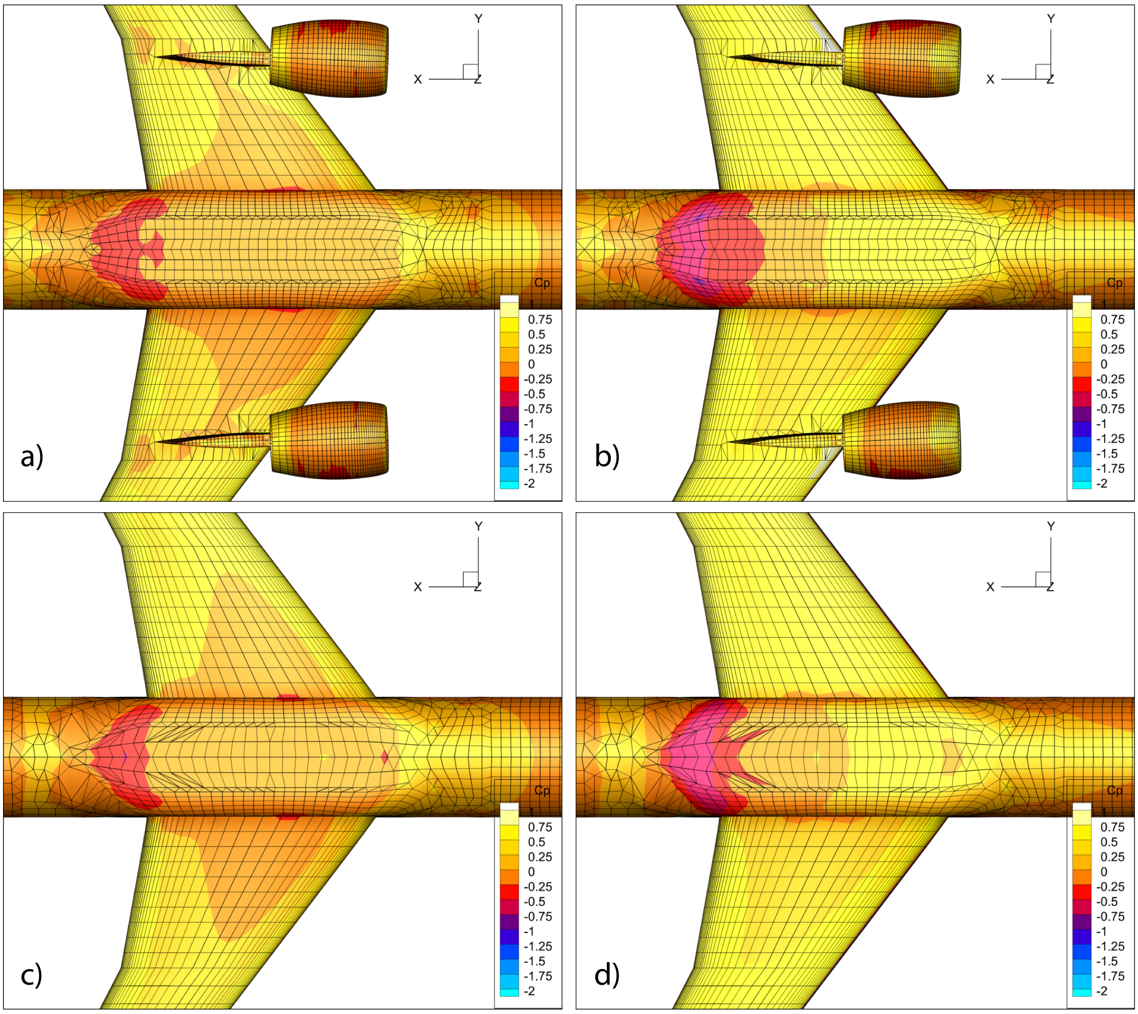

Figure 4.30: Contour plot of the pressure coefficient (C_p) for the CRM WBNP and WB configuration (Bottom view). Angle of attack for a) and c) is 2.8° ($C_L =$ 0.5) and for b) and d) 10°.

Figure 4.31 shows the drag polar for the CRM WBN compared to the WBNP. The difference in drag is very small when considering the entire aircraft.

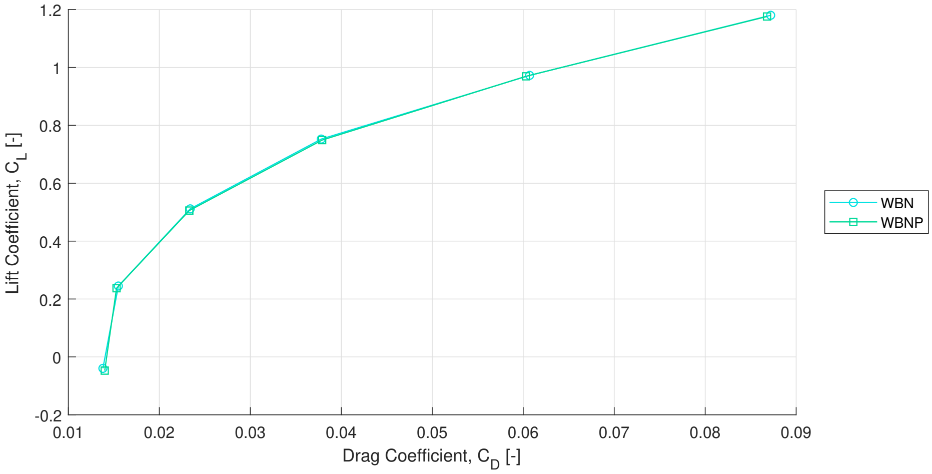

Figure 4.31: Drag polar for the CRM WBN and WBNP at Mach 0.7, Re 5 million, for the scaled model.

Figure 4.32 shows a zoomed-in part of the drag polar. It shows a slight increase in drag when the pylon is included.

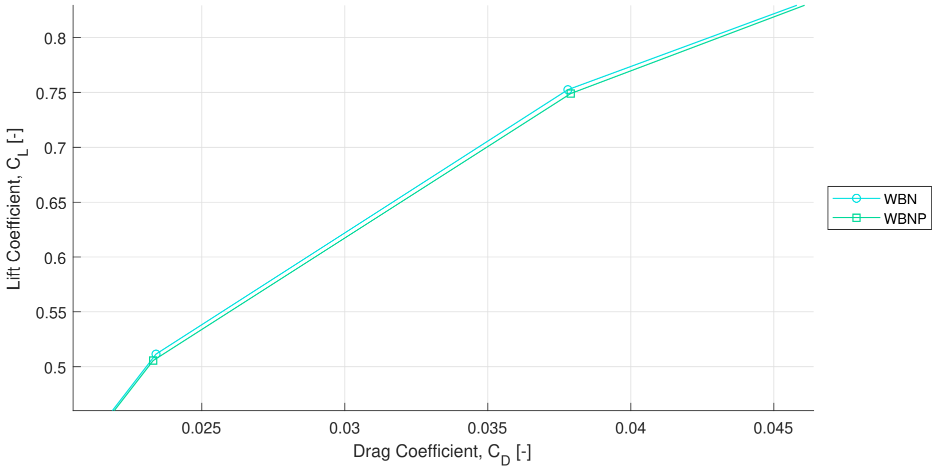

Figure 4.32: Close-up of the drag polar for the CRM WBN and WBNP at Mach 0.7, Re 5 million, for the scaled model.

The effect on the overall drag coefficient is small and is mainly due to the increased profile drag. There is also a reduction in the lift coefficient due to the interference from the pylon on the main wing. Two things can be observed: firstly, the lift induced drag reduces which shows an overall lower drag coefficient. Secondly, the effect on the pitching moment is more severe, as was also discovered in the previous section.

For calculating the drag coefficient, the pylon can be omitted. However, to be accurate in the aerodynamic center analysis, it must be included. Since this research is mainly focusing on the effect of increasing the engine size, the pylon will play a smaller role. The added complexity in modelling and meshing the pylon does not outweigh the increased solution accuracy. FlightStream also lacks the accuracy to predict complex 3D flow phenomenon which can be encountered at the wing-pylon and pylon-nacelle interfaces. For this, 3D finite volume solvers should be used.

As a conclusion, the pylon will be left out in the analysis. The results of the drag analysis will be used to compare the effects of the changes in nacelle size, nacelle wake and wing interaction. Furthermore the lift coefficient will be corrected as if the pylon was present. A correction based on the CRM validation case will be used. The two angle of attack points used for the aerodynamic center analysis are $-5\,\mathrm{deg}$ and $10\,\mathrm{deg}$. The lift and drag coefficients for those angles of attack are shown in Table 4.7. Two extra data points are chosen to average the results and capture trends.

Table 4.7: Lift and drag coefficients with drag breakdown for both CRM configurations at various angles of attack

	WBNP				**WBN**			
AOA [deg]	**C_L [-]**	**C_{D_i} [-]**	**C_{D_o}**	**C_D [-]**	**C_L [-]**	**C_{D_i} [-]**	**C_{D_o} [-]**	**C_D [-]**
-6	-0.3112	0.0034	0.0167	0.0201	-0.3051	0.0032	0.0166	0.0198
-5	-0.2268	0.0018	0.0157	0.0175	-0.2197	0.0016	0.0155	0.0171
-4	-0.1381	0.0007	0.0147	0.0154	-0.1301	0.0006	0.0143	0.0149
9	0.9672	0.0421	0.019	0.0611	0.9721	0.042	0.019	0.061
10	1.0399	0.0494	0.0213	0.0707	1.0425	0.0492	0.0215	0.0707
11	1.1075	0.0572	0.0229	0.0801	1.1113	0.057	0.0228	0.0798

The difference in values between the WBNP and WBN are shown in Table 4.8. The percentages are given with respect to the other case. It is clear that for the negative angles of attack the reduction in lift is larger compared to the higher positive angles of attack. For negative angles of attack the pylon is on the suction side of the wing where arguable the effect is more detrimental. For larger angles of attack the nacelle will shield and affect the flow over the wing where the pylon would be located. However this cannot be confirmed with FlightStream.

Changing from the WBN configuration to the WBNP configuration, the lift coefficient changes with 3.8% and -0.4% for $-5\,\mathrm{deg}$ and $10\,\mathrm{deg}$ respectively. The values follow from averaging the three angle of attack results. The pitching moment values from FlightStream also change, partly because it uses the changed lift coefficient. Because of the dependency between the two, it is not correct to simply multiply the values with a correction factor. It should be noted in the conclusions that leaving out the pylon adds to an error in the results.

Table 4.8: Lift and drag coefficients with the percentage change with respect to the opposite case

	WBNP w.r.t WBN				**WBN w.r.t WBNP**			
AOA [deg],	**C_L [-]**	**% C_L**	**C_D [-]**	**% C_D**	**C_L [-]**	**% C_L**	**C_D [-]**	**% C_D**
-6	-0.3112	2.00%	0.0201	1.52%	-0.3051	-1.96%	0.0198	-1.49%
-5	-0.2268	3.23%	0.0175	2.34%	-0.2197	-3.13%	0.0171	-2.29%
-4	-0.1381	6.15%	0.0154	3.36%	-0.1301	-5.79%	0.0149	-3.25%
9	0.9672	-0.50%	0.0611	0.16%	0.9721	0.51%	0.061	-0.16%
10	1.0399	-0.25%	0.0707	0.00%	1.0425	0.25%	0.0707	0.00%
11	1.1075	-0.34%	0.0801	0.38%	1.1113	0.34%	0.0798	-0.37%

5

Results

The results of the research are provided in this Chapter. Starting with the stability analysis for the A320 with the different engine sizes and locations as discussed in the previous Chapter. For each simulation case a small discussion on the result is given as well. Lastly, the results obtained using the Initiator are provided. The Initiator is used to evaluate the effects on the aircraft by using the different engine sizes and performance parameters.

5.1. Stability analysis Airbus A320

The results of the stability analysis of the A320 are provided in this Section. Before the results are presented, the solver settings used in FlightStream will be discussed. The following results are all for an engine retro-fit scenario.

5.1.1. FlightStream set-up

The FlightStream settings, as used in the aerodynamic center analysis, are shown in Table 5.1. The settings for the model are based on the validation of the CRM in subsection 3.2.4, with the exception of the flow separation and the boundary layer type. The turbulent boundary layer was chosen because for large transport aircraft the boundary layer is largely turbulent. From the CRM validation, it was found that non-linear effects are difficult to predict when it comes to the pitching moment. To be more consistent for all cases, the transition and separation are disabled. As a result, the drag estimation will be slightly larger for lower angles of attack. If the calculation method for the moment would be non-linear, the determination of the aerodynamic center, as described in section 4.4, would not work. Since the angles of attack are chosen within the linear regime, the result will be valid.

The flight conditions follow from the cruise Mach and cruise altitude as specified for the A320 by Airbus. The values for the viscosity and the Reynolds number are determined by using the data from the International Standard Atmosphere (ISA) and the specified cruise altitude.

Table 5.1: FlightStream settings used, with version 2020.2

Models used:	
lift	Pressure
drag	Vorticity
moment	linear pressure
Boundary layer type	Turbulent
viscous drag model	Momentum integral
Flow separation	No
Solver compressibility	Enabled
Free-stream	constant
Solver	Steady
Controller setting	

Number if iterations	1500
Convergence threshold	1.00E-06
Far field wake size	1000 %

Flight conditions	**Cruise**	**Landing**	**Take-off**	
Mach	0.78	0.4	0.23	-
Velocity	230	136	76.65	m/s
Viscosity	1.44E-05	0.0000179	0.0000179	Pa.sec
Re	2.64E+07	3.90E+07	2.20E+07	-
Reference values				
Vref	230	136	76.65	m/s
Cref	4.198	4.198	4.198	m
Sref	122.4	122.4	122.4	m2

5.1.2. A320 with reference engine

Before the engine size and location are varied, a baseline or reference needs to be set. For the wing body, the geometry of the A320 aircraft is used. Because no detailed geometry is available for the CFM56 nacelle, the (scaled) geometry of the nacelle of the CRM engine has been used. The nacelle size has been based on the size of the nacelle of CFM56 engine and scaled to represent the CFM56 nacelle. The FlightStream results are also compared with empirical relations to check for discrepancies.

A scissor plot is made to establish the possible design space for the horizontal tail. The plot is shown in Figure 5.1. The c.g. limits are based on the A320-232 and obtained from Figure 4.25. The limits are plotted for a value S_h/S that corresponds to the existing A320 aircraft.

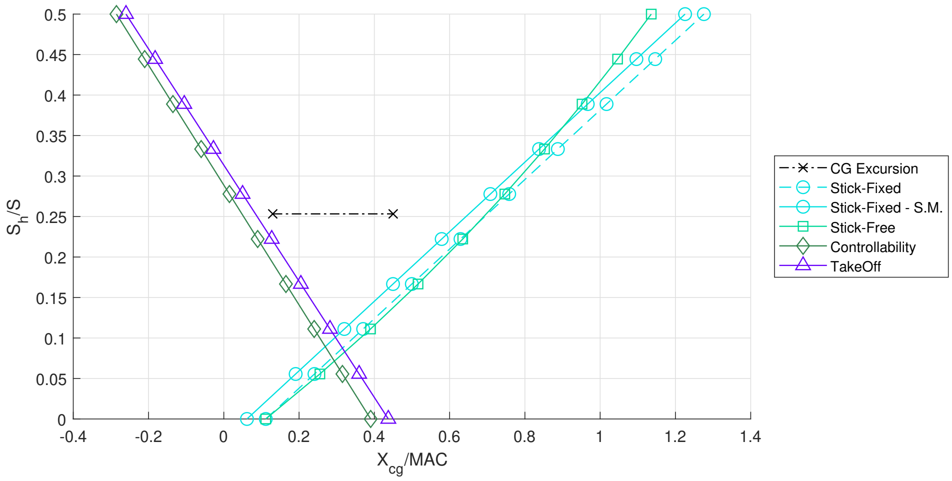

Figure 5.1: Scissor plot for the A320 aircraft using FlightStream results for aerodynamic parameters.

Quite a large discrepancy between the actual tail size and required tail size can be observed. Using the reference c.g. locations the tail can actually be quite a bit smaller. If the location of the main wing is altered as well, the required tail surface can be reduced even further. In the above figure all possible values that could be obtained from FlightStream are used. These include: the location of the aerodynamic center, the lift curve slope, the downwash and the velocity ratio. Comparing the values from FlightStream with the values from empirical relations or assumptions shows several clear differences. The values are shown in Table 5.2.

Table 5.2: Comparison between FlightStream based values and empirical values calculated using the methods described in Torenbeek [49]

	FlightStream	Empirical
x_{ac}	0.112	0.209
C_{L_α}	4.38	6.38
$C_{M_{ac}}$	-0.856	-1.066
$C_{L_{h_\alpha}}$	2.69	4.84
$d\epsilon/d\alpha$	0.133	0.424
V_h/V	0.99	0.92

The downwash calculated in FlightStream is smaller by almost a factor 3 compared to the empirical relation or the values calculated with the Initiator tool and AVL. FlightStream can generate off-body streamlines, the streamlines can be exported with the coordinates of the streamline. From the coordinates the orientation or the flow angle can be calculated. Because the angle of attack is known, the downwash angle can be calculated. Ten (10) Streamlines have been placed along the leading edge of where the horizontal tail would be, and based on the A320 reference aircraft. By calculating the angle and the average over the 10 streamlines, a downwash angle of roughly one (1) degree is found for both the -5 and 10 degrees angle of attack. The required $d\epsilon/d\alpha$ can be calculated and appeared to be a factor three (3) smaller.

Another difference is the velocity ratio which in the book of Torenbeek is assumed to be 0.92 for fuselage mounted stabilisers. The value calculated in FlightStream is much closer to 1, suggesting no real change exists in the local velocity at the horizontal tail. If the values for the downwash and velocity ratio are taken from the empirical relations, the results are quite different. Figure 5.2 shows the resulting plot.

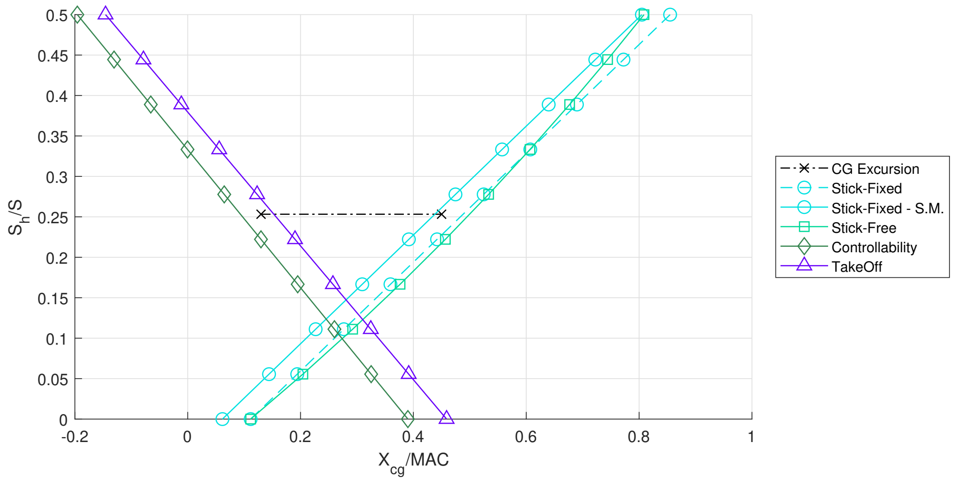

Figure 5.2: Scissor plot for the A320 aircraft using FlightStream results, with modified downwash and velocity ratio

The parameters calculated by FlightStream to be used in the analysis are: the location of the aerodynamic center, lift curve slope coefficients for the wingbody and tail, and lastly the pitching moment around the aerodynamic center.

Finally, in an effort to compare the FlightStream results with the empirical relations, another plot is made in Figure 5.3. For this plot, all parameters are determined using relations and assumptions described in Torenbeek.

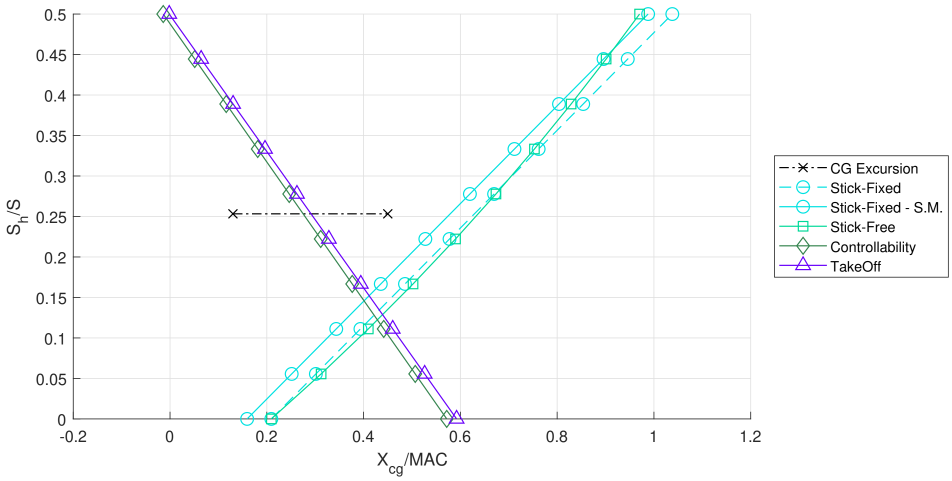

Figure 5.3: Scissor plot for the A320 aircraft using the empirical relations as provided in Torenbeek [49]

Both the FlightStream (Figure 5.1) and the empirical (Figure 5.3) scissor plots show that a different tail design is required. Both methods however show an error, but in different ways. For the FlightStream results, the slope of the criteria plots is not correct, which leads to a possible smaller tail size. Or the location of the aerodynamic center is wrong, which causes the criteria to shift to the left or right. Similarly, the empirical results show a shift in the criteria, but also a wrong slope. For the reference S_h/S, the c.g. range is 0.29 rather than the actual 0.32. From this comparison, it is not possible to say which method would work best to estimate the quantitative values. Both show errors compared to the reference material of the A320 aircraft.

5.1.3. Effect of engine location

Before the effect of the different engine sizes is investigated, first the effect of changing the engine location is checked. The main reason is to find a relation between the location of the engine and the aerodynamic center. Two engine sizes at similar locations have been evaluated. The first engine is a CFM56 engine with a geometry based on the CRM nacelle. Two flight conditions are checked: cruise and landing. These are the two flight conditions for which the stability analysis is done. The results for the cruise condition are shown in Table 5.3.

Table 5.3: The a.c. location $x_{ac}/\bar{c}$ [-] for the A320 airframe with a CFM56 type engine. Evaluated at different locations (percentile change w.r.t reference value), at cruise condition

	backward up	up	forward up	
	2.90%	2.72%	1.64%	
backward	4.26%	**0.122**	-0.37%	forward
	8.02%	4.86%	2.53%	
	backward down	down	forward down	

The value in bold shown in the center of the table is the $x_{ac}/\bar{c}$ (dimensionless) for the reference location. The reference location is similar to that of the original CFM56 engine. The percentages in the table are the changes with respect to the bold reference value. Negative values mean the aerodynamic center has moved forward, positive values mean the aerodynamic center has moved backward. Looking at Table 5.3 it can be observed that for mostly all cases (except the forward case) the aerodynamic center has moved back. Similar trends are can be seen when considering the landing conditions, as shown in Table 5.4. The differences are less severe compared to cruise conditions.

Moving the engine up and down has a significant effect and in both cases causes the aerodynamic center to move backwards. If the change was due to the tangential force, which is omitted (as explained in section 4.4), a different result would be expected. If the tangential force causes a shift, the effect should be reversed whether the engine is moved up or down. When the engine is moved down, the moment will be larger and more significant. When the engine is moved up the moment reduces and

Table 5.4: The a.c. location $x_{ac}/\bar{c}$ [-] for the A320 airframe with a CFM56 type engine. Evaluated at different locations (percentile change w.r.t reference value), at landing conditions

	backward up	up	forward up	
	2.63%	3.09%	2.46%	
backward	2.25%	**0.102**	-2.44%	forward
	5.01%	2.90%	0.06%	
	backward down	down	forward down	

one would expect the aerodynamic center to move forward.

It should be noted that although the changes of 5% seem large, in absolute values it means a 4 cm shift. With respect to the location of the c.g. of the A320 (1.34m, see Figure 4.25), the shift is 3%. For the larger engine (LEAP-1A), the magnitude of the changes is slightly more, however the absolute values are very similar. Table 5.5 shows the results for the cruise conditions with the larger engine. Locations are the same as for the previous engine.

Table 5.5: The a.c. location $x_{ac}/\bar{c}$ [-] for the A320 airframe with a LEAP-1A type engine. Evaluated at different locations (percentile change w.r.t reference value), at cruise condition

	backward up	up	forward up	
	-7.63%	-2.48%	-6.20%	
backward	1.70%	**0.109**	-4.10%	forward
	2.26%	-2.21%	-7.27%	
	backward down	down	forward down	

The landing conditions for the larger LEAP-1A engine are shown in Table 5.6. Where the smaller CFM56 engine shows a similar trend between the cruise and landing conditions, quite a difference exists for the LEAP-1A engine. If the engine is moved down, not much changes can be seen, suggesting that very little interference at this location will occur. For the engine moved up, the effect is literally reversed. For the cruise condition, the aerodynamic center moves forward and for the landing condition the aerodynamic center moves backwards. When the aerodynamic center moves forward, either the nacelle produces more lift, or the wing produces less lift. Between the two flight conditions, only the Reynolds number is changing significantly. The same effect is present for the smaller CFM56 engine. This leaves only interference between the two bodies as a possible source for the difference.

Table 5.6: The a.c. location $x_{ac}/\bar{c}$ [-] for the A320 airframe with a LEAP-1A type engine. Evaluated at different locations (percentile change w.r.t reference value), at landing conditions

	backward up	up	forward up	
	0.12%	2.97%	5.23%	
backward	3.15%	**0.0955**	-0.39%	forward
	2.28%	-2.23%	-6.83%	
	backward down	down	forward down	

A clear distinct dependency cannot be observed from these results. Without performing an aerodynamic analysis, in which the wing and nacelle are evaluated together, it is not possible to link the engine location to the aerodynamic center. The difference between the small and large engine however is quite significant. For the cruise conditions the $x_{ac}/\bar{c}$ goes from 0.122 to 0.109, a -10.6% shift. A second conclusion can be that the engine size, or the magnitude of the nacelle lift, is more important. Important for the analysis is that the effect of the engine weight on the c.g. is not taken into account. The engine shift will cause a shift in c.g. as well.

5.1.4. Change in center of gravity due to new engine weight

The larger engine has a different weight compared to the original engine for which the c.g. limits (in Figure 4.25) are defined. On top of the changed engine weight, the engine location is also changed. Both have an effect on the aircraft c.g. location.

To determine the new c.g. locations, first the c.g. location of the aircraft without the tail is determined. The reference engine weight follows from the dry engine mass of the IAE V2500 corrected with the nacelle weight as was done in subsection 4.3.3. The location follows from the service manual [46]. The c.g. limits from Figure 4.25 are converted to absolute values rather than fractions of the MAC. Using the nose as a reference location, the moment of the aircraft weight around the nose can be calculated using: $W_{aircraft} \times cg_{aircraft}$. Subtracting the moment of the engine, $W_{engine} \times cg_{engine}$, and dividing by the weight of the aircraft minus the engine yields the c.g. without the engine. In an analogous way the new engine can be added and the new c.g. limits can be calculated. The results are shown in Figure 5.4 for the three different location cases. Where **Case 1** is the fixed engine location (gully distance decreases), **Case 2** is the spanwise constant location (gully distance fixed, engine moved forward and down), and **Case 3** is the constant aircraft c.g. (gully distance fixed, engine moved down and outboard). In all cases the aircraft has not changed.

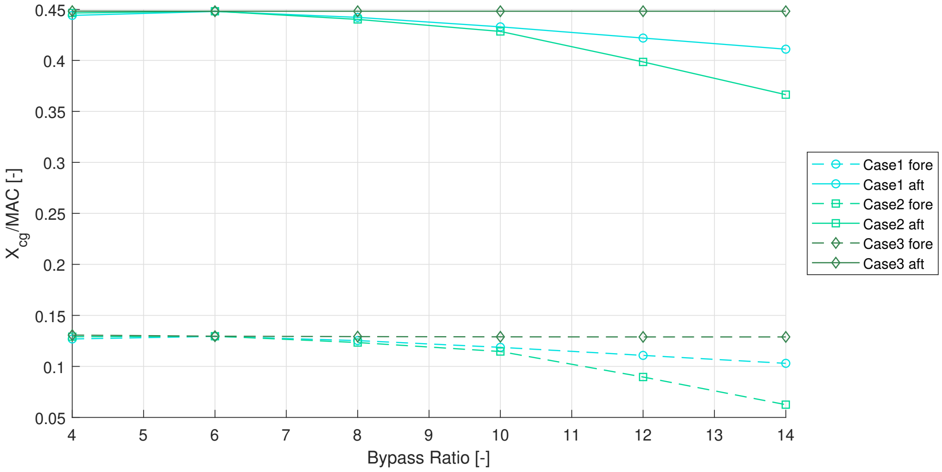

Figure 5.4: Forward and backward c.g. limits for the A320 airframe with different engines. Three different cases indicate the different engine locations.

5.1.5. Changing the bypass ratio for a fixed engine location [Case 1]

The effect of the increased bypass ratio on the stability characteristics and tail design are discussed. Firstly the engine is kept at the same location, so no correction for interference, ground clearance or c.g. location is required (only gully distance decreases). Purely the effect of the engine size is considered. For three conditions (cruise, landing, take-off) the change in location of the aerodynamic center as function of the bypass ratio is shown in Figure 5.5.

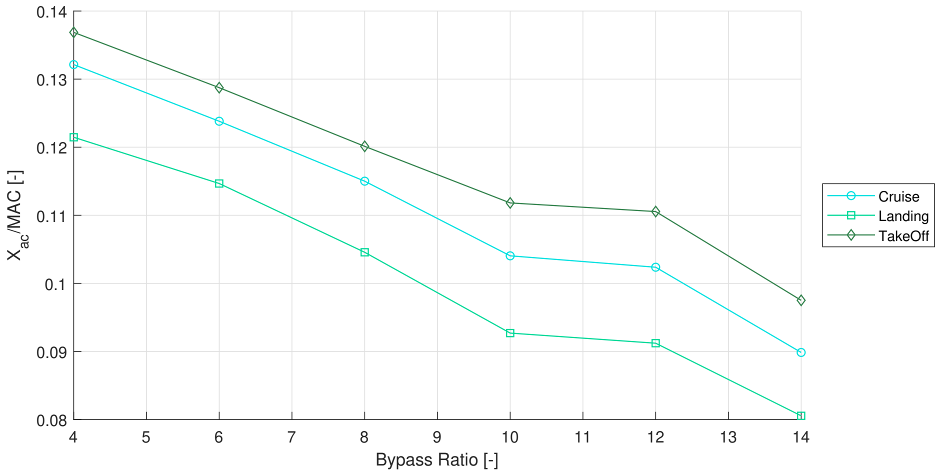

Figure 5.5: Change of the aerodynamic center with respect to changing engine size for a retro-fit scenario.

A clear trend between the engine size (bypass ratio) and the location of the aerodynamic center is visible. For larger engines the aerodynamic center moves forward. This can be explained by two factors. Firstly the larger nacelle produces more lift which shifts the aerodynamic center forward. Secondly the wake behind the larger nacelle affects a larger area of the main wing resulting in a forward shift of the aerodynamic center. Apart from the discontinuity between BPR 10 and 12 the change is almost linear. The discontinuity is present in all three flight conditions which indicates it is not a numerical anomaly. However no clear reason for the discontinuity can be given. From BPR 8 to 9 the slope increases, then decreases after which it increases again. The changes in geometry of the engines are linear, however this trend is not seen here.

In the tables shown in subsection 5.1.3 can be seen that the aerodynamic center moves forward if the flight condition changes from cruise to landing. This trend is further confirmed in the graph above. However, for the take-off condition, the aerodynamic center moves the other way (backward). It corresponds to the Reynolds number and Mach number, see Table 5.1. The Reynolds number will influence the boundary layer thickness and momentum. Typically, the transition point, separation zone, and shock waves will be changed. In this FlightStream analysis, the transition point is fixed and no separation or shockwaves are modelled. This leaves only the pressure distribution as a cause. The Reynolds number will affect the pressure distribution and will cause the airfoil to be more front loaded. Or the 3D pressure profile over the wing changes such that the wing root becomes higher loaded for higher Reynolds numbers.

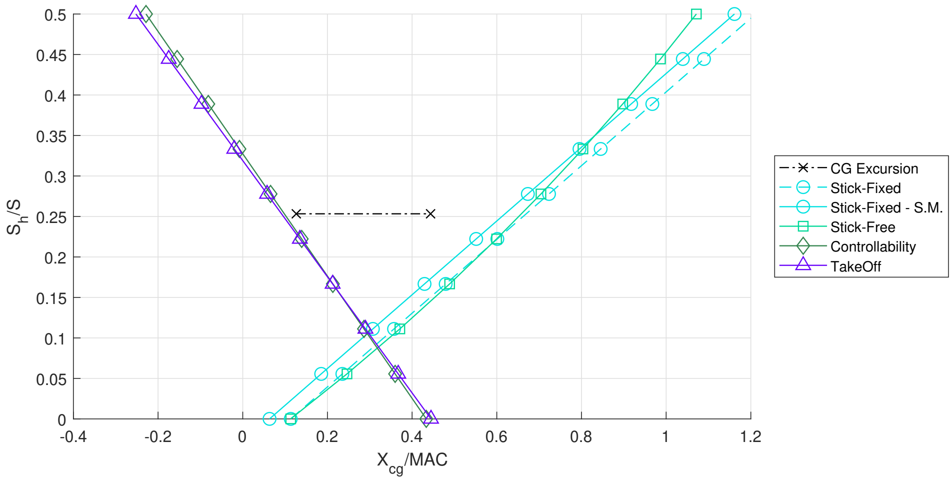

Figure 5.6: Scissor plot for Bypass ratio 4 with corrected CG excursion for a retro-fit scenario.

The stability plots for a bypass ratio 4 and bypass ratio 14 are shown in Figure 5.6 and Figure 5.7 respectively. At first glance no significant difference can be seen between the two graphs. When looking closer, the entire graph is shifted to the left. The c.g. excursion is also shifted to the left due to the changed engine weight. The larger engine is heavier which causes the c.g. to shift forward.

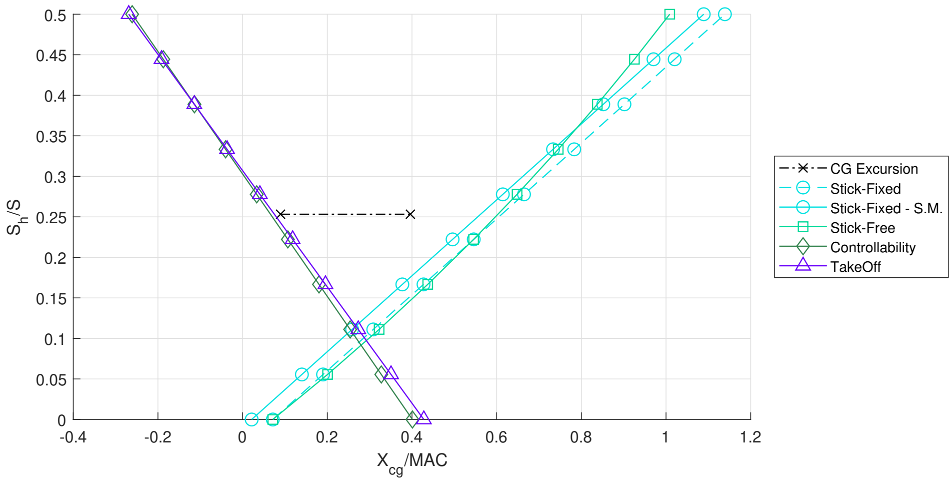

Figure 5.7: Scissor plot for Bypass ratio 14 with corrected CG excursion for a retro-fit scenario.

Similar to the reference A320 case shown in Figure 5.1 the tail can be made smaller for the specified c.g. range. There is one restriction: the main wing should also be moved. If the main wing is not moved, the forward c.g. limits will be constraining.

5.1.6. Changing bypass ratio for a fixed engine location with jet flow

In this case the jet flow from the engine and the engine inlet flow are taken into account. The nacelle shapes and locations are kept the same as in the previous section. The jet flow can have a significant effect on the wake and the wing performance. It should be noted that the included jet only effects the interference between the jet stream and the surrounding elements. Secondly the jet flow is modelled based on an assumed jet velocity, density and jet spreading. Since no information about the actual jet flow is known, general assumptions are made based on a CFM56 engine. The effect of the jet spreading, for example how the jet stream expands after the exhaust, is not known and should be investigated further.

Figure 5.8 shows the change in aerodynamic center for different bypass ratios with the jet flow included. Again the trend between the flight conditions, Reynolds number and aerodynamic center is visible. It can be noted that unlike the previous case without the jet flow, the location of the aerodynamic center stays practically the same for all bypass ratio's. The difference between the aerodynamic center in take-off and landing condition is very large. As a result the landing and take-off condition in the stability plot are spaced far apart, see Figure 5.9. The graph is not realistic and the results should be interpreted with caution.

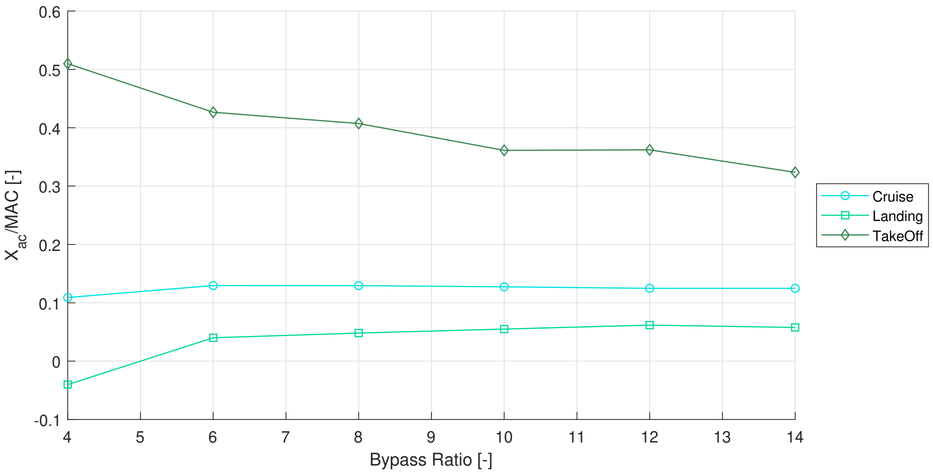

Figure 5.8: Change of the aerodynamic center with respect to changing engine size for a retro-fit scenario.

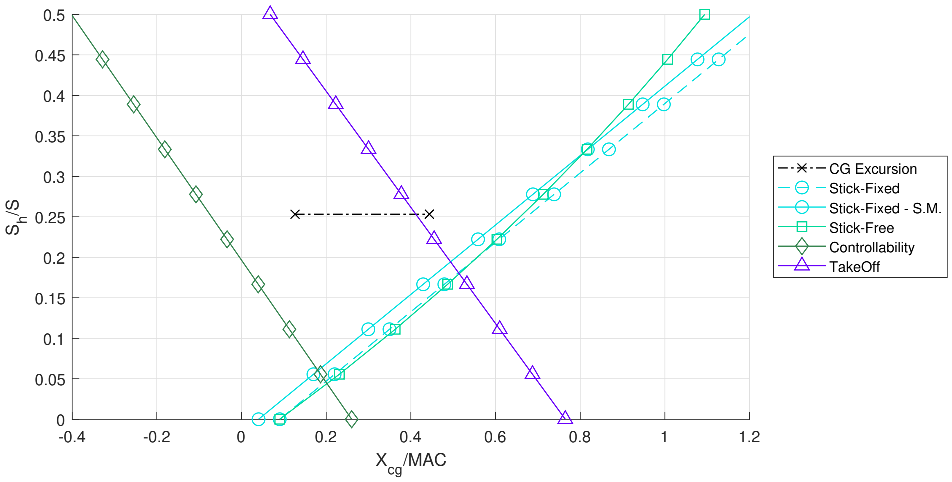

Figure 5.9: Scissor plot for bypass ratio 4 with corrected CG excursion and jet flow for a retro-fit scenario.

Figure 5.10 shows the stability plot for the bypass ratio 14. Still there is a rather large difference between the controllability curve and take-off curve compared to the curves in the previous section (without the jet stream) and to the curves of the reference case. The reason for the offset follows from the difference in the location of the aerodynamic center. The slope of both curves is still almost parallel, just like the case without the jet flow.

A possible cause for the shift to the left of the take-off curve is the magnitude of the thrust. For cruise and landing conditions, the thrust is relatively low compared to the take-off thrust. The effect of the jet flow is therefore small and the results are similar to the results of the case without a jet flow. For take-off the effect of the jet flow is much more significant. It should be said that the effects captured here are the interference effects between the jet flow and the surroundings. The actual thrust force and its effect on the aerodynamic center is taken into account for all cases.

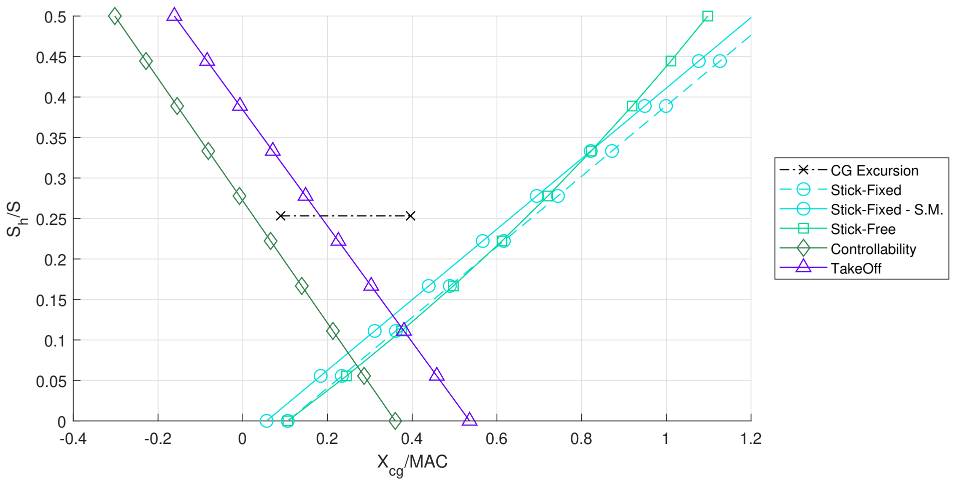

Figure 5.10: Scissor plot for Bypass ratio 14 with corrected CG excursion and jet flow for a retro-fit scenario.

The c.g. ranges corresponding to the reference tail size are shown in Figure 5.11. The dotted line is the c.g. range without the jet flow. The outlier at BPR 4 is visible again and should be ignored. Furthermore, the c.g. range now increases with bypass ratio rather than decreases. Although less than the aforementioned case, the c.g. range is still larger compared to the original c.g. range (0.32 $\bar{c}$). The major reason for the difference is the take-off criterion. If the take-off criterion is ignored (square green line in Figure 5.11) the c.g. range shows similar trends compared to the no jet case, but the values are still larger.

For completeness, the effect of the jet flow should be incorporated in the analysis. However compared to the calculated c.g. range, the values will not be more accurate. With the jet flow incorporated, the absolute value for the c.g. range improves, but looking at the stability plot in Figure 5.10, it is clear that for the given forward c.g. position the take-off criterion is not met. In the end the effect of the changed engine size can be evaluated, but for quantitatively good values adding the jet stream does not matter.

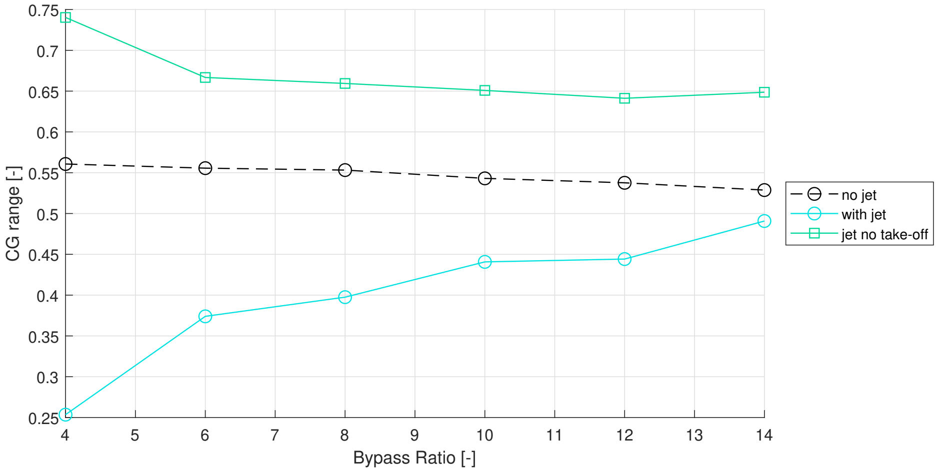

Figure 5.11: CG range for different bypass ratios and fixed engine location for a retro-fit scenario.

5.1.7. Changing bypass ratio with fixed spanwise location [Case 2]

Typically, the engine location is changed when an existing airframe is retro-fitted with a new (larger) engine. The following set of results are linked to the spanwise fixed engine location. The engine is moved forward and up, contrary to the previous results, to preserve the ground clearance. Figure 5.12 shows the location of the aerodynamic center. The trend in the graph is similar to that of the fixed engine location in Figure 5.5. However the bend at BPR 10 and BPR 12 is not present here. The effect of the flight conditions is also similar to that of the fixed engine location, with the exception that the take-off curve is closer to the cruise curve.

The downward slope, or the aerodynamic center moving forward with increasing bypass ratio, can be explained by the increased lift produced by the nacelle. On top of that, the larger engine wake affects the main wing and reduces the lift from the main wing. The trend is linear up to BPR 12. The sudden increase in slope can be explained by the location of the BPR 14 engine. In order to maintain proper ground clearance the BPR 14 engine has to be moved quite far forward. This can be seen in the location of the aerodynamic center for the aircraft.

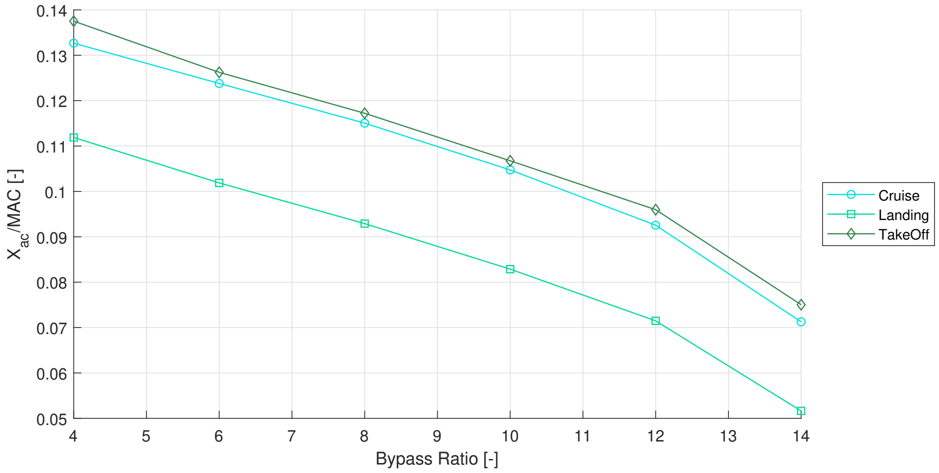

Figure 5.12: Change in aerodynamic center location with bypass ratio for the spanwise fixed location

Figure 5.13 and Figure 5.14 show the scissor plots for the BPR 4 and BPR 14 engines respectively. Similar to the fixed engine location in the previous section, the forward c.g. limit is close to the limiting criteria. For the BPR 14 the criteria actually limits the c.g. and the tail must be larger to accommodate the required c.g. excursion.

Furthermore the change in the location of the aerodynamic center can be seen again. The criteria are shifted to the left. The engine with a BPR 14 moves further forward causing a larger c.g. shift forward. As a result the take-off criterion becomes a limiting factor. The actual c.g. range which is possible with the given tail size, is still quite large.

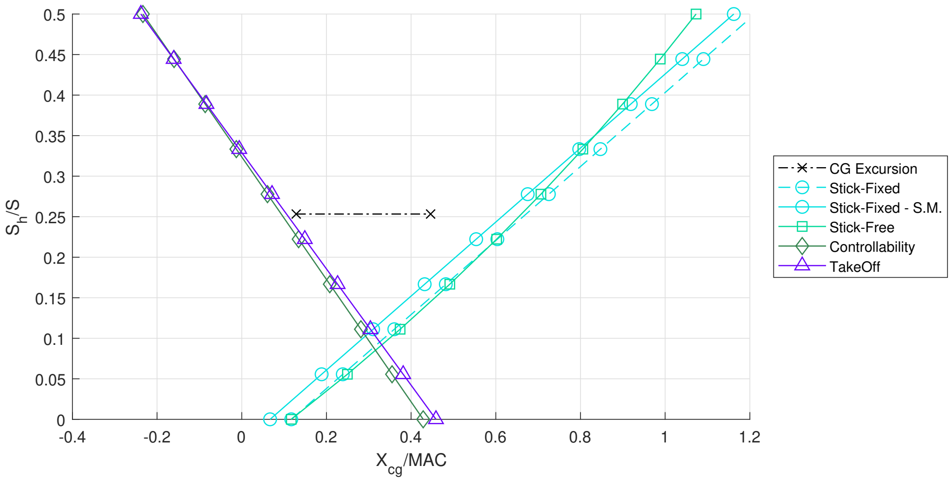

Figure 5.13: Scissor plot for bypass ratio 4 with corrected CG excursion for a retro-fit scenario.

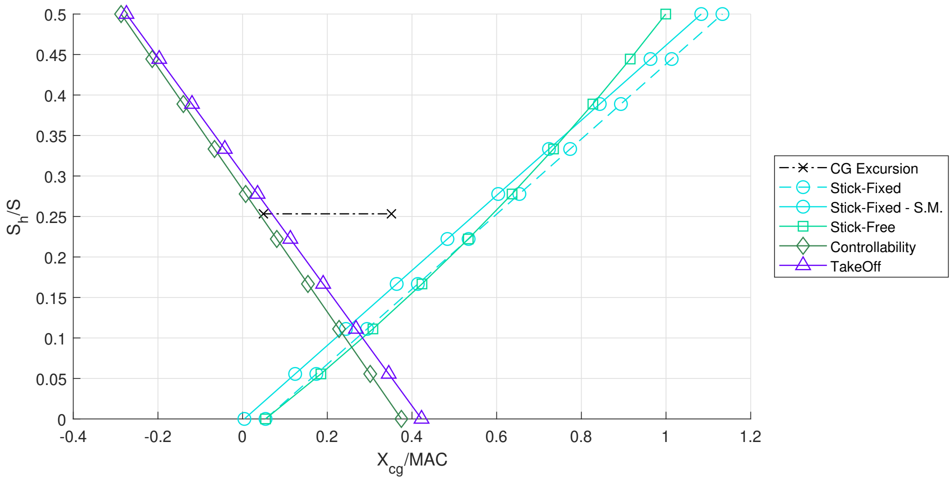

Figure 5.14: Scissor plot for bypass ratio 14 with corrected CG excursion for a retro-fit scenario.

5.1.8. Changing bypass ratio with a fixed aircraft c.g. [Case 3]

The last set of results is obtained by varying the bypass ratio and keeping the c.g. fixed. The engine is moved in order to preserve ground clearance and the same gully distance, however the c.g. of the total aircraft is kept the same. The engine location is adapted for the increase in engine weight to keep a fixed c.g. of the aircraft. A heavier engine will be closer to the airframe c.g., and a lighter engine will be further forward. The resulting c.g. will be constant for all engine sizes. Figure 5.15 shows the change in aerodynamic center with respect to the bypass ratio. For this case, it is interesting to note that the location of the aerodynamic center also moves forward with the engine size increasing. For the larger engines (BPR 10 to 14), the engine effectively moves backwards. Compared to the spanwise fixed case (dotted line), the location of the aerodynamic center changes very similar. Both cases use a different method for locating the engine and yet the results are similar. An argument can be made that the change in aerodynamic center is more dependent on the engine wake affecting the main wing rather than the actual engine location. The lift produced by the nacelle is negligible compared to the lift produced by the wing. It can be concluded that the engine location is not a driving factor for the location of the aerodynamic center. Contrary, the engine diameter is a driving factor as it influences the wing lift distribution.

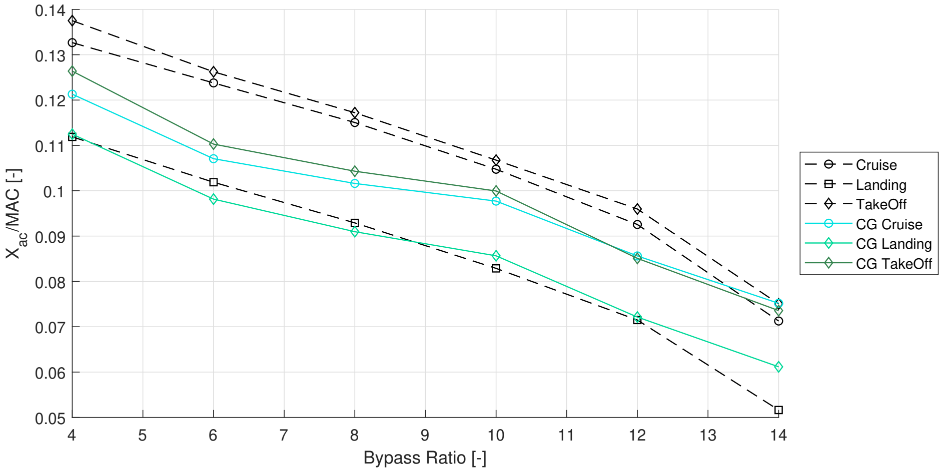

Figure 5.15: Change in the location of the aerodynamic center with bypass ratio and fixed c.g. of the aircraft for a retro-fit scenario.

Figure 5.16 and Figure 5.17 show the scissor plots for the smallest and largest engine considered. Again the trend looks very similar to that of the previous cases, with the exception of the c.g. excursion remaining constant. The criteria still shift left for increasing engine size. Consequently, the forward c.g. limit moves further away from the criteria, resulting in a possibly smaller tail section.

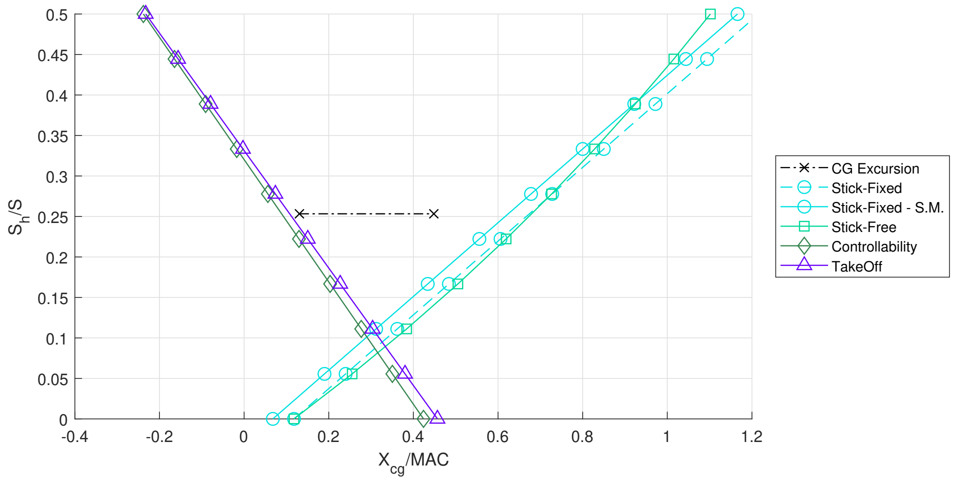

Figure 5.16: Scissor plot for bypass ratio 4 with corrected CG excursion for a retro-fit scenario.

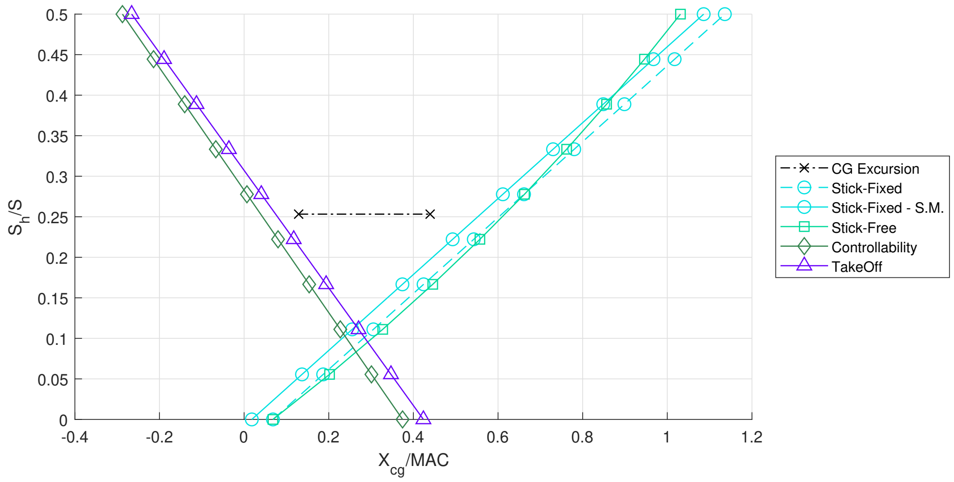

Figure 5.17: Scissor plot for bypass ratio 14 with corrected CG excursion for a retro-fit scenario.

From Figure 5.16 and Figure 5.17 it can be seen that the take-off criterion becomes dominant for BPR 14. It does not shift as far left as compared to the controllability criterion. A likely consequence will be a reduced c.g. margin, which is discussed in the next section.

5.1.9. Effect on the horizontal tail design

Combining the results from the previous section, a conclusion on the tail design can be drawn. Firstly, the c.g. margins can be determined. The c.g. margin is the distance between the forward and backward c.g. limit, for the A320 the margin is 0.32. The c.g. margin is dependent on the tail size and the criteria. To make a fair comparison, the tail size for the A320 is used as a reference and corresponds to a value of 0.253 for S_h/S. The results for the different cases as well as the calculated A320 c.g. margin are plotted in Figure 5.18. The calculated A320 line is based on the results from subsection 5.1.2.

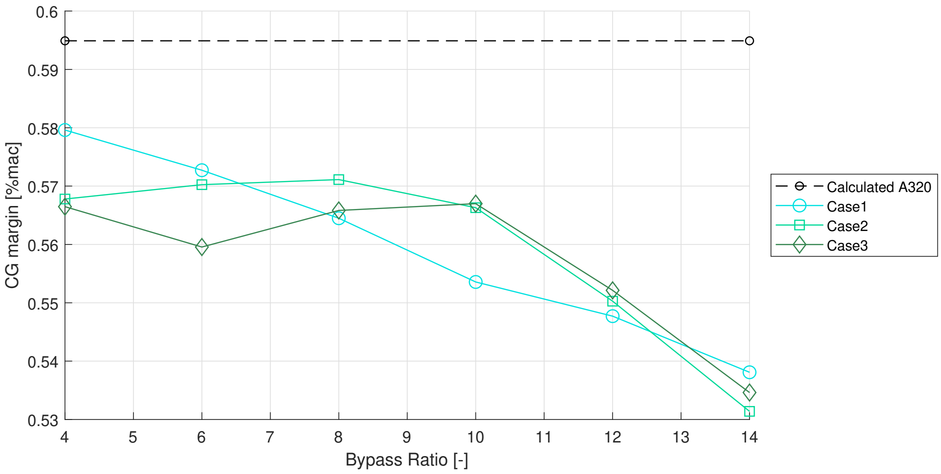

Figure 5.18: C.g. margins for all three engine location cases compared to the calculated A320 (engine based on A320 engine size) for a retro-fit scenario.

All three engine location cases show a fairly similar trend. In all cases the c.g. margin decreases with an increasing engine size. The engine location seems to be less important, although there is a difference between all three cases. In case 1 the engine location is kept constant and the c.g. margin decreases with a nearly constant slope. By moving the engine, case 2 and 3, the effect of the increasing engine can be mitigated until a point is reached where a drop off starts.

The differences between the largest and smallest c.g. margin for case 1, 2 and 3 is -7.16%, -6.96% and -5.71% respectively. The typical value used for the stability margin (a safety factor in the c.g. margin) is 5%. By increasing the engine size, the complete stability margin can be nullified. It is worth noting that the actual c.g. margin for the A320 is 0.32 instead of the 0.58, which is calculated using this analysis. This is a 81% difference. With such a large deviation, it is difficult to say whether the calculated difference is an actual consequence of the engine change, or if it is an analysis/numerical error that becomes less significant.

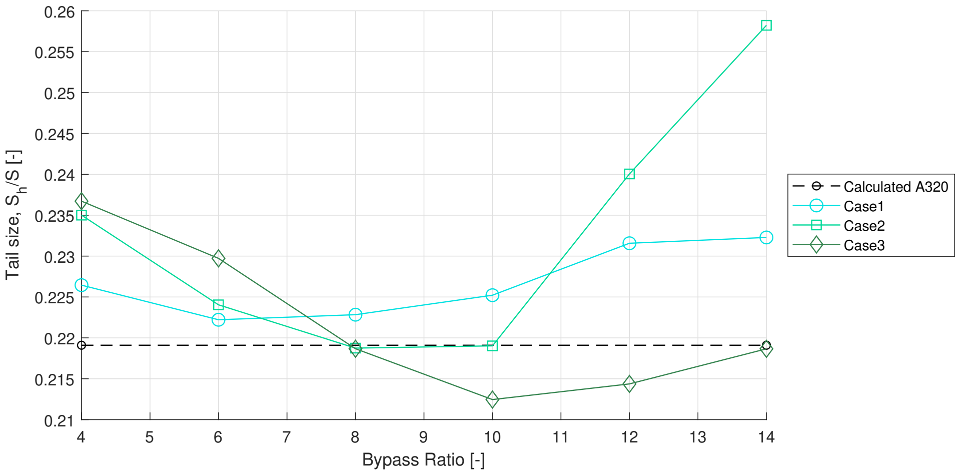

Figure 5.19: The horizontal tail size for the three engine location cases compared to the calculated A320 (engine based on A320 engine size) for a retro-fit scenario.

For this analysis, 4 criteria were used in the stability analysis. More criteria can be formulated regarding the control forces. A certain tail size is required to minimise the required elevator control forces during a manoeuvre. It is possible that these control forces are the limiting factors, and can therefore result in smaller calculated c.g. margins. These criteria were not used since they required more assumptions and knowledge about the control systems, which is not readily available. Furthermore, the methods described by Torenbeek are for mechanical control systems with cable and pulley systems. The A320 uses a fly by wire control system for which these methods are not valid.

Figure 5.19 shows the effect of the increased engine on the tail size. Whereas the c.g. margins showed some consistency for all the engine location cases, the tail size is less consistent. For case 1, the tail has to increase by a maximum of 4.5% between BPR 6 and BPR 14. The maximum required increase in tail size occurs in case 2: 18% between BPR 8 and BPR 14. The explanation follows from the individual stability plots. The forward c.g. location is limited in all cases. The changes in the aerodynamic center, C_{L_α}, and $C_{M_{ac}}$ cause the criteria to shift. However, the change in c.g. location, due to the changed engine location and weight, is far more a driving factor. This is demonstrated by the fact that case 2 (where the engine moves farthest forward) shows the largest change. Compared to the actual A320, the tail can generally be smaller. In the most severe case (BPR 14, case 2), the calculated tail size is only 2% larger compared to the tail size of the A320.

The same reasoning can be used to explain why for case 3 the tail size decreases. From Figure 5.16 and Figure 5.17 it can be seen that the c.g. remains in the same location while the criteria shift to the left. The effect from the change in aerodynamic parameters is also visible. From BPR 10 onwards, the decreasing trend in tail size stagnates and actually reverses. The same aerodynamic effect is visible in Figure 5.18 where after BPR 10 the c.g. margin starts to decrease rapidly.

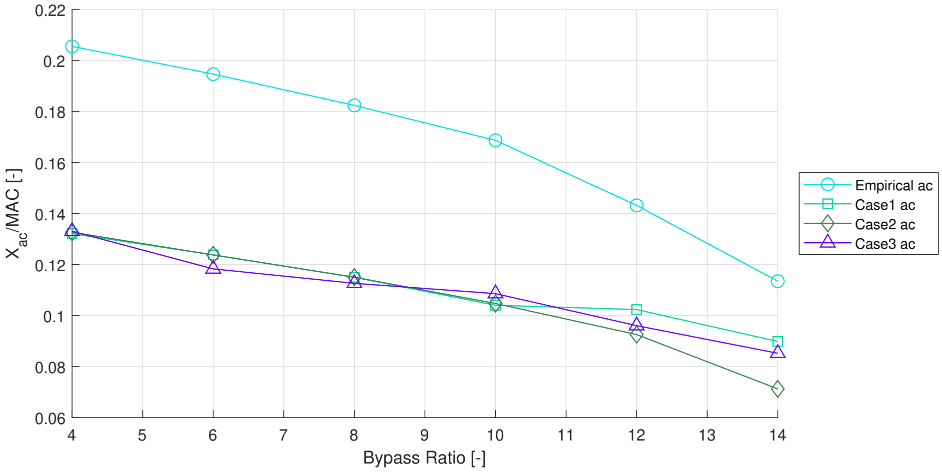

Figure 5.20: Aerodynamic center location for different engine sizes for all engine location cases. Compared to the a.c. calculated from the empirical relation in Torenbeek.

Figure 5.20 can be made by comparing the FlightStream results for the aerodynamic center with the results obtained from the empirical relations. The results of the calculation of the aerodynamic center with FlightStream show similar trends (especially for case 2) to that of the calculation with the empirical relation. The largest difference between the cases happens at BPR 14, suggesting that the engine location is less important compared to the engine size. The large difference between the absolute values calculated with the empirical relation and FlightStream is not possible to explain. For a thin airfoil, the aerodynamic center will be at the quarter chord point. For finite wings with thick airfoils, the aerodynamic center will move slightly. Adding the fuselage and nacelle will shift the aerodynamic center forward. Which method is most accurate cannot be said. The effect of the increasing engine size is taken into account when the empirical relation is used. The empirical relation seems to capture the trend found by FlightStream quite well.

5.2. A320 Drag results

Using the new tail sizes, a new FlightStream analysis is done for the cruise conditions. The smallest required tail and largest required tail are used. These are the BPR 10 for the case 3 engine location and BPR 14 for the case 2 engine location. The geometry consists of the wingbody, nacelle and the new horizontal tail. In Figure 5.21 the drag polars for the two tail sizes are plotted. For the dotted lines, the nacelle is included, whereas the solid lines show the results without the nacelle. The effect of the tail size can be isolated. When the nacelle is excluded, FlightStream shows a lower drag for the larger horizontal tail. This is against expectations and can only be explained by a numerical error in FlightStream.

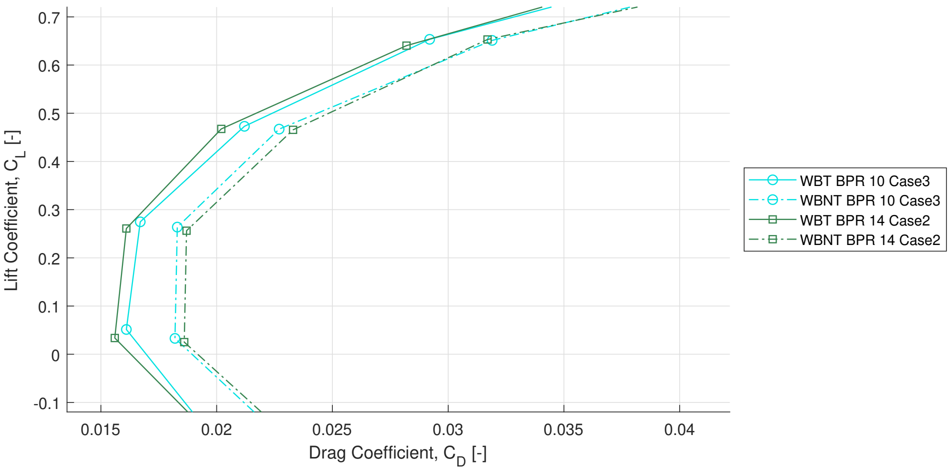

Figure 5.21: Drag polars for the two extremes in the tail size. Plots for the whole aircraft (WBNT) and wingbody+tail without the nacelle (WBT) are shown.

A similar anomaly happens in Figure 5.22. Two engine sizes are analysed. The wingbody and nacelle are run together and separately (result of wingbody and nacelle is added). From theory, the drag should increase if the wingbody and nacelle are run together because of the interference drag between the two bodies. This happens for the BPR 14 engine, however for the BPR 6 engine, the drag is lower. This suggests that the interference drag is negative, which is not possible.

The origin of the reduction in drag lies in the lift induced drag, C_{D_i}. The C_{D_0} is either similar or larger when the engine or tail size are increased. However, the reduction in lift coefficient means a lower total drag coefficient.

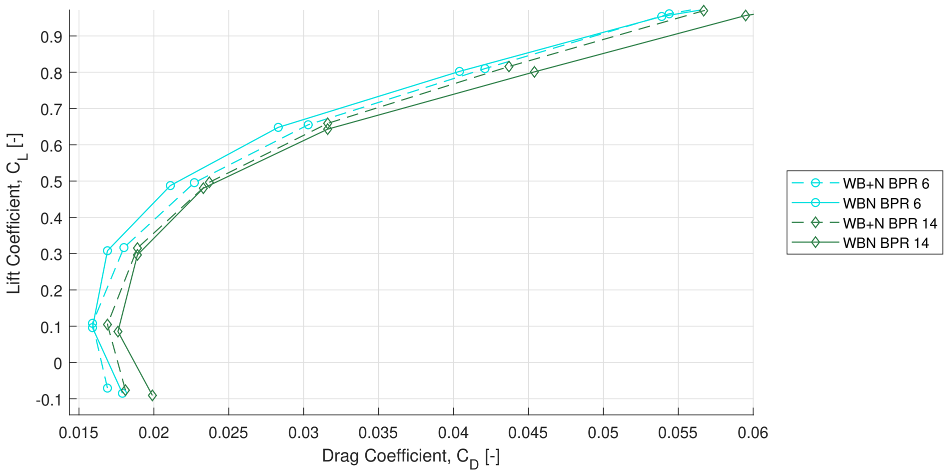

Figure 5.22: Drag polars for two engine sizes for case 1 engine location. The wingbody and nacelle are evaluated together (WBN) or separately (WB+N) and then added.

To further quantify the effect of the nacelle on the aircraft, Figure 5.23 shows the pressure plot for a wingbody and wingbody + nacelle. When the nacelle is included, the suction peak at the leading edge of the wing is significantly reduced. Apart from the leading edge, the C_P distribution is very similar. The effect of the nacelle on the trailing edge is negligible. The difference at the leading edge causes a loss in lift production for this section. Part of the lift loss is resolved by the nacelle producing lift. In the end there is a loss in total lift, as was also shown for the CRM in subsection 3.2.4.

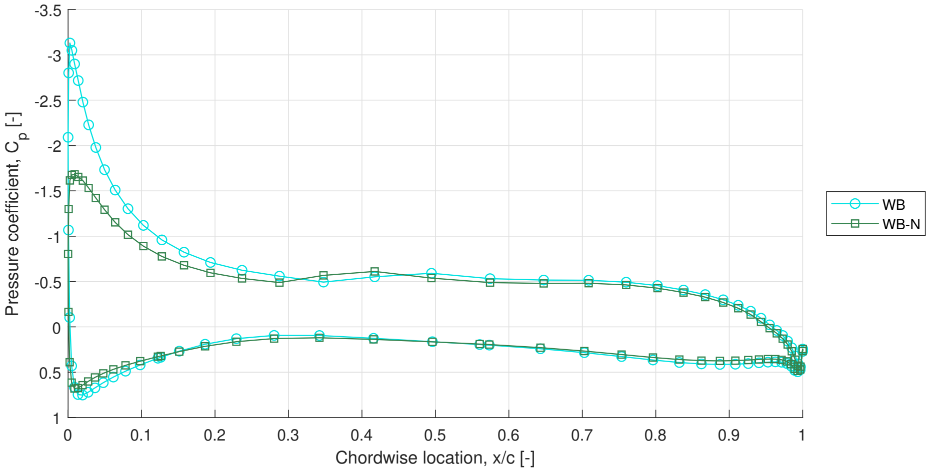

Figure 5.23: Pressure coefficient at 5.5m from the fuselage centerline. Angle of attack is 6° at cruise conditions. Plot for the wingbody without a nacelle (WB) and for a wing with nacelle present (WB-N)

Figure 5.24 shows the effect of the angle of attack and engine size on the pressure distribution for a wing section. For both angles of attack, the suction peak at the leading edge is reduced when the engine size is increased. On the pressure side, similar patterns are visible for the different angles of attack. Between the WB and WBN in Figure 5.23 there is a 11% decrease in sectional lift coefficient C_l when the engine is included. The change from a BPR 6 to BPR 14 results in a 5.2% drop in sectional lift coefficient C_l. The effect of the engine size is quite drastic. Simply the increase in engine size is half of the effect of adding an engine to a bare wing. For these plots only one section is considered, but the loss in lift happens for more spanwise sections and results in the reduced lift coefficient.

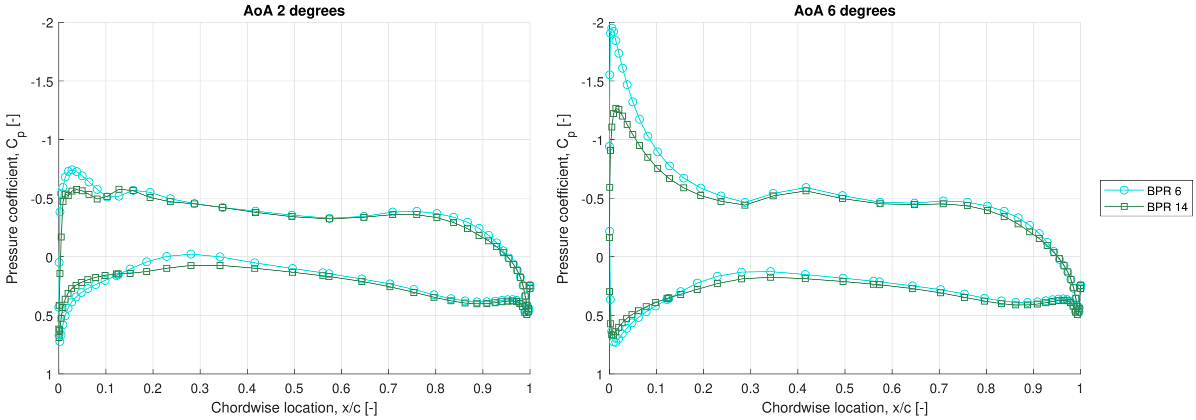

Figure 5.24: Pressure coefficient at 5.5m from the fuselage centerline. For two angles of attack at cruise conditions. Plot for two different engine sizes. Engine location follows case 2.

The effect on the pressure distribution is further visualised in Figure 5.25. The higher pressure, as can be seen in the C_p plot for the single section, occurs along a larger section of the wing. In this case the pressure increases with engine size, despite that the channel between the wing and nacelle converges. The increased nacelle causes a larger stagnating effect. The wake from the nacelle is likely to interfere with the pressure side. Since the wake is a relatively low velocity flow, the pressure will be higher compared to the pressure side that sees more free-stream flow.

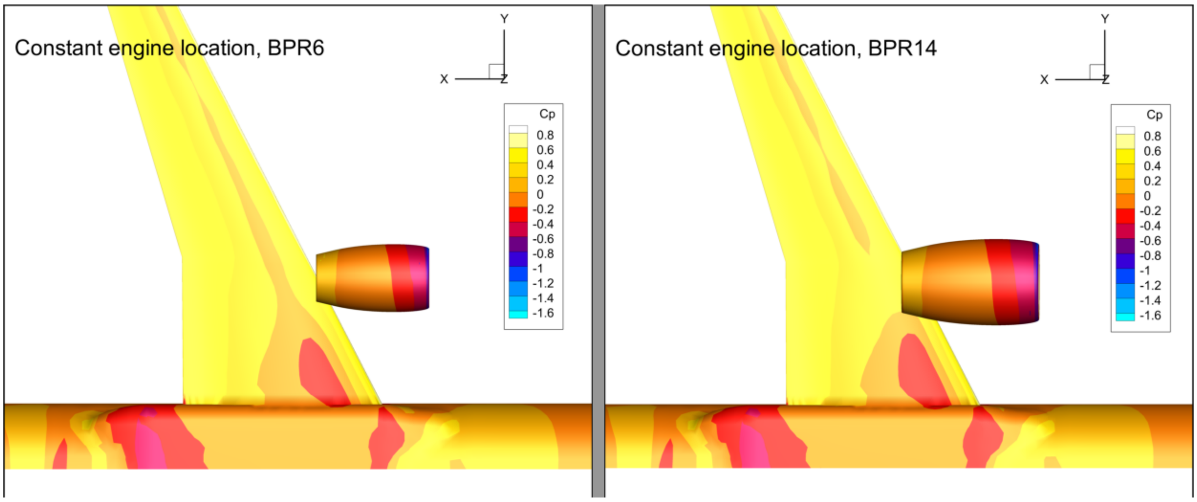

Figure 5.25: Pressure coefficient contour plot of the A320 (bottom view). For 2° angle of attack at cruise conditions. Plot for two different engine sizes. Engine location follows case 2.

5.3. Initiator results

The different engines with the different bypass ratio's, weights, SFC and nacelle size are used as a fixed input in the Initiator. Other input parameters are based on a A320 type aircraft with constant payload and mission requirements. The top level requirements are provided in Table 5.7

Table 5.7: Top level requirements for the Airbus A320-200 used in the analyses

Parameter	Value	Unit
Pax	156	-
Payload mass	20536	kg
Cruise Mach	0.78	-
Cruise Altitude	11280	m
Harmonic range	3917	km
Takeoff dist.	1938	m
Landing dist.	1480	m

The engine dimensions corresponding to the various BPR were fixed in the input file. The spanwise engine location was kept similar to location in the A320 reference file. The vertical location is kept constant as well, meaning the center line of the engine remains at the same place. Effectively, the distance between the engine and wing becomes smaller, as well as the ground clearance if the landing gear is not modified. The results of the two calculated aircraft are shown in Figure 5.26 to Figure 5.27.

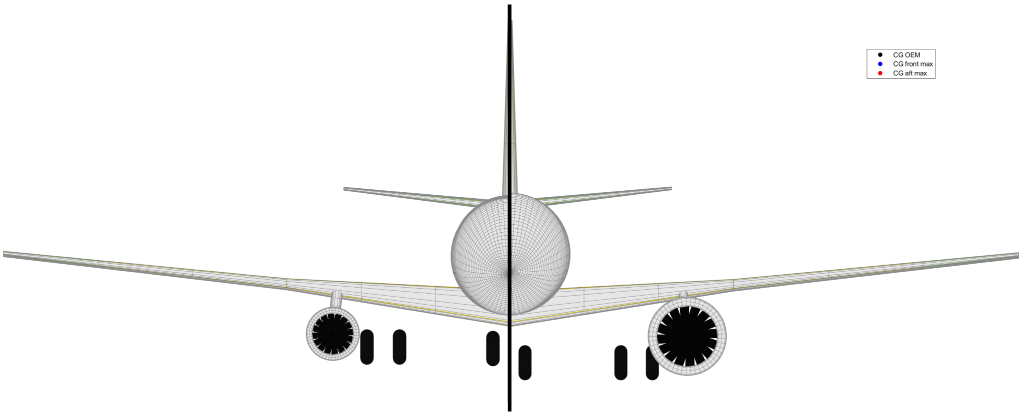

Figure 5.26: Front view of the aircraft with an engine with a BPR 4 (left) and BPR 14 (right)

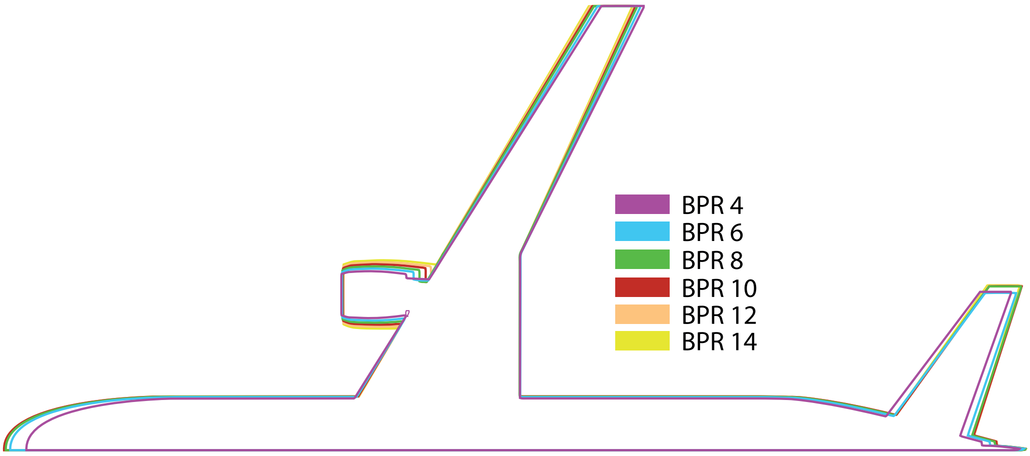

Figure 5.27: Top view of the aircraft planform for changing engine size with an aircraft redesign

Apart from visually identifying the changes, the next graphs show various aircraft parameters as function of the bypass ratio. Although the BPR is not directly related to these parameters, it represents the different engines. Firstly, Figure 5.28 shows the relation between the different engines and the maximum take-off mass (MTOM) and the operational empty mass (OEM). Both masses decrease with the increasing engine size despite the increase in engine weight with increasing BPR. However, the OEM stagnates at roughly BPR 8 and for BPR 10, it increases again. The decrease in mass can be explained by the improved SFC that corresponds with the larger bypass ratio.

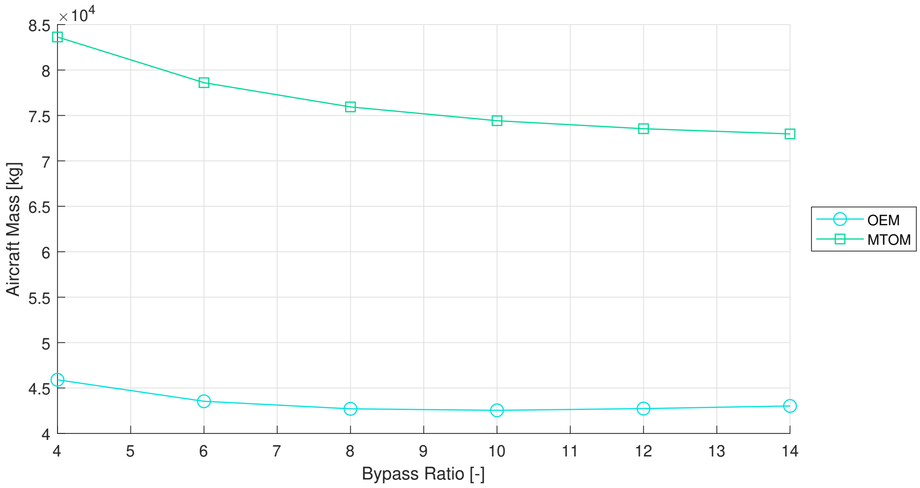

Figure 5.28: Aircraft OEM and MTOM for the different bypass ratio’s, after a full aircraft redesign.

With the improved SFC, the required fuel for the same mission reduces. Less fuel results in a lower MTOM. The fuel burn for the harmonic mission (range at maximum payload mass) is shown in Figure 5.29. The graph shows three plots; the harmonic mission results for a changing engine with changing SFC, a fixed SFC with the changing engine, and a fixed engine size and weight with the changing SFC. The effect of the changing engine is minimal compared to the effect of the SFC. With the engine increasing in size (thus increasing the drag and increasing the weight), the overall increase in fuel burn is 5.9%. However, the decrease in fuel burn due to the improved SFC is 53%. When the SFC and engine effects are considered together, the fuel burn drops by 50%.

The fuel burn curve for the harmonic mission does show a slight flattening. However, the engine can be larger and heavier before this minimum fuel burn is reached. At that point, the fuel burn curve looks like the SFC vs BPR curve in Figure 4.2, which is used to estimated the fuel burn of the engines in the first place.

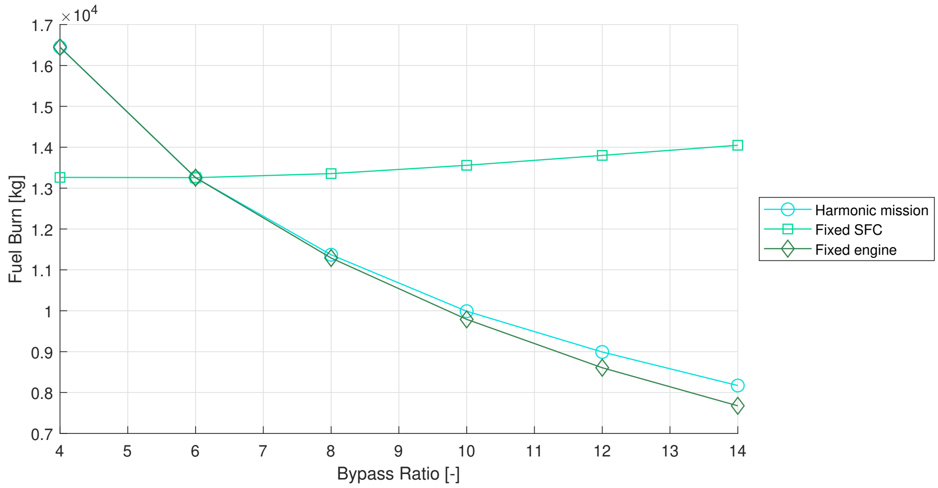

Figure 5.29: Aircraft fuel burn for the different bypass ratio's, after a full aircraft redesign.

Looking at the lifting surfaces, Figure 5.30 shows the wing surface area together with the empennage surface area. The surface area's can be related back to the OEM as they are interdependent. The basic statistical relation for the calculation of the tail surface area (as used in the Initiator) result in a small effect on the tail size. Also, from the results obtained from the more elaborated stability analysis (as described before), the horizontal tail would not change much either based on the stability requirements.

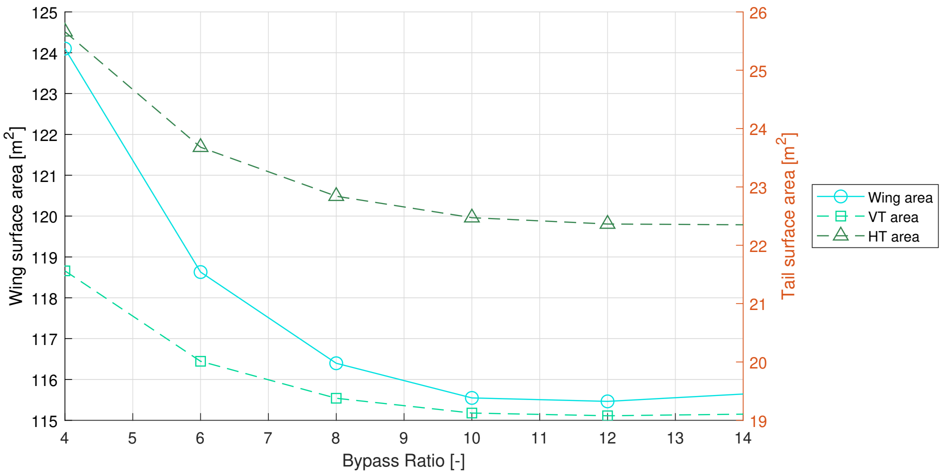

Figure 5.30: Aircraft main wing and empennage surface area, after a full aircraft redesign.

The reason why the fuel burn keeps on decreasing while the change of the OEM and wing surface area starts to stagnate, can be further explained when looking at the wetted area. The wetted area versus the bypass ratio is plotted in Figure 5.31 and actually shows an increase in wetted area. Since the wing and empennage do not increase in area, the reason is purely the larger nacelle due to the larger BPR. The wetted area is used for the drag estimation and will negatively affect the drag.

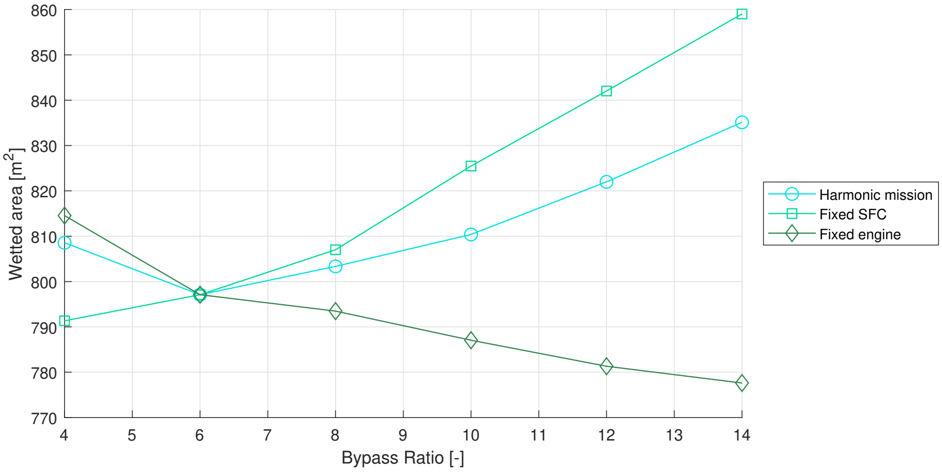

Figure 5.31: Wetted area for the different bypass ratio's, after a full aircraft redesign.

It is likely that the slope reduction in the fuel burn is caused by the increased drag due to the increased wetted area. The SFC of the engine itself still becomes better, even for larger BPR. The increased drag causes a decrease in performance gain. However, there is still a performance gain, even at larger BPR. For larger BPR, the location and the engine (nacelle) must be optimised for ground clearance. The reason for not further increasing the BPR lies in practical limitations such as mounting the engine under the wing of a low wing aircraft. The fan size also has limitations based on the fan tip velocity. This depends also on the fan shaft speed and other factors. If tuned accordingly, the engine size can increase further.

In Figure 5.32 the forward and backward c.g. location are plot. The c.g. limits stay roughly similar for all bypass ratio's despite the change in engine weight. In Figure 5.27 the changed planform is shown. The change in complete aircraft geometry causes the c.g. limits to barely shift. Unlike the c.g. limits for the engine retro fit analysis in Figure 5.4, where the limits do change and shift forward for increasing engine size. There is also very little difference between the results of the harmonic mission (where the engine and SFC changed), the fixed SFC and the fixed engine cases. The Initiator seems to converge to these c.g. limits for this aircraft, despite the different design limitations.

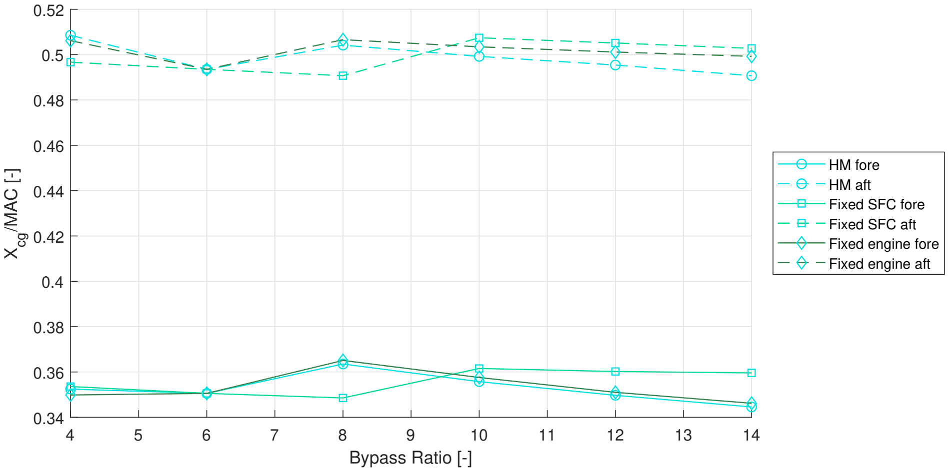

Figure 5.32: C.G. limits for the different bypass ratio's, after a full aircraft redesign.

6

Conclusions

In this research, the installation penalties of gas turbine engines on an aircraft are investigated. One of the parameters to improve the gas turbine efficiency is the bypass ratio. Increasing the bypass ratio will result in a larger engine, has more wetted area, creates more drag, and will be heavier. The engine weight has an effect on the location of the center of gravity of the aircraft. The change in location of the center of gravity affects the aircraft pitching characteristics.

From the literature study can be concluded that determining the overall engine installation penalty is a difficult task. An aircraft is a complex system and practically all components are linked to each other. The Initiator toolbox developed by the TU Delft aerospace faculty is a tool that can synthesise a preliminary aircraft design based on a set of input requirements. Most methods used in the Initiator are based on empirical methods from conceptual aircraft design books, such as 'Synthesis of subsonic airplane design' by E. Torenbeek and 'Aircraft Design - A Conceptual Approach' by Daniel P. Raymer. These methods make use of older data, when the engine bypass ratio was still small. By using the Initiator tool, an aircraft design has been made for different bypass ratio's and corresponding engine parameters. The fuel burn (for the design mission) is the most important aircraft parameter to reduce. With the lower fuel load, the airframe can become lighter, which in turn means a further reduction in fuel load. Despite the increase in drag due to the larger surface area of the engine and the increase in engine weight, the improvement in specific fuel consumption of the aircraft negates all of the installation penalties.

The Initiator tool has some shortcomings for analysing the installation penalties. For example, it does not consider the interference effects between the nacelle and the main wing. The iterative nature makes it difficult to include other programmes. A stand alone analysis has been done based on an engine retro-fit on an existing aircraft. For example, the 737 MAX showed a changed pitching moment characteristic after it had been retro-fitted with larger engines with an high bypass ratio. Using a more comprehensive aerodynamics solver (such as FlightStream), the aerodynamic parameters have been determined and used for a stability analysis. With this simulation program, some of the aerodynamic interference effects are captured. Furthermore, the location of the aerodynamic center can be calculated with more accuracy rather than using an empirical relation. The engine location, as well as the engine size, have been varied to assess the effect on the aerodynamic center. Using the FlightStream results, scissor plots are made to determine the possible center of gravity (c.g.) range. With this tool it was not possible to relate the calculated c.g. excursion to a reference c.g. excursion based on the A320-232. Nevertheless, it was possible to evaluate the differences between the various engine sizes. The change in c.g. excursion, as a result of the change in bypass ratio, can be considered significant. A change up to -7.1% was observed. The typical stability margin is 5% of the c.g. range. Because there is a large error between the calculated and real c.g. range, the validity of the -7.1% can be questioned. The difference can also be attributed to an error becoming smaller.

A reflection on the research questions as specified in chapter 1 is given below:

- **How does the engine bypass ratio relate to the engine performance and size?**
  Preferably, the specific fuel consumption (SFC) of the engine should be determined using an engine design tool. However, most tools need multiple input parameters, which for this study,

were not known. The only known input parameter was the bypass ratio. Choosing a set of inputs that would work for all bypass ratio's was not an option. Optimising the inputs for efficiency or engine mass also yielded unusable results. To solve this problem, the engine emission databank by the ICAO was used to create a regression curve between the bypass ratio and the SFC. The relation between the bypass ratio and the SFC is not an one-to-one dependency, other engine performance gains, due to improved components, are also included. The engine size follows from statistics and shows a fairly linear trend between the bypass ratio and engine size.

- **What are the engine installation penalties on the aircraft aerodynamics?**
  To evaluate the full extend of the interference between the nacelle and the wing, a Navier Stokes solver should be used. Such a solver will take too much computing time for a preliminary design. As an alternative the simulation program FlightStream has been used. FlightStream needs less computing time, however, has also less accuracy. With this simulation program the aerodynamic effect of adding an engine can be analysed. The drag increase, as well as a small drop in lift production, can be calculated. This effect is validated with the NASA Common Research Model (CRM). Flow separation effects are not well captured by FlightStream. Although the point of separation can be determined, the consequential increase in drag not. Also shock waves cannot be calculated, which means that possible shock formation at nacelle-pylon-wing intersections cannot be evaluated. Lastly, the 3D geometry input is very important for the final results. An analysis of the installation penalties has been done on the A320 aircraft. As a full 3D model of the A320 was not available, the geometry used is based on two schematic drawings. The wing geometry follows from interpolated graphs out of a book.
- **How does the addition of an engine change the weight distribution of the aircraft?**
  During the preliminary design phase it will be difficult to estimate the stability characteristics of the aircraft. Even when using more sophisticated tools to determine the aerodynamic parameters, it will be still complicated. Changing the weight of the engine will result in a shift in the c.g. location. The secondary weight effects, such as engine supports or wing bracing due to the heavier engine, are difficult to estimate. The effect on the tail design can be analysed with the help of the changed c.g. range. The changes in the aerodynamic center and wing performance can reduce the c.g. range by around 7.1%. This means that practically the entire stability margin is lost.

A conclusive answer to the main research question: **For narrow wing/body aircraft, can the installation penalties from an increase in bypass ratio outweigh the gain in specific fuel consumption?** can unfortunately not be given. The graph that comes closest to Figure 1.1 is the fuel burn plot in Figure 5.29. If the gain in SFC is large enough and the entire aircraft can be redesigned, the installation penalties will not outweigh the gains in fuel burn. The possible fuel save, that for example can be achieved by increasing the bypass ratio, will negate the engine weight penalty, drag penalties and depreciated aerodynamic performance. The engine itself will become the limiting factor, rather than its installation penalties. At some point, the fan will be too large and will create supersonic flow, or the engine diameter will be too large and ground clearance will be the limiting factor.

In case of an engine retro-fit, the changed aircraft c.g. limits and aerodynamics may require a larger tail. There is certainly an effect on the c.g. margin, however the effect does not directly lead to further penalties, or drastic redesigns. The new required tail size compared to the A320 is marginally larger: 2.0%. The added drag is negligible. If the stability characteristics are kept the same, as was done for the 737 MAX, it is possible that the SFC gains are lost. However not through installation penalties, but through performance loss.

7

Recommendations

Based on the results, conclusions and lessons learnt during this Thesis, several recommendations are formulated for future work. The recommendations can be split: firstly, recommendations on how to improve the results and conclusions obtained in this report. Secondly, to further expand on the Thesis topic of engine installation penalties. And lastly, general recommendations following from the experiences gained during the Thesis.

- The Initiator only considers the lifting surface, no fuselage and nacelle are taken into account. FlightStream added a higher level of fidelity to the results. However, FlightStream is not capable to capture all aerodynamic effects, for example shock waves. To capture all the aerodynamic interference effects, a higher fidelity CFD solver should be used. Studies have been done on the effects of the engine nacelle shape and the engine location. Repeating these studies is not advised. The results can be used to improve the empirical relations in the Initiator.
- The geometry used was without a pylon and with a through flow nacelle. The pylon was a source of errors during meshing and therefore omitted. Although FlightStream can model inlets and exhaust actuators, the results could not be validated and were therefore not used. To improve the accuracy of the analysis, these components must be added and must be validated.
- A more detailed stability analysis can be done if more aircraft stability parameters are known. Typically, these parameters follow from windtunnel or even flight testing. Obtaining these parameters through CFD and possibly FlightStream, could provide valuable information in the early design process on the aircraft stability characteristics.
- In principle, the Initiator toolbox is a powerful tool when it comes to preliminary aircraft design. However, over the years a lot of code has been added and many lines of code have become obsolete. As a result, the files have become incoherent, bug fixing is very difficult and time consuming. Also the programme structure is spread out over multiple files, making it hard to find which modules are actually used and which are skipped. Cleaning up the directories and modules would help significantly. The Initiator is primarily used as a conceptual design tool. It performs an iterative weight convergence for which it uses analysis modules. It is possible to run modules separately, but this can quickly run into problems such as missing inputs, or inputs that change because they are needed in the weight convergence. It will be a benefit if the Initiator can be used as an analysis tool without having to fully define the aircraft first.

A

FlightStream Validation data

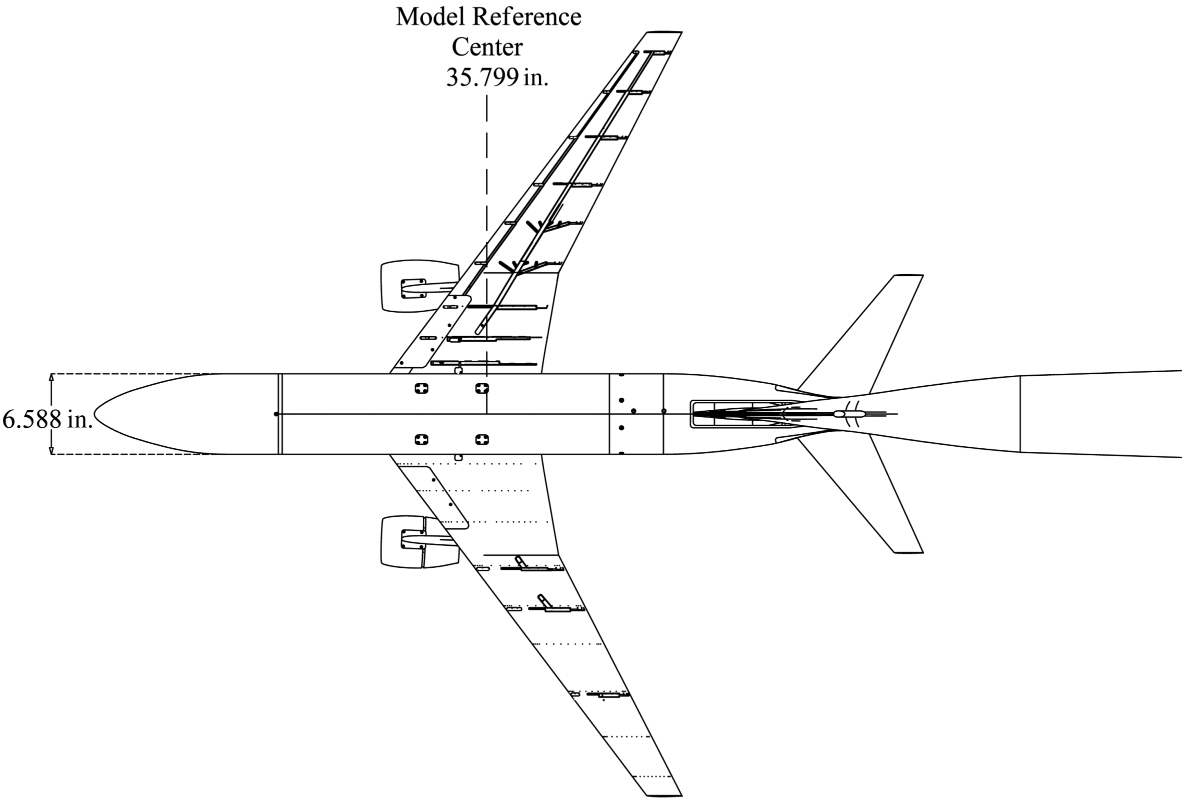

a) Top view

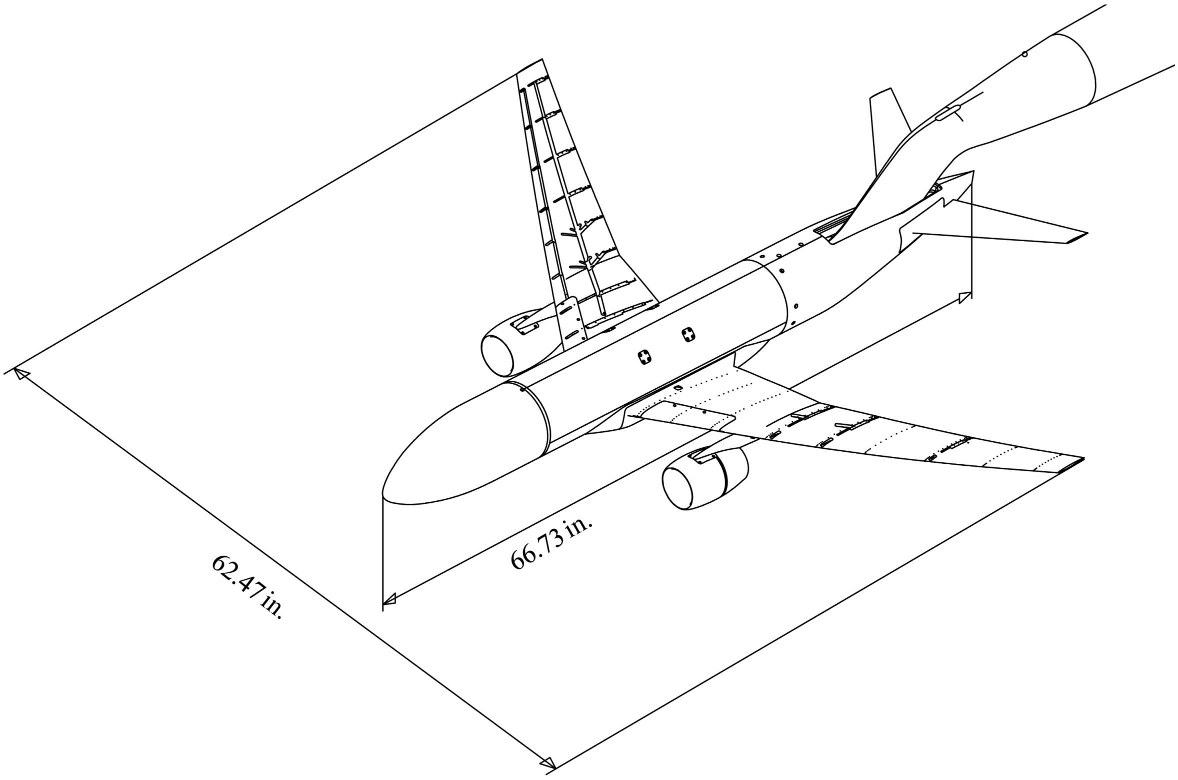

b) Isometric view

Figure A.1: Schematic of the scaled CRM windtunnel model

Table A.1: AMES experimental windtunnel data for the NASA CRM WB

ALPHA	MACH	CREYN	CS2S_CL	CS2S_CD	CS2S_CS	CS2S_CRM	CS2S_CPM	CS2S_CYM
-2.977	0.700	5.000	-0.1541	0.0154	0.0001	-0.0013	-0.0275	0.0001
-2.013	0.701	5.005	-0.0558	0.0141	-0.0004	-0.0013	-0.0312	0.0000
-1.017	0.700	5.003	0.0447	0.0137	-0.0010	-0.0013	-0.0353	0.0000
-0.003	0.700	5.000	0.1464	0.0143	-0.0011	-0.0013	-0.0388	0.0000
0.998	0.700	5.002	0.2471	0.0157	-0.0017	-0.0014	-0.0416	0.0000
2.002	0.700	5.001	0.3470	0.0178	-0.0020	-0.0014	-0.0436	0.0000
2.266	0.700	5.002	0.3725	0.0186	-0.0022	-0.0014	-0.0440	0.0000
2.525	0.700	5.003	0.3979	0.0194	-0.0023	-0.0014	-0.0442	0.0000
2.818	0.700	5.002	0.4256	0.0203	-0.0022	-0.0013	-0.0443	0.0000
3.078	0.700	5.003	0.4514	0.0212	-0.0024	-0.0013	-0.0441	0.0000
3.351	0.700	5.003	0.4772	0.0223	-0.0023	-0.0013	-0.0436	0.0000
3.599	0.699	5.000	0.4996	0.0233	-0.0024	-0.0013	-0.0428	0.0000
3.855	0.700	5.003	0.5237	0.0245	-0.0025	-0.0013	-0.0420	-0.0001
4.115	0.700	5.004	0.5484	0.0258	-0.0026	-0.0013	-0.0409	-0.0001
4.372	0.700	5.002	0.5733	0.0273	-0.0025	-0.0013	-0.0393	-0.0001
4.630	0.699	5.001	0.5986	0.0289	-0.0025	-0.0014	-0.0378	0.0000
4.874	0.700	5.004	0.6223	0.0308	-0.0030	-0.0014	-0.0364	-0.0001
5.143	0.700	5.003	0.6480	0.0330	-0.0026	-0.0015	-0.0350	-0.0001
5.626	0.700	5.003	0.6934	0.0375	-0.0027	-0.0017	-0.0322	-0.0001
6.146	0.699	5.001	0.7397	0.0434	-0.0026	-0.0021	-0.0280	-0.0001
6.669	0.700	5.003	0.7756	0.0510	-0.0031	-0.0016	-0.0163	-0.0001
7.168	0.699	5.002	0.7834	0.0619	-0.0023	-0.0010	-0.0052	0.0000
7.662	0.700	5.003	0.7913	0.0759	-0.0029	0.0014	0.0070	0.0005
8.159	0.700	5.003	0.8078	0.0903	-0.0029	0.0019	0.0130	0.0007
8.680	0.700	5.004	0.8288	0.1048	-0.0031	0.0025	0.0160	0.0009
9.188	0.700	5.003	0.8500	0.1189	-0.0027	0.0043	0.0182	0.0013
9.681	0.700	5.003	0.8698	0.1323	-0.0034	0.0057	0.0195	0.0015
10.194	0.701	5.004	0.8856	0.1455	-0.0032	0.0053	0.0234	0.0016
10.653	0.700	5.003	0.9020	0.1578	-0.0030	0.0052	0.0272	0.0017
11.174	0.700	5.002	0.8764	0.1676	-0.0021	0.0117	0.0355	0.0025
11.682	0.700	5.003	0.8930	0.1809	-0.0023	0.0131	0.0354	0.0027
12.191	0.700	5.000	0.8980	0.1924	-0.0023	0.0131	0.0347	0.0026

Table A.2: AMES experimental windtunnel data for the NASA CRM WBNP

ALPHA	**MACH**	**CREYN**	**CS2S_CL**	**CS2S_CD**	**CS2S_CS**	**CS2S_CRM**	**CS2S_CPM**	**CS2S_CYM**
-2.968	0.700	5.005	-0.1809	0.0196	0.0002	-0.0014	-0.0659	0.0001
-2.019	0.700	5.002	-0.0837	0.0173	0.0001	-0.0013	-0.0606	0.0000
-1.017	0.700	5.003	0.0212	0.0163	-0.0002	-0.0014	-0.0560	0.0000
-0.029	0.700	5.001	0.1237	0.0165	-0.0010	-0.0014	-0.0514	0.0000
0.989	0.699	5.000	0.2283	0.0176	-0.0014	-0.0014	-0.0467	0.0000
1.991	0.700	5.000	0.3317	0.0196	-0.0020	-0.0014	-0.0419	0.0000
2.273	0.700	5.001	0.3598	0.0204	-0.0017	-0.0014	-0.0404	0.0000
2.526	0.700	5.002	0.3855	0.0212	-0.0019	-0.0014	-0.0391	0.0000
2.754	0.700	5.002	0.4099	0.0219	-0.0021	-0.0014	-0.0377	-0.0001
3.072	0.701	5.007	0.4404	0.0231	-0.0019	-0.0014	-0.0362	0.0000
3.305	0.700	5.003	0.4669	0.0238	-0.0018	-0.0014	-0.0344	0.0000
3.577	0.699	5.002	0.4914	0.0251	-0.0023	-0.0014	-0.0326	-0.0001
3.845	0.700	5.005	0.5192	0.0262	-0.0023	-0.0014	-0.0304	-0.0001
4.098	0.700	5.005	0.5433	0.0275	-0.0022	-0.0014	-0.0282	-0.0001
4.380	0.700	5.004	0.5697	0.0291	-0.0027	-0.0014	-0.0255	-0.0001
4.635	0.700	5.000	0.5933	0.0307	-0.0023	-0.0013	-0.0225	-0.0001
4.868	0.700	5.000	0.6165	0.0322	-0.0018	-0.0014	-0.0195	0.0000
5.155	0.700	5.002	0.6430	0.0345	-0.0019	-0.0014	-0.0167	0.0000
5.636	0.700	5.003	0.6921	0.0387	-0.0028	-0.0016	-0.0123	-0.0002
6.152	0.700	5.001	0.7429	0.0443	-0.0025	-0.0020	-0.0077	-0.0001
6.634	0.700	5.001	0.7762	0.0512	-0.0031	-0.0017	-0.0010	-0.0002
7.178	0.700	5.003	0.8008	0.0618	-0.0029	-0.0020	0.0034	-0.0002
7.687	0.700	5.003	0.8197	0.0738	-0.0033	-0.0003	0.0144	0.0002
8.172	0.699	5.000	0.8363	0.0869	-0.0029	0.0012	0.0231	0.0007
8.673	0.700	5.003	0.8515	0.1012	-0.0030	0.0032	0.0298	0.0013
9.195	0.700	5.004	0.8644	0.1153	-0.0019	0.0056	0.0347	0.0020
9.684	0.700	5.004	0.8779	0.1283	-0.0029	0.0078	0.0418	0.0022
10.175	0.700	5.001	0.8911	0.1408	-0.0011	0.0094	0.0500	0.0027
10.692	0.700	5.001	0.8928	0.1544	-0.0016	0.0075	0.0630	0.0021
11.225	0.700	4.998	0.9048	0.1673	-0.0010	0.0086	0.0688	0.0022
11.686	0.700	5.000	0.9139	0.1782	-0.0016	0.0090	0.0722	0.0023
12.204	0.700	5.002	0.9208	0.1895	-0.0027	0.0090	0.0723	0.0025

B

Aerodynamic center validation data

B.1. NACA 0005 validation data

Table B.1: Forward reference frame angle of attack sweep

aoa	beta	V	Cx	Cy	Fz	CL	CDi	CDo	CMx	CMy	CMz
-5	0	73.1	-0.032	0	-0.5243	-0.5251	0.006	0.0079	0	0.026	0
-4	0	73.1	-0.0187	0	-0.4205	-0.4208	0.0038	0.0068	0	0.0208	0
-3	0	73.1	-0.0086	0	-0.3161	-0.3161	0.0022	0.0058	0	0.0157	0
-2	0	73.1	-0.0009	0	-0.2113	-0.2112	0.001	0.0055	0	0.0106	0
-1	0	73.1	0.0044	0	-0.1057	-0.1057	0.0002	0.006	0	0.0055	0
0	0	73.1	0.0058	0	0.0003	0.0003	0	0.0058	0	0.0004	0
1	0	73.1	0.0044	0	0.1065	0.1064	0.0002	0.006	0	-0.0046	0
2	0	73.1	-0.0001	0	0.2123	0.2122	0.001	0.0064	0	-0.0096	0
3	0	73.1	-0.0077	0	0.3177	0.3176	0.0022	0.0068	0	-0.0146	0
4	0	73.1	-0.0193	0	0.4226	0.423	0.0038	0.0064	0	-0.0196	0
5	0	73.1	-0.0328	0	0.5273	0.5281	0.006	0.0073	0	-0.0246	0
6	0	73.1	-0.0481	0	0.6315	0.633	0.0086	0.0096	0	-0.0296	0
7	0	73.1	-0.0675	0	0.7347	0.7375	0.0117	0.0108	0	-0.0345	0
8	0	73.1	-0.0877	0	0.8373	0.8414	0.0153	0.0145	0	-0.0394	0
9	0	73.1	-0.1113	0	0.9388	0.9446	0.0193	0.0177	0	-0.0443	0
10	0	73.1	-0.1358	0	1.0394	1.0472	0.0238	0.0229	0	-0.0493	0

Table B.2: Backward reference frame angle of attack sweep

aoa	beta	V	Cx	Cy	Fz	CL	CDi	CDo	CMx	CMy	CMz
-5	0	73.1	-0.032	0	-0.5243	-0.5251	0.006	0.0079	0	-0.0265	0
-4	0	73.1	-0.0187	0	-0.4205	-0.4208	0.0038	0.0068	0	-0.0212	0
-3	0	73.1	-0.0086	0	-0.3161	-0.3161	0.0022	0.0058	0	-0.0159	0
-2	0	73.1	-0.0009	0	-0.2113	-0.2112	0.001	0.0055	0	-0.0106	0
-1	0	73.1	0.0044	0	-0.1057	-0.1057	0.0002	0.006	0	-0.0051	0
0	0	73.1	0.0058	0	0.0003	0.0003	0	0.0058	0	0.0005	0
1	0	73.1	0.0044	0	0.1065	0.1064	0.0002	0.006	0	0.006	0
2	0	73.1	-0.0001	0	0.2123	0.2122	0.001	0.0064	0	0.0116	0
3	0	73.1	-0.0077	0	0.3177	0.3176	0.0022	0.0068	0	0.0171	0
4	0	73.1	-0.0193	0	0.4226	0.423	0.0038	0.0064	0	0.0227	0
5	0	73.1	-0.0328	0	0.5273	0.5281	0.006	0.0073	0	0.0282	0
6	0	73.1	-0.0481	0	0.6315	0.633	0.0086	0.0096	0	0.0337	0
7	0	73.1	-0.0675	0	0.7347	0.7375	0.0117	0.0108	0	0.0392	0
8	0	73.1	-0.0877	0	0.8373	0.8414	0.0153	0.0145	0	0.0446	0
9	0	73.1	-0.1113	0	0.9388	0.9446	0.0193	0.0177	0	0.0501	0
10	0	73.1	-0.1358	0	1.0394	1.0472	0.0238	0.0229	0	0.0554	0

Table B.3: Angle of attack sweep for the calculated location of the aerodynamic center as reference frame

aoa	beta	V	Cx	Cy	Fz	CL	CDi	CDo	CMx	CMy	CMz
-5	0	73.1	-0.032	0	-0.5243	-0.5251	0.006	0.0079	0	0.0008	0
-4	0	73.1	-0.0187	0	-0.4205	-0.4208	0.0038	0.0068	0	0.0006	0
-3	0	73.1	-0.0086	0	-0.3161	-0.3161	0.0022	0.0058	0	0.0005	0
-2	0	73.1	-0.0009	0	-0.2113	-0.2112	0.001	0.0055	0	0.0004	0
-1	0	73.1	0.0044	0	-0.1057	-0.1057	0.0002	0.006	0	0.0004	0
0	0	73.1	0.0058	0	0.0003	0.0003	0	0.0058	0	0.0005	0
1	0	73.1	0.0044	0	0.1065	0.1064	0.0002	0.006	0	0.0005	0
2	0	73.1	-0.0001	0	0.2123	0.2122	0.001	0.0064	0	0.0006	0
3	0	73.1	-0.0077	0	0.3177	0.3176	0.0022	0.0068	0	0.0006	0
4	0	73.1	-0.0193	0	0.4226	0.423	0.0038	0.0064	0	0.0007	0
5	0	73.1	-0.0328	0	0.5273	0.5281	0.006	0.0073	0	0.0007	0
6	0	73.1	-0.0481	0	0.6315	0.633	0.0086	0.0096	0	0.0008	0
7	0	73.1	-0.0675	0	0.7347	0.7375	0.0117	0.0108	0	0.0009	0
8	0	73.1	-0.0877	0	0.8373	0.8414	0.0153	0.0145	0	0.0009	0
9	0	73.1	-0.1113	0	0.9388	0.9446	0.0193	0.0177	0	0.001	0
10	0	73.1	-0.1358	0	1.0394	1.0472	0.0238	0.0229	0	0.001	0

C

Airbus A320-series reference figures and data

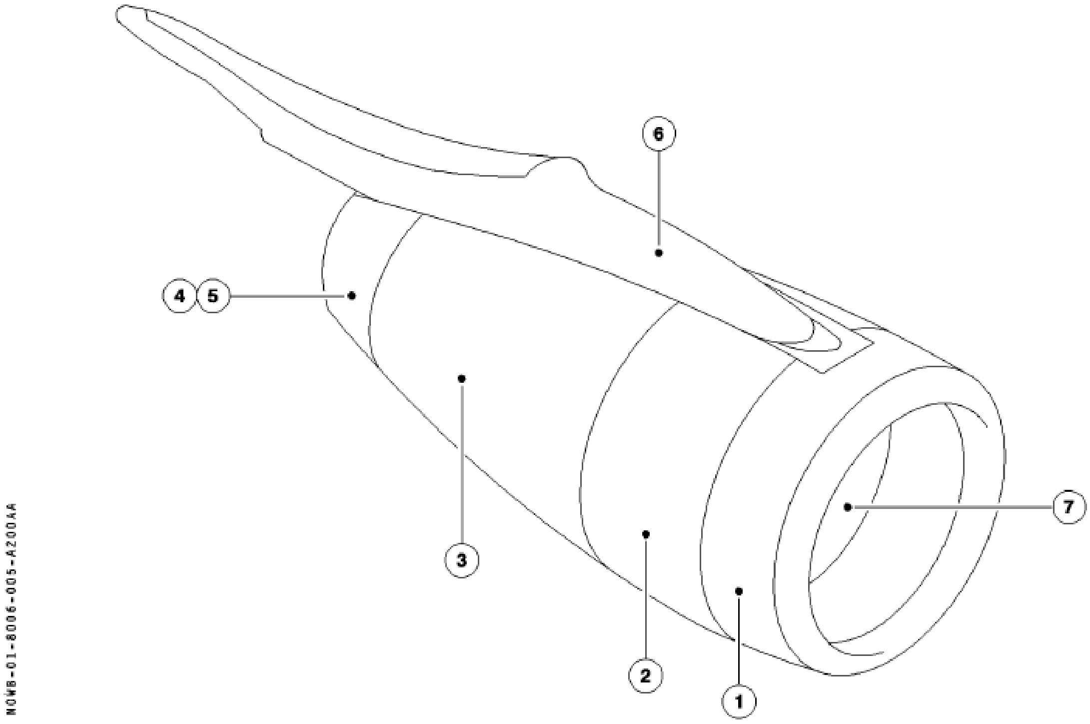

PYLON AND POD

REF N°	COMPONENT	WEIGHT		H-ARM	
		(kg)	(lb)	(m)	(in)
1	INLET	121	266	14.110	555.51
2	FAN COWL	98	215	15.120	595.27
3	THRUST REVERSER	518	1141	16.524	650.55
4	COMMON NOZZLE ASSEMBLY	84	186	18.100	712.60
5	JET PIPE AND PRIMARY PLUG	17	38	18.840	741.73
6	PYLON	570	1257	17.514	689.53
7	ENGINE	3582	7896	16.063	632.40

Figure C.1: Engine reference weights

Bibliography

[1] Vivek Ahuja and RJ Hartfield. Aerodynamic loads over arbitrary bodies by method of integrated circulation. *Journal of Aircraft*, 53(6):1719–1730, 2016.

[2] John David Anderson Jr. *Fundamentals of aerodynamics*. Tata McGraw-Hill Education, fifth edition, 2010.

[3] Mario Asselin. *An introduction to aircraft performance*. American Institute of Aeronautics and Astronautics, 1997.

[4] Dennis L Berry. The boeing 777 engine/airframe integration aerodynamic design process. In *ICAS PROCEEDINGS*, volume 19, pages 1305–1305. AMERICAN INST OF AERONAUTICS AND ASTRONAUTICS, 1994.

[5] J. Borradaile. Towards the optimum ducted uhbr engine. In *24th Joint Propulsion Conference*, 1988. doi: 10.2514/6.1988-2954. URL https://arc.aiaa.org/doi/abs/10.2514/6.1988-2954.

[6] FlightAscend Consultancy. Ascend fleets [aviation database], 2015. URL https://www.flightglobal.com/orders-and-deliveries/flightglobal-launches-fleets-analyzer-data-service/118286.article.

[7] Eugene E Covert. *Thrust and Drag: Its Prediction and Verification*, volume 98. AIAA, 1985.

[8] Nick Cumpsty, Dimitri Mavris, and Michelle Kirby. Icao enviromental report 2019. Technical report, ICAO, 2019.

[9] David L Daggett, Stephen T Brown, and Ron T Kawai. Ultra-efficient engine diameter study. Technical report, NASA, 2003.

[10] Mark Drela. Tasopt 2.00. Technical report, Tech. rep., Massachusetts Institute of Technology, 2010.

[11] Reno Elmendorp, Roelof Vos, and Gianfranco La Rocca. A conceptual design and analysis method for conventional and unconventional airplanes. *29th Congress of the International Council of the Aeronautical Sciences, ICAS 2014*, pages 1–12, 2014. ISSN 3932182804.

[12] Richard C Feagin and William D Morrison. Delta method, an empirical drag buildup technique. Technical report, NASA, 1978.

[13] International Transport Forum. Transport outlook, 2011.

[14] Panagiotis Giannakakis, Panagiotis Laskaridis, and Pericles Pilidis. Effects of offtakes for aircraft secondary-power systems on jet engine efficiency. *Journal of Propulsion and Power*, 27(5):1024–1031, 2011. ISSN 07484658. doi: 10.2514/1.B34252.

[15] JL Godard, H Hoheisel, C-C Rossow, V Schmitt, et al. Investigation of interference effects for different engine positions on a transport aircraft configuration. In *DLR Workshop*, pages 11–1/11–22, 1996.

[16] Matt Grote, Ian Williams, and John Preston. Direct carbon dioxide emissions from civil aircraft. *Atmospheric Environment*, 95:214–224, June 2014.

[17] Mark Guynn, Jeffery Berton, Kenneth Fisher, William Haller, Michael Tong, and Douglas Thurman. Analysis of turbofan design options for an advanced single-aisle transport aircraft. In *9th AIAA Aviation Technology, Integration, and Operations Conference (ATIO) and Aircraft Noise and Emissions Reduction Symposium (ANERS)*, page 6942, 2009.

[18] David K Hall, Arthur C Huang, Alejandra Uranga, Edward M Greitzer, Mark Drela, and Sho Sato. Boundary layer ingestion propulsion benefit for transport aircraft. *Journal of Propulsion and Power*, 33(5):1118–1129, 2017.

[19] Geoffrey Hill, Sherilyn Brown, Karl Geiselhart, and Cecile Burg. Integration of propulsion-airframe-aeroacoustic technologies and design concepts for a quiet blended-wing-body transport. In *AIAA 4th Aviation Technology, Integration and Operations (ATIO) Forum*, page 6403, 2004.

[20] Geoffrey A Hill and Russell H Thomas. Challenges and opportunities for noise reduction through advanced aircraft propulsion airframe integration and configurations. In *8th CEAS Workshop on Aeroacoustics of New Aircraft and Engine Configurations, Budapest, Hungary*, 2004.

[21] Sighard F. Hoerner. *Fluid Dynamic Drag - Practical Information on Aerodynamic Drag and Hydrodynamic Resistance*. Hoerner Fluid Dynamics, 1965.

[22] H Hoheisel. Aerodynamic aspects of engine-aircraft integration of transport aircraft. *Aerospace science and technology*, 1(7):475–487, 1997.

[23] Muwanika Jdiobe, Kyle Hickman, James A. Kidd, and Nicoletta Fala. Improving undergraduate aerospace engineer professional readiness through boeing 737 max crash case study. In *AIAA AVIATION 2020 FORUM*, 2020. doi: 10.2514/6.2020-2937. URL https://arc.aiaa.org/doi/abs/10.2514/6.2020-2937.

[24] Lloyd R Jenkinson, Paul Simpkin, Darren Rhodes, Lloyd R Jenkison, and Rolls Royce. *Civil jet aircraft design*, volume 338. Arnold London, UK, 1999.

[25] Schmidt K. and Vos R. A semi-analytical weight estimation method for oval fuselages in conventional and novel aircraft. In *52nd Aerospace Sciences Meeting*, page 0026, 2014. doi: 10.2514/6.2014-0026. URL https://arc.aiaa.org/doi/abs/10.2514/6.2014-0026.

[26] Anastasia Kharina and Daniel Rutherford, Ph.D. Fuel efficiency trends for new commercial jet aircraft: 1960 to 2014. Technical report, International Council on Clean Transportation, Washington DC 20005 USA, 2015.

[27] David S. Lee, David W. Fahey, Piers M. Forster, Peter J. Newton, Ron C.N. Wit, Ling L. Lim, Bethan Owena, and Robert Sausen. Aviation and global climate change in the 21st century. *Atmospheric Environment*, 43(22-23):3520–3537, April 2009.

[28] Jack D Mattingly. *Aircraft engine design*. Aiaa, 2002.

[29] J.A. Mulder, W.H.J.J. van Staveren, J.C. van der Vaart, E. de Weerdt, C.C. de Visser, A.C. in 't Veld, and E. Mooij. Flight dynamics - lecture notes. Technical report, Faculty of Aerospace Engineering - Delft University of Technology, March 2013.

[30] E. Obert. *Aerodynamic Design of Transport Aircraft*. IOS Press, 2009. ISBN 9781586039707.

[31] Guilherme Oliveira, Luis Gustavo Trapp, and Antonini Puppin-Macedo. Engine-airframe integration methodology for regional jet aircrafts with underwing engines. In *41st aerospace sciences meeting and exhibit*, page 934, 2003.

[32] International Civil Aviation Organization. Enviromental report 2010. Technical report, ICAO, 2010.

[33] Martin Orlita and Roelof Vos. Cruise performance optimization of the airbus a320 through flap morphing. In *17th AIAA Aviation Technology, Integration, and Operations Conference*, page 3264, 2017.

[34] N. Peacock. Engine design and systems integration for propfan and high bypass turbofan engines. In *23rd Joint Propulsion Conference*, 1987. doi: 10.2514/6.1987-1730. URL https://arc.aiaa.org/doi/abs/10.2514/6.1987-1730.

[35] B. Peerlings. A review of aerodynamic flow models, solution methods and solvers – and their applicability to aircraft conceptual design. Master's thesis, Delft University of Technology, Delft, 10 2018.

[36] M Pflug and Ch Haberland. On numerical jet flow simulation of current and future high by-pass engines. *Aspects of engine airframe integration for transport aircraft*, pages 25–1, 1996.

[37] Pieter-Jan Proesmans and Roelof Vos. Airplane design optimization for minimal global warming impact. In *AIAA Scitech 2021 Forum*, page 1297, 2021.

[38] Daniel P. Raymer. *Aircraft Design: A Conceptual Approach*. American Institute of Aeronautics and Astronautics, Inc., sixth edition, 2018. ISBN 978-1-62410-490-9.

[39] Melissa B Rivers and Ashley Dittberner. Experimental investigations of the nasa common research model. *Journal of Aircraft*, 51(4):1183–1193, 2014.

[40] Matthew Robinson, David G MacManus, and Christopher Sheaf. Aspects of aero-engine nacelle drag. *Proceedings of the Institution of Mechanical Engineers, Part G: Journal of Aerospace Engineering*, 233(5):1667–1682, 2019.

[41] Jan Roskam. *Airplane Design Parts I-VIII*. Roskam Aviation and Engineering Corp, 1985.

[42] Ralf Rudnik, Cord-Christian Rossow, and Heiko Frhr v Geyr. Numerical simulation of engine/airframe integration for high-bypass engines. *Aerospace Science and Technology*, 6(1):31–42, 2002.

[43] Robert Sausen and Ulrich Schumann. Estimates of the climate response to aircraft co2 and noxemissions scenarios. *Climatic Change*, 44(1):27–58, Jan 2000. ISSN 1573-1480. doi: 10.1023/A:1005579306109. URL https://doi.org/10.1023/A:1005579306109.

[44] Robert Sausen, Ivar Isaksen, Volker Grewe, Didier Hauglustaine, David S Lee, Gunnar Myhre, Marcus O Köhler, Giovanni Pitari, Ulrich Schumann, Frode Stordal, et al. Aviation radiative forcing in 2000: An update on ipcc (1999). *Meteorologische Zeitschrift*, 14(4):555–561, 2005.

[45] Customer Service. *A320 - Weight and Balance Manual*. AIRBUS S.A.S., 39 edition, Dec 2002.

[46] Customer Service. *Aicraft Characteristics - Airport and Maintenance Planning*. AIRBUS S.A.S., 39 edition, Dec 2020.

[47] Tomasz P Stankowski, David G MacManus, Chrisopher T Sheaf, and Nicholas Grech. Aerodynamic interference for aero-engine installations. In *54th AIAA Aerospace Sciences Meeting*, page 0766, 2016.

[48] Edward N Tinoco, Olaf P Brodersen, Stefan Keye, Kelly R Laflin, Edward Feltrop, John C Vassberg, Mori Mani, Ben Rider, Richard A Wahls, Joseph H Morrison, et al. Summary data from the sixth aiaa cfd drag prediction workshop: Crm cases. *Journal of Aircraft*, 55(4):1352–1379, 2018.

[49] E. Torenbeek. *Synthesis of Subsonic Airplane Design*. Delft University Press, Martinus Nijhotf Publishers, 1982. ISBN 90-247-2724-3.

[50] E. Torenbeek. *Advanced Aircraft Design - Conceptual Design, Analysis and Optimization of Subsonic Civil Airplanes*. Aerospace Series. John Wiley and Sons, Ltd., 2013. ISBN 9781119969303.

[51] John Vassberg, Mark Dehaan, Melissa Rivers, and Richard Wahls. Development of a common research model for applied cfd validation studies. In *26th AIAA applied aerodynamics conference*, page 6919, 2008.

[52] Roelof Vos and Saeed Farokhi. *Introduction to transonic aerodynamics*, volume 110. Springer, 2015.

[53] F.R. Wood, A. Bows, and K. Anderson. Apportioning aviation co2 emissions to regional administrations for monitoring and target setting. *Transport Policy*, 17(4):206 – 215, 2010. ISSN 0967-070X. doi: https://doi.org/10.1016/j.tranpol.2010.01.010. URL http://www.sciencedirect.com/science/article/pii/S0967070X10000223.